

**APPLIED PHYSICS REVIEWS—FOCUSED REVIEW****Third-generation infrared photodetector arrays**A. Rogalski,<sup>1</sup> J. Antoszewski,<sup>2,a)</sup> and L. Faraone<sup>2</sup><sup>1</sup>*Institute of Applied Physics, Military University of Technology, 2 Kaliskiego Street, 00-908 Warsaw, Poland*<sup>2</sup>*School of Electrical, Electronic and Computer Engineering, The University of Western Australia, Crawley 6009, Australia*

(Received 30 June 2008; accepted 26 January 2009; published online 11 May 2009)

Hitherto, two distinct families of multielement detector arrays have been used for infrared (IR) imaging system applications: linear arrays for scanning systems (first generation) and two-dimensional arrays for staring systems (second generation). Nowadays, third-generation IR systems are being developed which, in the common understanding, provide enhanced capabilities such as larger numbers of pixels, higher frame rates, better thermal resolution, multicolor functionality, and/or other on-chip signal-processing functions. In this paper, fundamental and technological issues associated with the development and exploitation of third-generation IR photon detectors are discussed. In this class of detectors the two main competitors, HgCdTe photodiodes and quantum-well photoconductors, are considered. This is followed by discussions focused on the most recently developed focal plane arrays based on type-II strained-layer superlattices and quantum dot IR photodetectors. The main challenges facing multicolor devices are concerned with complicated device structures, thicker and multilayer material growth, and more difficult device fabrication, especially for large array sizes and/or small pixel dimensions. This paper also presents and discusses the ongoing detector technology challenges that are being addressed in order to develop third-generation infrared photodetector arrays. © 2009 American Institute of Physics. [DOI: [10.1063/1.3099572](https://doi.org/10.1063/1.3099572)]

**TABLE OF CONTENTS**

I. INTRODUCTION.....	1	2. Experimental verification.....	25
II. BRIEF HISTORY OF IR DETECTORS.....	2	VII. HgCdTe MULTICOLOR DETECTORS.....	26
III. FIRST- AND SECOND-GENERATION IR IMAGING SYSTEMS.....	3	A. HgCdTe dual-band detectors.....	26
IV. BENEFITS OF MULTICOLOR DETECTION....	5	B. Three-color HgCdTe detectors.....	30
V. REQUIREMENTS OF THIRD-GENERATION DETECTORS.....	6	VIII. MULTIBAND QWIPS.....	32
A. Noise equivalent difference temperature....	6	IX. TYPE-II InAs/GaInSb DUAL-BAND DETECTORS.....	36
B. Pixel and chip sizes.....	7	X. MULTIBAND QDIPS.....	38
C. Uniformity.....	8	XI. ADAPTIVE FPAS.....	39
D. Identification and detection ranges.....	9	XII. CONCLUSIONS.....	40
VI. MATERIAL CONSIDERATIONS FOR THIRD-GENERATION IR DETECTORS.....	9	XIII. NOMENCLATURE.....	41
A. HgCdTe.....	10		
1. Outlook on crystal growth.....	11	<b>I. INTRODUCTION</b>	
2. HgCdTe photodiodes.....	13	Multicolor detector capabilities are highly desirable for advanced infrared (IR) imaging systems, since they provide enhanced target discrimination and identification, combined with lower false-alarm rates. Systems that collect data in separate IR spectral bands can discriminate both absolute temperature as well as unique signatures of objects in the scene. By providing this new dimension of contrast, multi-band detection also offers advanced color processing algorithms to further improve sensitivity above that of single-color devices. This is extremely important for identifying temperature differences between missile targets, warheads, and decoys. Multispectral IR focal plane arrays (FPAs) are highly beneficial for a variety of applications such as missile warning and guidance, precision strike, airborne surveil-	
B. QWIPs.....	15		
C. InAs/GaInSb type-II SLS photodiodes.....	19		
1. Material properties.....	19		
2. SL photodiodes.....	20		
D. QDIP.....	22		
1. Anticipated advantages of QDIPs.....	23		

<sup>a)</sup>Electronic mail: [jarek@ee.uwa.edu.au](mailto:jarek@ee.uwa.edu.au).

lance, target detection, recognition, acquisition and tracking, thermal imaging, navigational aids and night vision, etc.<sup>1,2</sup> They also play an important role in Earth and planetary remote sensing, astronomy, etc.<sup>3</sup>

Military surveillance, target detection, and target tracking can be undertaken using single-color FPAs if the targets are easy to identify. However, in the presence of clutter, or when the target and/or background are uncertain, or in situations where the target and/or background may change during engagement, single-color system design involves compromises that can degrade overall capability. It is well established that in order to reduce clutter and enhance the desired features/contrast, one will require the use of multispectral FPAs. In such cases, multicolor imaging can greatly improve overall system performance.

Currently, multispectral systems rely on cumbersome imaging techniques that either disperse the optical signal across multiple IR FPAs or use a filter wheel to spectrally discriminate the image focused on a single FPA. These systems include beamsplitters, lenses, and bandpass filters in the optical path to focus the images onto separate FPAs responding to different IR bands. Also, complex optical alignment is required to map the multispectral image pixel for pixel. Consequently, these approaches are relatively high cost and place additional burdens on the sensor platform because of their extensive size, complexity, and cooling requirements.

In the future, multispectral imaging systems will include very large sensors feeding an enormous amount of data to the digital mission processing subsystem. FPAs with the number of pixels above  $1 \times 10^6$  are now available. As these imaging arrays grow in detector number for higher resolution, so will the computing requirements for the embedded digital image processing system. One approach to solving this processing bottleneck problem could be to incorporate a certain amount of pixel-level processing within the detector pixel, similar to the technique implemented in biological sensor information processing systems. Currently, several scientific groups in the world have turned to the biological retina for answers as to how to improve man-made sensors.<sup>4,5</sup>

In this paper, we will review the state-of-the-art multicolor detector technologies over a wide IR spectral range. In the beginning we will outline the historical evolution of IR detector technology showing why certain device designs and architectures have emerged as successful candidates in the development of multicolor detectors. Next, discussion is focused on the most recently developed FPAs containing such material systems as HgCdTe photodiodes, type-II strained-layer superlattices (SLS), quantum-well IR photodetectors (QWIPs), and quantum dot IR photodetectors (QDIPs). Finally, we discuss the ongoing detector technology efforts being undertaken to realize third-generation FPAs.

## II. BRIEF HISTORY OF IR DETECTORS

Looking back over the past 1000 years, it is noted that IR radiation itself was unknown until just under 200 years ago when Herschel's experiments with thermometers was first reported. He built a crude monochromator that used a thermometer as a thermal detector so that he could measure

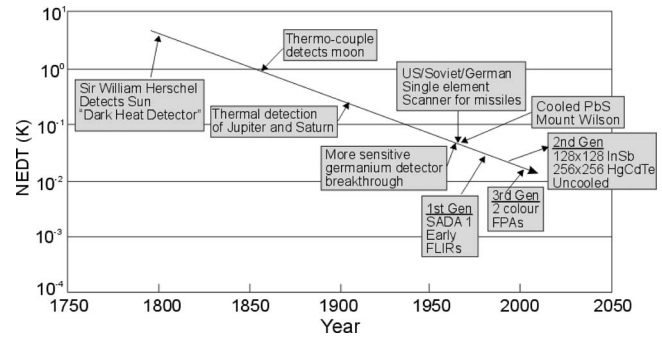


FIG. 1. Development of IR detectors: NEDT vs era (after Ref. 5).

the distribution of energy in sunlight. The early history of IR was reviewed about 40 years ago in two well-known monographs<sup>6,7</sup> and Barr's paper.<sup>8</sup>

Initially, the development of IR detectors was connected with thermal detectors. In 1821 Seebeck discovered the thermoelectric effect and soon thereafter demonstrated the first thermocouple, but several years later, in 1829, Nobili constructed the first thermopile by connecting a number of thermocouples in series. Langley's bolometer appeared in 1880, in which he used two thin ribbons of platinum foil, connected so as to form two arms of a Wheatstone bridge. He continued to develop his bolometer over the next 20 years, 400 times more sensitive than in his first efforts. His latest bolometer could detect the heat from a cow at a distance of quarter of a mile.

The initial spectacular applications of thermal detectors in astronomy are noted in Fig. 1. In 1856, Charles Piazzi Smyth,<sup>9,10</sup> from the peak of Guajara on Tenerife, detected IR radiation from the Moon using a thermocouple. In the early 1900s, IR radiation was successfully detected from the planets Jupiter and Saturn and from some bright stars such as Vega and Arcturus. In 1915, William Coblentz<sup>9</sup> at the U.S. National Bureau of Standards developed thermopile detectors, which he uses to measure the IR radiation from 110 stars. However, the low sensitivity of early IR instruments prevented the detection of other near-IR sources. Work in IR astronomy remained at a low level until breakthroughs in the development of new, sensitive IR detectors were achieved in the late 1950s.

Photon detectors were developed during the 20th century. The first IR photoconductor was developed by Case in 1917.<sup>11</sup> In 1933, Kutzscher at the University of Berlin discovered that lead sulfide (from natural galena found in Sardinia) was photoconductive and had a response out to about  $3 \mu\text{m}$ .<sup>12</sup>

IR detector technology development was and continues to be primarily driven by military applications. Many of these advances were transferred to IR astronomy from U.S. Department of Defense research. In the mid-1960s, the first IR survey of the sky was made at the Mount Wilson Observatory using liquid nitrogen cooled PbS photoconductors, which were most sensitive at  $2.2 \mu\text{m}$ . The survey covered approximately 75% of the sky and found about 20 000 IR sources.<sup>9</sup> Many of these sources were stars which had never been seen before in visible light.

Hitherto, many materials have been investigated in the

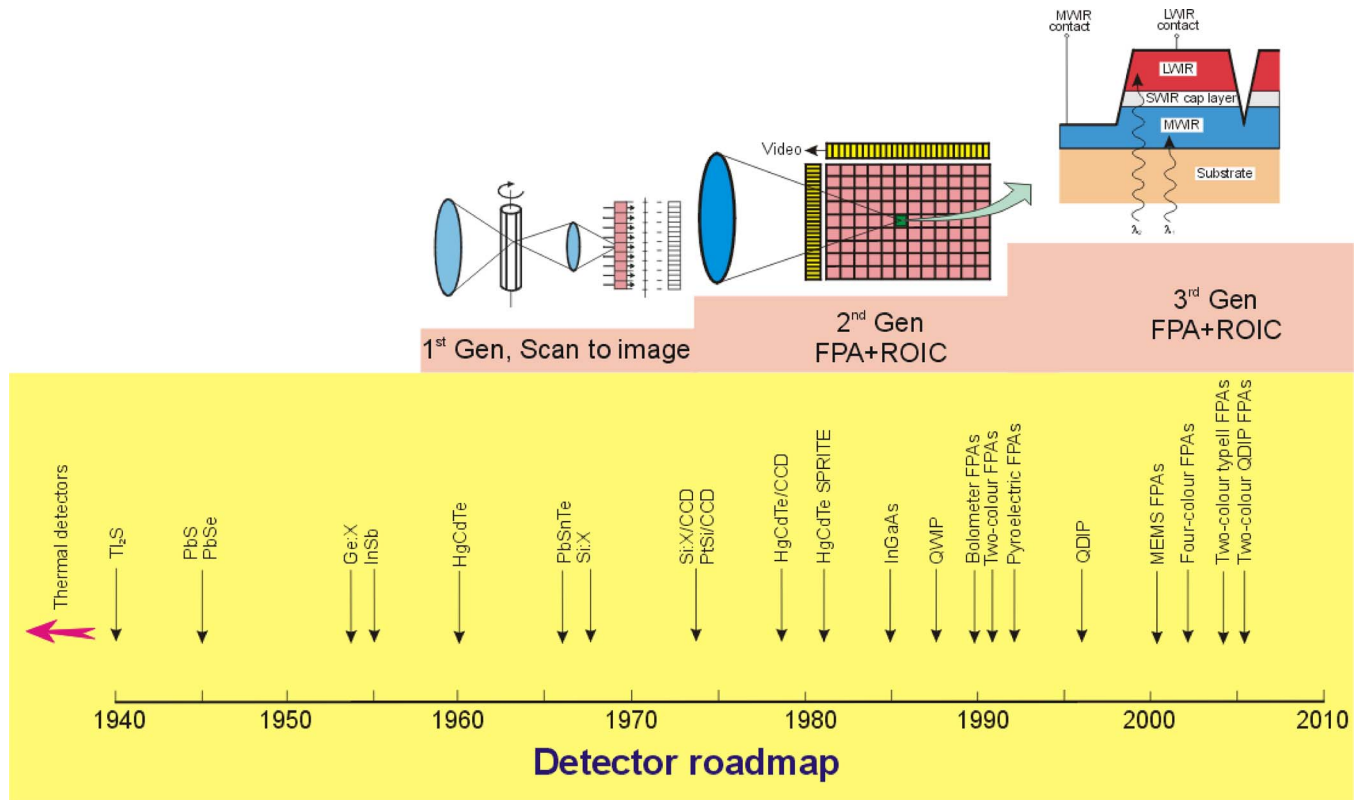


FIG. 2. (Color online) History of the development of IR detectors and systems. Three generation systems can be considered for principal military and civilian applications: First generation (scanning systems), second generation (staring systems—electronically scanned), and third generation (multicolor functionality and other on-chip functions).

IR field. Observing a history of the development of IR detector technology, a simple theorem, after Norton,<sup>13</sup> can be stated: “All physical phenomena in the range of about 0.1–1 eV can be proposed for IR detectors.” Among these phenomena are thermoelectric power (thermocouples), change in electrical conductivity (bolometers), gas expansion (Golay cell), pyroelectricity (pyroelectric detectors), photon drag, Josephson effect (Josephson junctions, superconducting quantum interference devices), internal emission (PtSi Schottky barriers), fundamental absorption (intrinsic photodetectors), impurity absorption (extrinsic photodetectors), low dimensional solids [superlattice (SL), quantum well (QW), and quantum dot (QD) detectors], different types of phase transitions, etc.

Figure 2 gives approximate dates of significant development efforts for the above-mentioned materials. The years during World War II saw the origins of modern IR detector technology. Photon IR technology combined with semiconductor material science, photolithography technology developed for integrated circuits, and the impetus of Cold War military preparedness have propelled extraordinary advances in IR capabilities within a short time period during the last century.<sup>14</sup>

### III. FIRST- AND SECOND-GENERATION IR IMAGING SYSTEMS

Two distinct families of multielement detector arrays can be considered for military and civilian IR imaging applications; one used for scanning systems and the other used for

staring systems (see upper part of Fig. 2). Scanning systems, which do not include multiplexing functions in the focal plane, belong to first-generation systems. A typical example of this kind of detector is a linear photoconductive array in which an electrical contact to each element of a multielement array is connected from the cryogenically cooled focal plane to the outside, where there is one electronic amplifying channel at ambient temperature for each detector element. The U.S. common-module HgCdTe arrays employ 60, 120, or 180 photoconductive elements, depending on the application. HgCdTe photoconductors entered production in the late 1970s following the establishment of reproducible bulk growth techniques and anodic oxide surface passivation. Although first-generation systems are now being supplanted by second-generation photovoltaic-based arrays, the production of such devices will continue for many years to come. It should be noted that many photovoltaic detector arrays are also used in scanning formats.

Second-generation systems (full-framing systems) typically have three orders of magnitude more elements ( $>10^6$ ) on the focal plane than first-generation systems, and the detector elements are configured in a two-dimensional (2D) array format. These staring arrays are scanned electronically by readout integrated circuits (ROICs) that are hybrid packaged with the arrays. These modules are 2D arrays of photodiodes connected with indium bumps to a ROIC chip as a hybrid structure, often called a sensor chip assembly (SCA) (see Fig. 3). These ROICs include, e.g., pixel deselecting, antiblooming on each pixel, subframe imaging, output



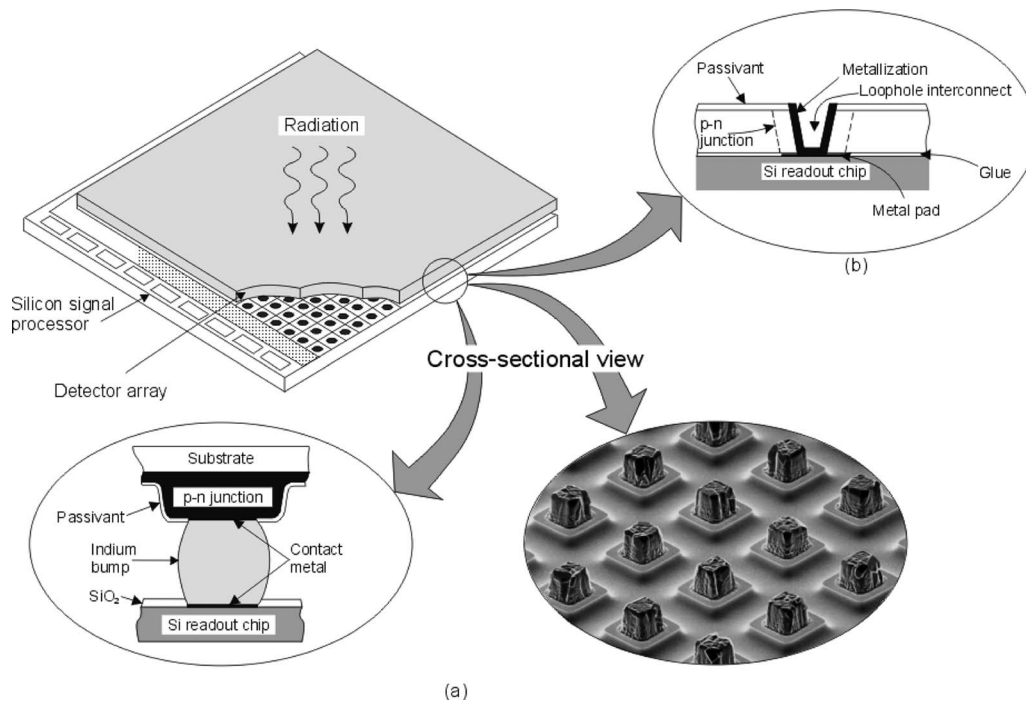


FIG. 3. Hybrid IR FPA with independently optimized signal detection and readout: (a) indium bump technique; (b) loophole technique.

preamplifiers, and many other functions in such structures. The detector material and multiplexer can be optimized independently. Other advantages of hybrid-packaged FPAs are near-100% fill factors and increased signal-processing area on the multiplexer chip. Photodiodes with their very low power dissipation, inherently high impedance, negligible  $1/f$  noise, and easy multiplexing via the ROIC can be assembled in 2D arrays containing a very large number of pixels, limited only by existing technologies. Photodiodes can be reverse biased for even higher impedance, and can therefore better match electrically with compact low-noise silicon readout preamplifier circuits. The photoresponse of photodiodes remains linear for significantly higher photon flux levels than that of photoconductors, primarily because of higher doping levels in the photodiode absorber layer and because the photogenerated carriers are collected rapidly by the junction. Development of hybrid packaging technology began in the late 1970s (Ref. 15) and took the next decade to reach volume production. In the early 1990s, fully 2D imaging arrays provided a means for staring sensor systems to enter the production stage. In the hybrid architecture, indium bump bonding with readout electronics provides for multiplexing the signals from thousands or millions of pixels onto a few output lines, greatly simplifying the interface between the vacuum-enclosed cryogenic sensor and the system electronics.

Hybridized FPA detectors and multiplexers are also fabricated using a loophole interconnection structure.<sup>16</sup> In this case, the IR detector material and the multiplexer chip are glued together to form a single bonded unit before detector fabrication. The photovoltaic detector elements are then formed by a combination of ion implantation and an etching process, with the loopholes drilled by ion milling. The loop-

hole interconnection technology offers more stable mechanical and thermal features than the flip-chip indium bump-bonded hybrid architecture.

The 2D second-generation detector arrays are usually illuminated from the back side with photons passing through the transparent detector array substrate. In HgCdTe hybrid FPAs, photovoltaic detectors are usually formed on a thin HgCdTe epitaxial layer grown on a transparent CdZnTe substrate. For the HgCdTe flip-chip hybrid technology, the maximum chip size is on the order of 20 mm square due to thermal mismatch between the FPA and ROIC. To overcome this problem, alternatives to CdTe for epitaxy technology was developed with sapphire or silicon as the substrate for the HgCdTe layer. When using opaque materials, substrates must be thinned to below  $10\ \mu\text{m}$  to obtain sufficient quantum efficiencies and minimize cross-talk.

Intermediate systems in use are also fabricated with multiplexed scanned photodetector linear arrays and with, as a rule, time delay and integration (TDI) functions. Typical examples of these systems are HgCdTe multilinear  $288 \times 4$  arrays, fabricated by Sofradir for both 3–5 and 8–10.5  $\mu\text{m}$  bands with signal processing on the focal plane.

Complementary metal oxide semiconductor (CMOS) multiplexers are the best choice to perform the integration and signal processing for 2D arrays. The advantages of CMOS are that existing foundries, which fabricate application specific integrated circuits, can be readily used by adapting their design rules. Design rules of  $0.07\ \mu\text{m}$  are currently in production, with preproduction runs of  $0.045\ \mu\text{m}$  design rules. As a result of such fine design rules, more functionality has been designed into the unit cells of IR and visible multiplexers with smaller unit cells, leading to large array sizes. Figure 4 shows the timelines for minimum circuit features and the resulting charge-coupled device (CCD), IR FPA, and

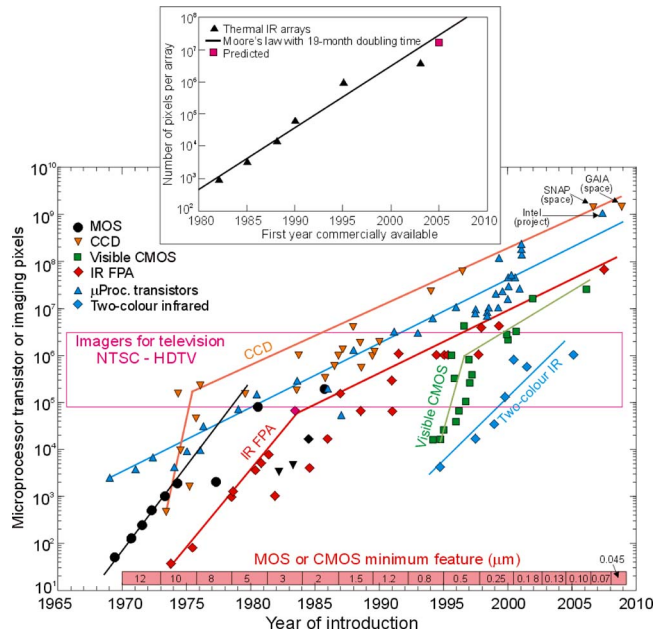


FIG. 4. (Color online) Imaging array formats compared with the complexity of microprocessor technology as indicated by transistor count. The timeline design rule of MOS/CMOS features is shown at the bottom (after Ref. 17 with completions). The number of pixels on an IR array has been growing exponentially, in accordance with Moore's law for 25 years with a doubling time of approximately 19 months (insert of figure—after Ref. 18).

CMOS visible imager sizes with respect to number of imaging pixels. Along the horizontal axis is also a scale depicting the general availability of various MOS and CMOS processes. The ongoing migration to even finer lithography will thus enable the rapid development of CMOS-based imagers having even higher resolution, better image quality, higher levels of integration, and lower overall imaging system cost than CCD-based solutions. At present, CMOS with minimum features of  $\leq 0.5 \mu\text{m}$  makes possible monolithic visible CMOS imagers because the denser photolithography allows for low-noise signal extraction and high-performance detection with high optical fill factor within each pixel. The silicon wafer production infrastructure which has put high-performance personal computers into many homes makes CMOS-based imaging in consumer products such as video and digital still cameras widely available.

Large 2D IR detector arrays, that meet the demanding requirements of astronomy and civil space applications, are also available today. IR radiation, having longer wavelengths and lower energy than visible light, is not suitable for use with the photographic plates which are used in visible light astronomy. Astronomers, in particular, have eagerly waited for the day when optoelectronic arrays could match the size of photographic film. Development of large format, high sensitivity, mosaic IR sensors for ground-based astronomy is the goal of many observatories around the world, since large arrays dramatically multiply the data output of a telescope system.

For the past 25 years array size has been increasing at an exponential rate, following the Moore's law growth path (see insert of Fig. 4), with the number of pixels doubling every 19 months. The graph shows the number of pixels per SCA as a

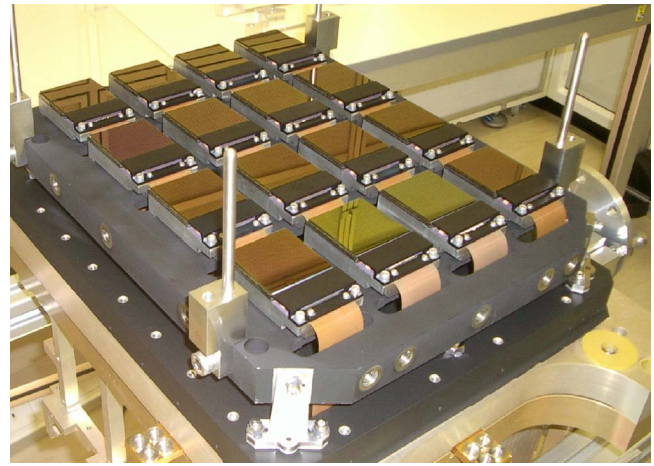


FIG. 5. (Color online) Sixteen  $2048 \times 2048$  HgCdTe SCAs were assembled for the VISTA telescope. The SCAs are attached to a precision ground plate that ensures that all pixels are within  $12 \mu\text{m}$  of the desired focus. The detectors are ready to be placed in the telescope camera's vacuum chamber and cooled to 72 K (after Ref. 17).

function of the year first used in astronomy for medium-wavelength IR (MWIR) SCAs. At present arrays exceed  $4K \times 4K$  format— $16 \times 10^6$  pixels—this about a year later than the Moore's law prediction.

It should be noted that the dramatic increase in the number of pixels is observed in short- and medium-wavelength applications where most or all of the sensing time can be used for signal integration. In the log wavelength IR (LWIR) spectral region, the photon flux from earth scenes fills the unit cell charge-storage capacitor in just a fraction of the available time (especially in the case of HgCdTe photodiodes), limiting the full-signal averaging advantage of staring technology. Even so, the improvement over LWIR scanned sensors is significant.

The trend of increasing pixel numbers is likely to continue in the area of large-format arrays. This increase will be continued using a close-butted mosaic of several SCAs as shown in Fig. 5. Raytheon has recently manufactured a  $4 \times 4$  mosaic of  $2K \times 2K$  HgCdTe SCAs into the final focal plane configuration to survey the entire sky in the southern hemisphere at four IR wavelengths. With  $67 \times 10^6$  pixels, this is currently the world's largest IR FPA. Although there are currently technological limitations to reducing the size of the gaps between active detectors on adjacent SCAs, many of these can be overcome. It is predicted that FPAs of 100 megapixels and larger will be possible in the near future, constrained only by budgets, but not technology.<sup>19</sup>

#### IV. BENEFITS OF MULTICOLOR DETECTION

IR multispectral imaging, sometimes referred to in the literature as hyperspectral imaging, is a relatively recent development that combines the information available from spectroscopy with the ability to acquire this information in a spatially resolved manner.<sup>20</sup> Instrumentally, an IR camera is used to record the spatial distribution of IR radiation in the scene, and the spectral information is gained by scanning a dispersive element to record spectra for each image. Single-color FPAs in conjunction with spectral filters, grating spec-

trometers or Fourier transform spectrometers have been deployed for a variety of NASA spaceborne remote-sensing applications utilizing push-broom scanning to record hyperspectral images of the Earth over the visible through very LWIR (VLWIR) spectral range. Dispersive devices based on mechanical scanning (e.g., filter wheels, monochromators) are not desirable because, in addition to their relatively large size they are prone to vibrations and are spectrally tuned in a relatively narrow range at a relatively slow speed.<sup>21</sup> Recent advances in material, electronic, and optical technologies have led to the development of novel types of electronically tunable filters, including the so-called adaptive FPAs.<sup>22</sup>

As mentioned in Sec. I, simultaneous detection in multiwavelength bands with a single FPA results in reduction or elimination of heavy and complex optical components now required for wavelength differentiation in remote sensors and leads to smaller, lighter, simpler instruments with better performance.

Whenever the target to be detected behaves as a blackbody, the true temperature inferred from the body is accurate and reliable. On the other hand, when it exhibits a behavior different from a blackbody, emissivity compensation needs to be undertaken. In the case of a known emissivity,  $\varepsilon$ , a single wavelength system can be used, whereas for gray body (unknown but constant emissivity in a narrow bandwidth) a dual-color system is more likely to be utilized.

Let us consider detectors, which are selected so as to cover the spectral range of blackbody emission from the target surface at the desired temperature. Thus, their cutoff wavelength will be shorter for higher temperature objects. Depending on the selected detectors, the two-band technique allows for temperature measurements, for example, with either MWIR detectors (higher temperature range) or LWIR detectors (lower temperature range). The detector is aimed toward the scene which is at a temperature  $T$ , which initially can be taken as a blackbody given by Planck's law,

$$r(\lambda) = \frac{2h\nu^2}{\lambda^3 \exp[(h\nu/kT) - 1]}, \quad (1)$$

where  $r$  is the radiance per unit wavelength and  $\nu$  is the radiation frequency.

The technique of two-color detection consists of making two measurements of the collected power at two separate wavelengths  $\lambda_1$  and  $\lambda_2$ . It can be shown that the ratio of the detected signals is equal to

$$R = \left( \frac{\varepsilon_1}{\varepsilon_2} \right) \left( \frac{\lambda_1}{\lambda_2} \right)^5 \left( \frac{\sigma_2 \Delta \lambda_2}{\sigma_1 \Delta \lambda_1} \right) \exp \left[ \frac{hc}{kT} \left( \frac{1}{\lambda_2} - \frac{1}{\lambda_1} \right) \right]. \quad (2)$$

The signal is now of the type

$$R = C_1 \exp \left( \frac{C_2}{T} \right), \quad (3)$$

where  $C_1$  and  $C_2$  are constants of the instrument. Taking the logarithm of  $R$  we have

$$\ln R = \ln C_1 + \frac{C_2}{T}, \quad (4)$$

and finally solving for  $T$

$$\begin{aligned} T &= \frac{C_2}{\ln R - \ln C_1} \\ &= \frac{(hc/k)[(1/\lambda_2) - (1/\lambda_1)]}{\ln R + \ln(\varepsilon_2/\varepsilon_1) + 5 \ln(\lambda_2/\lambda_1) + \ln(\sigma_1 \Delta \lambda_1 / \sigma_2 \Delta \lambda_2)}. \end{aligned} \quad (5)$$

The two-color detection technique is beneficial because the temperature becomes independent of the object emissivity, providing that the emissivity does not vary between  $\lambda_1$  and  $\lambda_2$  and is inherently self-calibrated. This method can be extremely useful in missile detection where there is a large difference between the temperature of the surface of the missile and the missile exhaust plume.

## V. REQUIREMENTS OF THIRD-GENERATION DETECTORS

In the 1990s (see Fig. 2) third-generation IR detectors emerged after the tremendous impetus provided by detector developments. The definition of third-generation IR systems is not particularly well established. In the common understanding, third-generation IR systems provide enhanced capabilities such as larger number of pixels, higher frame rates, better thermal resolution, as well as multicolor functionality and other on-chip signal-processing functions. According to Reago *et al.*,<sup>23</sup> the third generation is defined by the requirement to maintain the current advantage enjoyed by the U.S. and allied armed forces. This class of devices includes both cooled and uncooled FPAs:<sup>1,23</sup> (i) high performance, high resolution cooled imagers having multicolor bands; (ii) medium- to high-performance uncooled imagers; (iii) very low cost, expendable uncooled imagers.

When developing third-generation imagers, the IR community is faced with many challenges. Some of them are considered here: (i) noise equivalent temperature difference (NEDT), (ii) pixel and chip size issues, (iii) uniformity, and (iv) identification and detection ranges.

### A. Noise equivalent difference temperature

For FPAs the relevant figure of merit is the NEDT, the temperature change of a scene required to produce a signal equal to the rms noise. It can be shown that<sup>24</sup>

$$\text{NEDT} = (\tau C \eta_{\text{BLIP}} \sqrt{N_w})^{-1}, \quad (6)$$

where  $\tau$  is the optics transmission spectrum and  $C$  is the thermal contrast.  $N_w$  is the number of photogenerated carriers integrated for one integration time  $t_{\text{int}}$  and  $\Phi_B$  is the photon flux density incident on detector area  $A_d$ ,

$$N_w = \eta A_d t_{\text{int}} \Phi_B. \quad (7)$$

Percentage of background-limited performance (BLIP),  $\eta_{\text{BLIP}}$ , is simply the ratio of photon noise to composite FPA noise,

$$\eta_{\text{BLIP}} = \left( \frac{N_{\text{photon}}^2}{N_{\text{photon}}^2 + N_{\text{FPA}}^2} \right)^{1/2}. \quad (8)$$

From the above formulae, an important result is that the charge handling capacity of the readout, the integration time



linked to the frame time, and dark current of the sensitive material become the major issues limiting the performance of IR FPAs. The NEDT is inversely proportional to the square root of the integrated charge, and therefore the greater the charge, the higher the performance.

The distinction between integration time and the FPA frame time must be noted. At high backgrounds it is often impossible to handle the large amount of carriers generated within a frame time compatible with standard video rates. Off-FPA frame integration can be used to attain a level of sensor sensitivity that is commensurate with the detector-limited  $D^*$  and not the charge-handling-limited  $D^*$ . Even though the detectivity of LWIR detectors is background limited, the ROIC can collect only about 1% of the charge within the unit cell for a flux of  $10^{16}$ – $10^{17}$  photons/cm<sup>2</sup> s. Unit cell capacitors fill up in about 100  $\mu$ s, while the frame time is on the order of 10 ms.

The well charge capacity is the maximum amount of charge that can be stored on the storage capacitor of each unit cell. The size of the unit cell is limited to the dimensions of the detector element in the array. Usually, it is assumed that the integration time is such that the readout node capacity is maintained at half full. For a  $30 \times 30$   $\mu$ m<sup>2</sup> pixel size, the storage capacities are limited to  $1$ – $5 \times 10^7$  electrons. For LWIR HgCdTe FPAs the integration time is usually below 100  $\mu$ s. Since the noise power bandwidth  $\Delta f = 1/2t_{\text{int}}$ , a short integration time results in extra noise in the integration process.

Current readout technology is based on CMOS circuitry that has benefited from dramatic and continuing progress in miniaturizing circuit dimensions. Second-generation imagers provide NEDT of about 20–30 mK with  $f/2$  optics. A goal of third-generation imagers is to achieve sensitivity improvement corresponding to NEDT of about 1 mK. From Eq. (6) it can be determined that in a 300 K scene in the LWIR region with thermal contrast of 0.02, the required charge-storage capacity is above  $10^9$  electrons. This high charge-storage density cannot be obtained within the small pixel dimensions using standard CMOS capacitors.<sup>1</sup> Although the reduced oxide thickness of submicrometer CMOS design rules gives large capacitance per unit area, the reduced bias voltage, as illustrated in Fig. 6, largely cancels any improvement in charge-storage density. Ferroelectric capacitors may provide much greater charge-storage densities than the oxide-on-silicon capacitors now used. However, such a technology is not yet incorporated into standard CMOS foundries.

To provide an opportunity to significantly increase both, the charge-storage capacity and the dynamic range, the vertically integrated sensor array (VISA) program has been sponsored by DARPA.<sup>25–27</sup> The approach being developed builds on the traditional “hybrid” structure of a detector with a 2D array of indium-bump interconnects to the silicon readout. VISA allows additional layers of silicon processing chips to be connected below the readout to provide more complex functionality. It will allow the use of smaller and multicolor detectors without compromising storage capacity. Signal-to-noise ratios will increase for multicolor FPAs. This will permit LWIR FPAs to improve the sensitivity by a factor of 10.

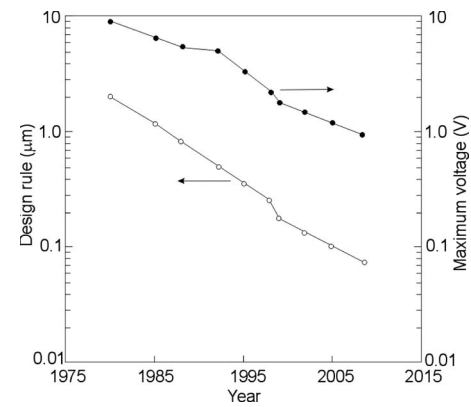


FIG. 6. Trends for design rule minimum and maximum bias voltage of silicon foundry requirements (after Ref. 1).

## B. Pixel and chip sizes

Pixel and chip sizes are important issues in association with multicolor imager formats. Small pixels reduce cost by increasing the number of readout and detector dice potentially available from processed wafers. Small pixels also allow smaller, light-weight optics to be used.

The fundamental limit to pixel size is determined by diffraction. The size of the diffraction-limited optical spot or Airy disk is given by

$$d = 2.44\lambda f, \quad (9)$$

where  $d$  is the diameter of the spot,  $\lambda$  is the wavelength, and  $f$  is the  $f$ -number of the focusing lens. For typical  $f/2.0$  optics at 5  $\mu$ m wavelength, the spot size is 25  $\mu$ m. Because system users prefer some degree of oversampling, the pixel size may be reduced for MWIR applications to dimensions on the order of 12  $\mu$ m. Given the track record of human nature, Norton<sup>13</sup> predicted that MWIR pixel size will eventually be reduced to about 10  $\mu$ m at some point, just to achieve the smaller pixel record. Short-wavelength IR (SWIR) pixel size will shrink to correspondingly smaller dimensions, for applications seeking maximum spatial resolution. LWIR pixels are not likely to shrink much below 20  $\mu$ m. However, it is anticipated that LWIR pixels will be made as small as MWIR pixels, since this will allow a single readout design then to be used with both MWIR and LWIR FPAs.

Readout circuit wafers are processed in standard commercial foundries and can be constrained in size by the die-size limits of the photolithography step and repeat printers.<sup>1</sup> This limit is currently on the order of  $22 \times 22$  mm<sup>2</sup> for sub-micron lithography. Thus, the array itself can only occupy  $18 \times 18$  mm<sup>2</sup> assuming one needs about 2 mm on each side for the peripheral circuitry such as bias supplies, shift registers, column amplifiers, and output drivers. Under these conditions, a  $1024 \times 1024$  array would need to have pixels no larger than 18  $\mu$ m.

To build larger sensor arrays, a new photolithographic technique called *stitching* can be used to fabricate detector arrays larger than the reticle field of photolithographic steps. The large array is divided into smaller subblocks. Later, the complete sensor chips are stitched together from the

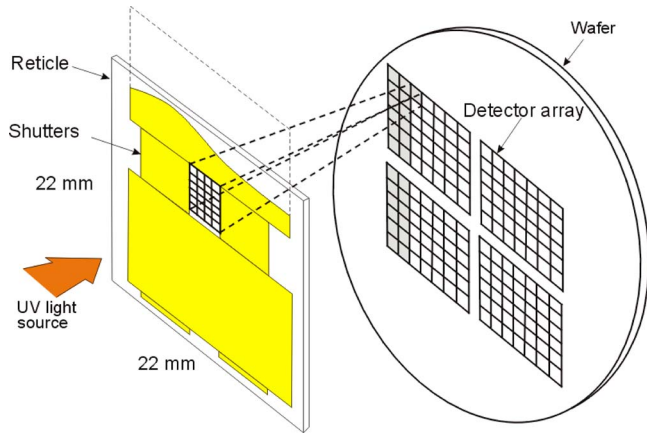


FIG. 7. (Color online) The photocomposition of a detector array die using array stitching based on photolithographic stepper.

building blocks in the reticle as shown in Fig. 7. Each block can be photocomposed on the wafer by multiple exposures at appropriate locations. Single blocks of the detector array are exposed at one time, as the optical system allows shuttering, or selectively exposing only a desired section of the reticle.

III-V compound semiconductors are available in large diameter wafers, up to 8 in. in the case of GaAs wafers. Thus, focal plane technologies such as InSb, QWIP, and type-II SLS are potential candidates for development of large-format arrays such as  $4096 \times 4096$  and larger. Gunapala *et al.*<sup>28</sup> have discussed the possibility of extending the array size up to 16 megapixels.

It should be noted that stitching creates a seamless detector array, as opposed to an assembly of closely butted subarrays. The butting technique is commonly used in the fabrication of very large-format HgCdTe hybrid sensor arrays due to the limited size of substrate wafers (usually CdZnTe). For example, Teledyne Scientific & Imaging has developed the world's largest HgCdTe SWIR FPA for astronomy and low-background applications. The format of the device is a hybrid  $2048 \times 2048$  with a unit cell size of  $18 \times 18 \mu\text{m}^2$  and with active size of 37 mm. Sets of four arrays are "tiled" into a  $2 \times 2$  mosaic configuration giving  $4096 \times 4096$  pixels.<sup>29</sup>

Recently, the first large-format MWIR FPAs with pixel dimension of  $15 \mu\text{m}$  have been demonstrated.<sup>30,31</sup> It will be an extreme challenge to deploy a two- or three-color detector structure into a small pixel such as  $18 \times 18 \mu\text{m}^2$ . Current two-color simultaneous mode pixels with two indium bumps per pixel have not been built with pixels smaller than  $25 \mu\text{m}$  on a side.

### C. Uniformity

It is well known that, when the detectivity is approaching a value above  $10^{10} \text{ cm Hz}^{1/2}/\text{W}$ , the FPA performance is uniformity limited prior to correction and thus essentially independent of the detectivity (see Fig. 8). An improvement in nonuniformity from 0.1% to 0.01% after correction could lower the NEDT from 63 to 6.3 mK.

The nonuniformity value is usually calculated using the standard deviation over mean, counting the number of oper-

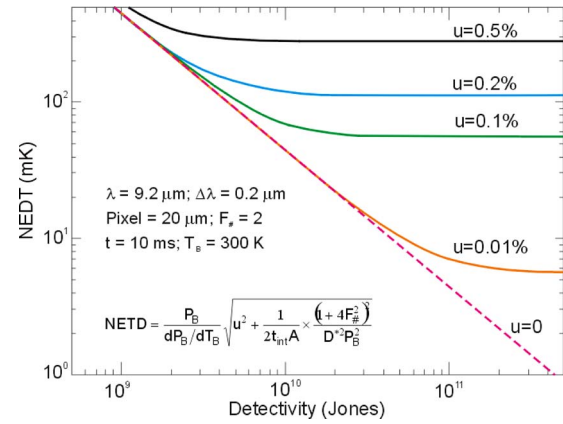


FIG. 8. (Color online) NEDT as a function of detectivity. The effects of nonuniformity are included for  $u=0.01\%$ ,  $0.1\%$ ,  $0.2\%$ , and  $0.5\%$ . Note that for  $D^* > 10^{10} \text{ cm Hz}^{1/2}/\text{W}$ , detectivity is not the relevant figure of merit.

able pixels in an array. For a system operating in the LWIR band, the scene contrast is about 2%/K of change in scene temperature. Thus, to obtain a pixel to pixel variation in apparent temperature to less than, e.g., 20 mK, the nonuniformity in response must be less than 0.04%. This is almost impossible to obtain in the uncorrected response of the FPA, so a two-point correction is typically used.

FPA uniformity influences the IR system complexity. The uniformity is important for accurate temperature measurements, background subtraction, and threshold sensing. Nonuniformities require elaborate compensation algorithms to correct the image, and by consuming a number of analog-to-digital bits they also reduce the system dynamic range.

Tactical IR FPAs usually require operation in the LWIR window, with a smaller number of applications in the  $3\text{--}5 \mu\text{m}$  window. Ranges from the sensor to the target are typically short, allowing for use of imaging sensors with large FPAs where precise radiometry is not critical. Imaging arrays can usually tolerate some percentage of dead or degraded pixels without jeopardizing mission performance. Tactical backgrounds in the IR windows are relatively high, with about  $10^{16}$  photons/ $\text{cm}^2 \text{ s}$  reaching the detector.

Table I shows the uncertainty in cutoff wavelength of  $\text{Hg}_{1-x}\text{Cd}_x\text{Te}$  for  $x$  variations of 0.1%. For short-wavelength IR ( $\approx 3 \mu\text{m}$ ) and MWIR ( $\approx 5 \mu\text{m}$ ) materials, the variation in cutoff wavelength is not large. However, the nonuniformity is a serious problem in the case of LWIR HgCdTe detectors. The variation in  $x$  across the  $\text{Hg}_{1-x}\text{Cd}_x\text{Te}$  wafer causes much larger spectral nonuniformity; e.g., at 77 K, a variation of  $\Delta x=0.2\%$  gives a  $\Delta \lambda_c=0.064 \mu\text{m}$  at  $\lambda_c$

TABLE I. Cutoff wavelength for  $x$  variations of 0.1% and the corresponding cutoff wavelength shift for  $\text{Hg}_{1-x}\text{Cd}_x\text{Te}$  at 77 K.

Composition $x$	Cutoff wavelength $\lambda_c$ ( $\mu\text{m}$ )	Uncertainty $\Delta \lambda_c$ ( $\mu\text{m}$ )
0.395	3	0.012
0.295	5	0.032
0.210	10	0.131
0.196	14	0.257
0.187	20	0.527



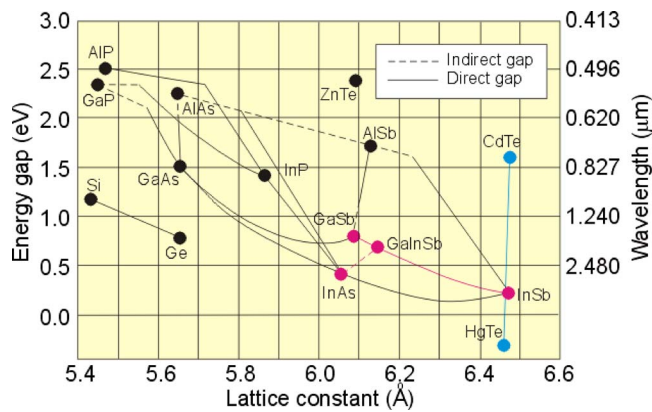


FIG. 9. (Color online) Composition and wavelength diagram of Sb-based III-V material systems.

$=5 \mu\text{m}$ , but  $\Delta\lambda_c=0.51 \mu\text{m}$  at  $14 \mu\text{m}$ , which cannot be fully corrected by either two or three point corrections.<sup>2</sup> Therefore material composition control is much more stringent for LWIR than for MWIR. For applications that require operation in the LWIR band as well as two-color LWIR/VLWIR bands, most probably HgCdTe will not be the optimal solution.

Alternative candidate for third-generation IR detectors are the Sb-based III-V material system. These materials are mechanically robust and have fairly weak dependence of band gap on composition (see Fig. 9).

#### D. Identification and detection ranges

Thermal imaging systems are used first to detect an object, and then to identify it. Typically, identification ranges are between two and three times shorter than detection ranges.<sup>32</sup> To increase ranges, better resolution and sensitivity of the IR systems (and hence the detectors) are required. Third-generation cooled imagers are being developed to extend the range of target detection and identification and to ensure that defense forces maintain a technological advantage in night operations over any opposing force.

Identification ranges can be further increased by using multispectral detection to correlate the images at different wavelengths. For example, it appears that in the MWIR spectral range, the IR image is washed out to the point that the target and the background cannot be distinguished from each other (see Fig. 10). Detectors that cover the entire spectral range will suffer from washout because the background contrast changes from positive to negative. Alternatively, using two band detectors (up to  $3.8 \mu\text{m}$  and from  $3.8$  up to  $5 \mu\text{m}$ ) and summing the inverse of the second band and the output of the first band will yield a contrast enhancement that is impossible to achieve if an integrated response of the entire spectral range is used.

Figure 11 compares the relative detection and identification ranges modeled for third-generation imagers using NVESD's (Fort Belvoir, VA 22060) NVTHERM program. As a range criterion, the standard 70% probability of detection or identification is assumed. Note that the identification range in the MWIR range is almost 70% of the LWIR detection range. For detection, LWIR provides superior range. In the

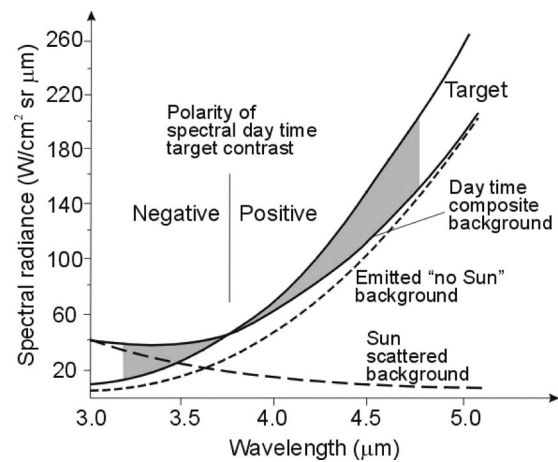


FIG. 10. Target and background contrast reversal in the MWIR spectral range (after Ref. 32).

detection mode, the optical system provides a wide field of view ( $f/2.5$ ) since third-generation systems will operate as an on-the-move wide area step scanner with automated target recognition (second-generation systems rely on manual target searching).<sup>33</sup> MWIR offers higher spatial resolution sensing and has an advantage for long-range identification when used with telephoto optics narrow field-of-view (NFOV) ( $f/6$ ).

#### VI. MATERIAL CONSIDERATIONS FOR THIRD-GENERATION IR DETECTORS

In the wavelength regions of interest such as SWIR, MWIR, and LWIR, four detector technologies that are developing multicolor capability are visited here: HgCdTe, QWIPs, antimonide based type-II SLs, and QDIPs.

Both HgCdTe photodiodes<sup>31,34–38</sup> and QWIPs<sup>2,28,32,39–44</sup> offer multicolor capability in the SWIR, MWIR, and LWIR ranges. The performance figures of merit of state-of-the-art QWIP and HgCdTe FPAs are similar because the main limitations are related to the readout circuits. A more detailed comparison of both technologies has been given by Tidrow *et al.*<sup>2</sup> and Rogalski.<sup>40,45</sup>

Recently, type-II InAs/GaInSb SLs<sup>42,46–49</sup> and QDIPs<sup>50–55</sup> have emerged as possible candidates for third-

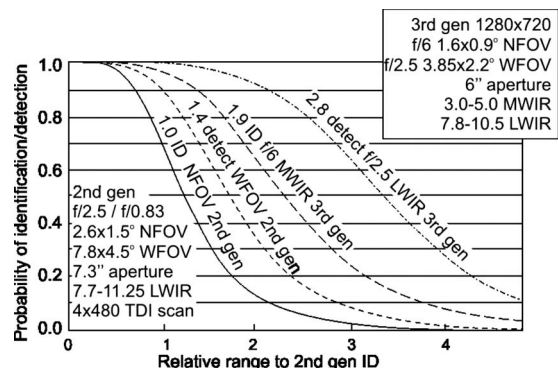


FIG. 11. Comparison of the detection and identification range between current second-generation TDI scanned LWIR imagers and the LWIR and MWIR bands of third-generation imager in a  $1280 \times 720$  format with  $20 \mu\text{m}$  pixels (after Ref. 33).

TABLE II. Summary of the material properties for the  $\text{Hg}_{1-x}\text{Cd}_x\text{Te}$  ternary alloy, listed for the binary components HgTe and CdTe, and for several technologically important alloy compositions (after Ref. 56).  $\tau_R$  and  $\tau_{A1}$  calculated for  $n$ -type HgCdTe with  $N_d = 1 \times 10^{15} \text{ cm}^{-3}$ . The last four material properties are independent of or relatively insensitive to alloy composition

Property $x$	HgTe 0	$\text{Hg}_{1-x}\text{Cd}_x\text{Te}$						CdTe 1.0
		0.194	0.205	0.225	0.31	0.44	0.62	
$a$ (Å)	6.461	6.464	6.464	6.464	6.465	6.468	6.472	6.481
	77 K	77 K	77 K	77 K	140 K	200 K	250 K	300 K
$E_g$ (eV)	-0.261	0.073	0.091	0.123	0.272	0.474	0.749	1.490
$\lambda_c$ (μm)	...	16.9	13.6	10.1	4.6	2.6	1.7	0.8
$n_i$ (cm <sup>-3</sup> )	...	$1.9 \times 10^{14}$	$5.8 \times 10^{13}$	$6.3 \times 10^{12}$	$3.7 \times 10^{12}$	$7.1 \times 10^{11}$	$3.1 \times 10^{10}$	$4.1 \times 10^5$
$m_e/m_o$	...	0.006	0.007	0.010	0.021	0.035	0.053	0.102
$g_c$	...	-150	-118	-84	-33	-15	-7	-1.2
$\epsilon_s/\epsilon_o$	20.0	18.2	18.1	17.9	17.1	15.9	14.2	10.6
$\epsilon_\infty/\epsilon_o$	14.4	12.8	12.7	12.5	11.9	10.8	9.3	6.2
$n_r$	3.79	3.58	3.57	3.54	3.44	3.29	3.06	2.50
$\mu_e$ (cm <sup>2</sup> /V s)	...	$4.5 \times 10^5$	$3.0 \times 10^5$	$1.0 \times 10^5$	...	...	...	...
$\mu_{hh}$ (cm <sup>2</sup> /V s)	...	450	450	450	...	...	...	...
$b = \mu_e/\mu_\eta$	...	1000	667	222	...	...	...	...
$\tau_R$ (μs)	...	16.5	13.9	10.4	11.3	11.2	10.6	2
$\tau_{A1}$ (μs)	...	0.45	0.85	1.8	39.6	453	$4.75 \times 10^3$	...
$\tau_{\text{typical}}$ (μs)	...	0.4	0.8	1	7	...	...	...
$E_p$ (eV)				19				
$\Delta$ (eV)				0.93				
$m_{hh}/m_o$				0.40-0.53				
$\Delta E_v$ (eV)				0.35-0.55				

generation IR detectors. Whether the low dimensional solid IR photodetectors can outperform the “bulk” narrow gap HgCdTe detectors is one of the most important questions that needs to be addressed for the future of IR photodetectors.

The subsections below describe issues associated with the development and exploitation of materials used in the fabrication of multicolor IR detectors.

### A. HgCdTe

The HgCdTe ternary alloy is a close to ideal IR detector material system. Its unique position is dependent on three key features:

- composition-dependent tailorable energy band gap over the entire 1–30 μm range,

- large optical coefficients that enable high quantum efficiency, and
- favorable inherent recombination mechanisms that lead to long carrier lifetime and high operating temperature.

These properties are a direct consequence of the energy band structure of this zinc-blende semiconductor. Moreover, additional specific advantages of HgCdTe are the ability to obtain both low and high carrier concentrations, high mobility of electrons, and low dielectric constant. The extremely small change in lattice constant with composition makes it possible to grow high quality layered and graded gap structures. As a result, HgCdTe can be used for detectors operated in various modes, photoconductor, photodiode, or metal-insulator-semiconductor detector.

TABLE III. Some physical properties of narrow gap semiconductors.

Material	$E_g$ (eV)		$n_i$ (cm <sup>-3</sup> )		$\epsilon$	$\mu_e$ (10 <sup>4</sup> cm <sup>2</sup> /V s)		$\mu_h$ (10 <sup>4</sup> cm <sup>2</sup> /V s)	
	77 K	300 K	77 K	300 K		77 K	300 K	77 K	300 K
InAs	0.414	0.359	$6.5 \times 10^3$	$9.3 \times 10^{14}$	14.5	8	3	0.07	0.02
InSb	0.228	0.18	$2.6 \times 10^9$	$1.9 \times 10^{16}$	17.9	100	8	1	0.08
$\text{In}_{0.53}\text{Ga}_{0.47}\text{As}$	0.66	0.75		$5.4 \times 10^{11}$	14.6	7	1.38		0.05
PbS	0.31	0.42	$3 \times 10^7$	$1.0 \times 10^{15}$	172	1.5	0.05	1.5	0.06
PbSe	0.17	0.28	$6 \times 10^{11}$	$2.0 \times 10^{16}$	227	3	0.10	3	0.10
PbTe	0.22	0.31	$1.5 \times 10^{10}$	$1.5 \times 10^{16}$	428	3	0.17	2	0.08
$\text{Pb}_{1-x}\text{Sn}_x\text{Te}$	0.1	0.1	$3.0 \times 10^{13}$	$2.0 \times 10^{16}$	400	3	0.12	2	0.08
$\text{Hg}_{1-x}\text{Cd}_x\text{Te}$	0.1	0.1	$3.2 \times 10^{13}$	$2.3 \times 10^{16}$	18.0	20	1	0.044	0.01
$\text{Hg}_{1-x}\text{Cd}_x\text{Te}$	0.25	0.25	$7.2 \times 10^8$	$2.3 \times 10^{15}$	16.7	8	0.6	0.044	0.01

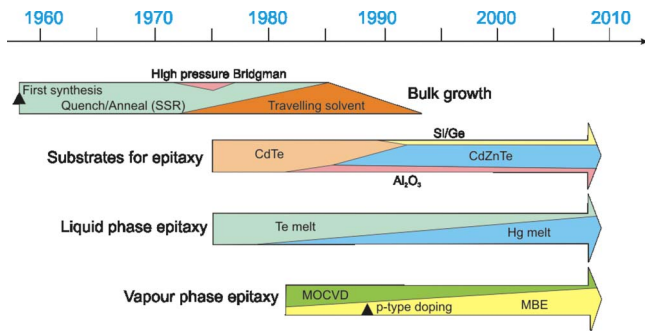


FIG. 12. (Color online) Evolution of HgCdTe crystal growth technology from 1958 to present (after Ref. 57).

Table II summarizes the various material properties of  $\text{Hg}_{1-x}\text{Cd}_x\text{Te}$ , and Table III compares important parameters of HgCdTe with other narrow gap semiconductors used in IR detector fabrication.

### 1. Outlook on crystal growth

Third-generation HgCdTe IR systems have emerged as a result of technological achievements in the growth of heterostructure devices used in the production of second-generation IR FPAs. The time line for the evolution of crystal growth technologies is illustrated in Fig. 12. Historically, crystal growth of HgCdTe has been a major problem mainly because a relatively high Hg pressure is present during growth, which makes it difficult to control the stoichiometry and composition of the grown material. The wide separation between the liquidus and solidus, leading to marked segregation between CdTe and HgTe, was instrumental in slowing the development of all the bulk growth techniques to this system. In addition to solidus-liquidus separation, high Hg partial pressures are also influential both during growth and postgrowth heat treatments.

Early experiments and a significant fraction of early production were undertaken using a quench-anneal or solid-state recrystallization process. In this method the charge of a required composition was synthesized, melted, and quenched. Then, the fine dendritic mass (highly polycrystalline solid)

obtained in the process was annealed below the liquidus temperature for a few weeks to recrystallize and homogenize the crystals. The material usually requires low-temperature annealing in order to adjust the concentration of native defects. The crystals can also be uniformly doped by the introduction of dopants to the charge.

Bridgman growth was attempted for several years near the mid-1970s of the last century. At the same time, solvent growth methods from Te-rich melts were initiated to reduce the growth temperature. One successful implementation was the traveling heater method which resulted in crystals up to 5 cm diameter. The perfect quality of crystals grown by this method is achieved at the cost of a low growth rate.

Bulk HgCdTe crystals were initially used for all types of IR photodetectors. At present they are still used for some IR applications such as *n*-type single element photoconductors, signal processing in the element (SPRITE) detectors, and linear arrays. Bulk growth produced thin rods, generally up to 15 mm in diameter, about 20 cm in length, and with a nonuniform distribution of composition. Large 2D arrays could not be realized with bulk crystals. Another drawback to bulk material was the need to thin the bulk wafers, usually cut to about 500  $\mu\text{m}$  down to a final device thickness of about 10  $\mu\text{m}$ . Also, further fabrication steps (polishing the wafers, mounting them to suitable substrates, and polishing to the final device thickness) was very labor intensive.

In comparison with bulk growth techniques, epitaxial techniques offer the possibility of growing large area epilayers and fabrication of sophisticated device structures with good lateral homogeneity and abrupt and complex composition and doping profiles, which can be configured to improve the performance of photodetectors. The growth is performed at low temperatures, which makes it possible to reduce the native defect density. The properties of HgCdTe grown by the various techniques discussed here are summarized in Table IV.

Among the various epitaxial techniques, liquid phase epitaxy (LPE) is the most technologically mature method. LPE is a single crystal growth process in which growth from a cooling solution occurs onto a substrate. Another technique,

TABLE IV. Comparison of the various methods used to grow HgCdTe (after Ref. 57).

	Bulk			LPE		Vapor phase epitaxy	
	SSR	Traveling heater method HCT melt	Te melt	Hg melt	Te melt	MOCVD	MBE
Temperature ( $^{\circ}\text{C}$ )	950	950	500	350–550	400–550	275–400	160–200
Pressure (Torr)	150 000	150 000	760–8000	760–114 00	760–8000	300–760	$10^{-3}$ – $10^{-4}$
Growth rate ( $\mu\text{m/h}$ )	250	250	80	30–60	5–60	2–10	1–5
Dimensions <i>w</i> (cm)	0.8–1.2 dia	0.8–1.2 dia	2.5 dia	5	5	7.5 dia	7.5 dia
<i>l</i> (cm)	...	...	...	6	5	4	4
<i>t</i> (cm)	15	15	15	0.0002–0.0030	0.0005–0.012	0.0005–0.001	0.0005–0.001
Dislocations ( $\text{cm}^{-2}$ )	$<10^5$	...	$<10^5$	$<10^5$	$<10^5$ – $10^7$	$5 \times 10^5$ – $10^7$	$<5 \times 10^4$ – $10^6$
Purity ( $\text{cm}^{-3}$ )	$<5 \times 10^{14}$	$<5 \times 10^{14}$	$<5 \times 10^{14}$	$<5 \times 10^{14}$	$<5 \times 10^{14}$	$<1 \times 10^{15}$	$<1 \times 10^{15}$
<i>n</i> -type doping ( $\text{cm}^{-3}$ )	N/A	N/A	N/A	$1 \times 10^{14}$ – $1 \times 10^{18}$	$1 \times 10^{15}$ – $1 \times 10^{16}$	$5 \times 10^{14}$ – $5 \times 10^{18}$	$5 \times 10^{14}$ – $1 \times 10^{19}$
<i>p</i> -type doping ( $\text{cm}^{-3}$ )	N/A	N/A	N/A	$1 \times 10^{15}$ – $1 \times 10^{18}$	$1 \times 10^{15}$ – $5 \times 10^{16}$	$3 \times 10^{15}$ – $5 \times 10^{17}$	$1 \times 10^{16}$ – $5 \times 10^{18}$
X-ray rocking curve (arc sec)	...	...	20–60	$<20$	$<20$	50–90	20–30
Compositional uniformity ( $\Delta x$ )	$<0.002$	$<0.004$	$<0.005$	$<0.002$	$<0.002$	$\pm 0.01$ – $0.0005$	$\pm 0.01$ – $0.0006$



vapor phase epitaxial growth of HgCdTe is typically carried out by nonequilibrium methods which also apply to metal organic chemical vapor deposition (MOCVD), molecular beam epitaxy (MBE), and their derivatives. The great potential benefit of MBE and MOCVD over equilibrium methods is the ability to modify the growth conditions dynamically during growth to tailor band gaps, add and remove dopants, prepare surfaces and interfaces, add passivations, perform anneals, and even grow on selected areas of a substrate. The growth control is exercised with great precision to obtain basic material properties comparable to those routinely obtained from equilibrium growth.

Epitaxial growth of HgCdTe layers requires a suitable substrate. CdTe was used initially, since it was available from commercial sources in reasonably large sizes. The main drawback to CdTe is that it has a few percent lattice mismatch with LWIR and MWIR HgCdTe. By the mid-1980s last century it was demonstrated that the addition of a few percent of ZnTe to CdTe (typically 4%) could create a lattice matched substrate. CdTe and closely lattice matched CdZnTe substrates are typically grown by the modified vertical or horizontal unseeded Bridgman technique. Most commonly the (111) and (100) orientations have been used, although others have been tried. Twinning which occurs in (111) layers can be prevented by a suitable misorientation of the substrate. Growth conditions found to be nearly optimal for the (112)B orientation were selected. The limited size, purity problems, Te precipitates, dislocation density (routinely in the low  $10^4 \text{ cm}^{-2}$  range), nonuniformity of lattice match, and high price (\$50–\$500 per  $\text{cm}^2$ , polished) are remaining problems to be solved. It is believed that these substrates will continue to be important for a long time, particularly for highest performance devices.

LPE growth of a thin layer of HgCdTe on CdTe substrates began in the early to mid-1970s. Initially, Te solutions with dissolved Cd (Cd has a high solubility in Te) and saturated with Hg vapor were used to efficiently grow HgCdTe in the temperature range of 420–600 °C. This allowed small-volume melts to be used with slider techniques which did not appreciably deplete during the growth run. Experiments with Hg-solvent LPE began in the late 1970s. Because of the limited solubility of Cd in Hg, the volume of the Hg melts had to be much larger than Te melts (typically about 20 kg) in order to minimize melt depletion during layer growth in the temperature range of 380–500 °C. This precluded the slider growth approach and Hg-melt epitaxy has been developed using large dipping vessels.

In the early 1990s, bulk growth was replaced by LPE and is now very mature for the production of first- and second-generation detectors. However, LPE technology is limited for a variety of advanced HgCdTe structures required for third-generation detectors. LPE typically melts off a thin layer of the underlying material each time an additional layer is grown due to the relatively high growth temperature. Additionally, the gradient in  $x$ -value in the base layer of  $p^+$ -on- $n$  junctions can generate a barrier to carrier transport in certain cases due to interdiffusion. These limitations have provided an opportunity for vapor phase epitaxy: MBE and MOCVD.

The era of MBE and MOCVD growth of HgCdTe began in the early 1980s by adopting both methods that had been well established in the III-V semiconductor materials. Through the following decade a variety of metal organic compounds were developed along with a number of reaction-chamber designs. In the case of MBE, a specially designed Hg-source oven was successfully designed to overcome the low sticking coefficient of Hg at the growth temperature. The growth temperature is less than 200 °C for MBE, but around 350 °C for MOCVD, making it more difficult to control  $p$ -type doping in MOCVD due to the formation of Hg vacancies at higher growth temperatures. At present, MBE is the dominant vapor phase method for the growth of HgCdTe. It offers low-temperature growth under an ultrahigh vacuum environment, *in situ*  $n$ -type and  $p$ -type doping, and control of composition, doping, and interfacial profiles. MBE is now the preferred method for growing complex layer structures for multicolor detectors and for avalanche photodiodes. Although the quality of MBE material is not yet on a par with LPE, it has made tremendous progress in the past decade. A key to its success has been the doping ability and the reduction in etch pit densities (EPDs) to below  $10^5 \text{ cm}^{-2}$ .

Near lattice matched CdZnTe substrates have severe drawbacks such as lack of large area, high production cost, and, more importantly, a difference in thermal expansion coefficient between the CdZnTe substrates and the silicon ROIC. Furthermore, interest in large area 2D IR FPAs ( $1024 \times 1024$  and larger) have resulted in limited applications of CdZnTe substrates. Currently, readily producible CdZnTe substrates are limited to areas of approximately  $50 \text{ cm}^2$ . At this size, the wafers are unable to accommodate more than two  $1024 \times 1024$  FPAs. Not even a single die can be accommodated for very large FPA formats ( $2048 \times 2048$  and larger) on substrates of this size.

The use of Si substrates is very attractive in IR FPA technology not only because it is less expensive and available in large area wafers but also because the coupling of the Si substrates with Si readout circuitry in a FPA structure allows fabrication of very large arrays exhibiting long-term thermal cycle reliability. The  $7 \times 7 \text{ cm}^2$  bulk CdZnTe substrate is the largest commercially available, and it is unlikely to increase much larger than its present size. With the cost of 6 in. Si substrates being  $\approx \$100$  versus  $\$10\,000$  for the  $7 \times 7 \text{ cm}^2$  CdZnTe, significant advantages of HgCdTe/Si are evident.<sup>58</sup> Despite the large lattice mismatch ( $\approx 19\%$ ) between CdTe and Si, MBE has been successfully used for the heteroepitaxial growth of CdTe on Si. Using optimized growth condition for Si(211)B substrates and a CdTe/ZnTe buffer system, epitaxial layers with EPD in the  $10^6 \text{ cm}^{-2}$  range have been obtained. This value of EPD has little effect on both MWIR and LWIR HgCdTe/Si detectors.<sup>58,59</sup> By comparison, HgCdTe epitaxial layers grown by MBE or LPE on bulk CdZnTe have typical EPD values in the  $10^4$  to mid- $10^5 \text{ cm}^{-2}$  range where there is a negligible effect of dislocation density on detector performance. At 77 K, diode performance with cutoff wavelength in LWIR region for HgCdTe on Si is comparable to that on bulk CdZnTe substrates.<sup>59</sup>

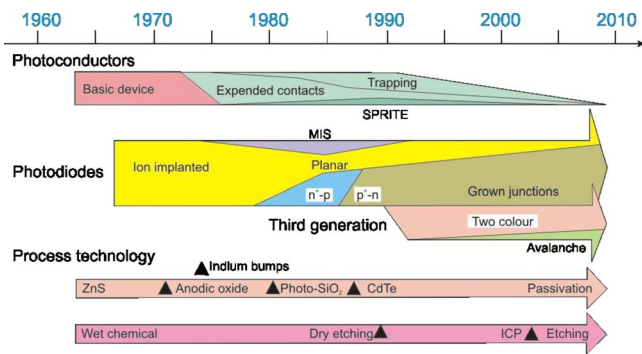


FIG. 13. (Color online) A time line of the evolution of HgCdTe IR detectors and key developments in process technology which made them possible (after Ref. 57).

Sapphire has also been widely used as a substrate for HgCdTe epitaxy. In this case a CdTe (CdZnTe) film is deposited on the sapphire prior to the growth of HgCdTe. This substrate has excellent physical properties and can be purchased in large wafer sizes. The large lattice mismatch with HgCdTe is accommodated by a CdTe buffer layer. Sapphire is transparent from the UV to about  $6\text{ }\mu\text{m}$  in wavelength and has been used in back side-illuminated SWIR and MWIR detectors (it is not acceptable for back side-illuminated LWIR arrays because of its opacity beyond  $6\text{ }\mu\text{m}$ ).

## 2. HgCdTe photodiodes

A number of different HgCdTe photodiode architectures have been developed. The time evolution of this development is illustrated in Fig. 13. The development of multicolor HgCdTe detectors has emerged from the two most important junction architectures based on  $n$ -on- $p$  homojunctions (Figs. 14 and 15) and  $p$ -on- $n$  heterojunctions (Fig. 16).

To avoid contribution from tunneling currents, low doping concentration in the base region is required. In both photodiode structures, the lightly doped narrow gap absorbing region ("base" of the photodiode:  $p(n)$ -type carrier concentration of about  $5 \times 10^{15}\text{ cm}^{-3}$  ( $5 \times 10^{14}\text{ cm}^{-3}$ )) determines the dark current and photocurrent. The internal electric fields at interfaces are "blocking" for minority carriers and influence of surface recombination is eliminated. Also, suitable passivation negates the influence of surface recombination. Indium is most frequently used as a well-controlled dopant for  $n$ -type doping due to its high solubility and moderately high diffusion. Elements of the VB group are acceptors sub-

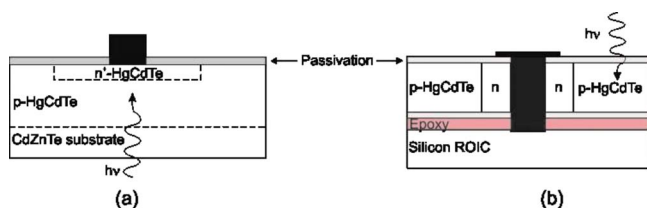


FIG. 14. (Color online) Cross sections of  $n$ -on- $p$  homojunction HgCdTe photodiodes formatted by (a) ion implantation into acceptor-doped (usually Hg vacancies)  $p$ -type LPE film grown by Te-solution slider (Sofradir), (b) ion beam milling, which forms  $n$ -type islands in  $p$ -type Hg-vacancy doped layer grown by Te-solution LPE on CdZnTe, and epoxied onto silicon ROIC wafer (cylindrical lateral collection diodes).

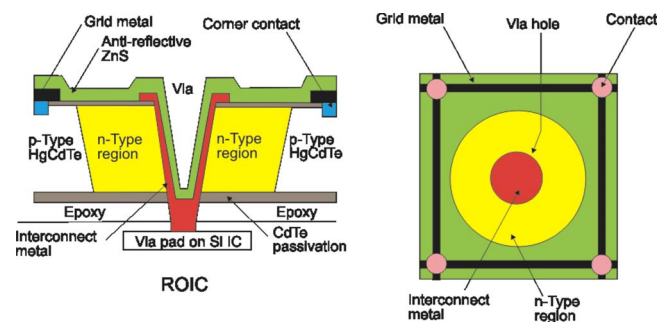


FIG. 15. (Color online) DRS's high-density vertically integrated photodiode (HDVIP™)  $n^+-n-p$  HgCdTe photodiode (after Ref. 63).

stituting at Te sites. They are very useful for fabrication of stable junctions due to very low diffusivity. Arsenic has proven to be the most successful  $p$ -type dopant to date. The main advantages are stability in the lattice, low activation energy, and possibility to control concentration over the  $10^{15}$ – $10^{18}\text{ cm}^{-3}$  range. Intensive efforts are currently underway to reduce the high temperature ( $\approx 400\text{ }^\circ\text{C}$ ) required to activate As as an acceptor.

The low binding energies and ionic bond nature of HgCdTe give rise to two important effects, which are influential in most junction-forming processes. The first is the role of Hg, which is liberated readily by processes such as ion implantation and ion beam milling. This creates a much deeper  $n$ -on- $p$  junction than would be expected from the implantation range. A second effect is the role of dislocations, which may play a part in annihilating vacancies. The role of Hg interstitials, dislocations, and ion bombardment in the junction-forming process is complex and not well understood in detail. Despite the complex physics involved, manufacturers have received good phenomenological control of the junction depth and dopant profiles with a variety of processes. Recently, epitaxial techniques using doping during growth are most often used for preparing  $p$ -on- $n$  junctions. LPE, MBE, and MOCVD have all been successfully accomplished with As doping during growth (see Fig. 13).

Figure 14 shows cross sections of the two most important  $n$ -on- $p$  HgCdTe junction structures adapted in fabrication of multicolor detectors. The structure (a) pioneered by Societe Anonyme de Telecommunications<sup>60</sup> (SAT) has been the most widely developed and used by Sofradir. The second type of structure shown in Fig. 14(b) is a vertically integrated photodiode (VIP™) developed by DRS Infrared Technologies.<sup>61</sup> This structure, currently referred to as a high-density vertically integrated photodiode (HDVIP) is similar to the British-developed loop-hole photodiode.<sup>62,63</sup>

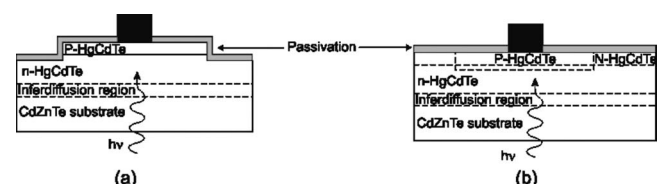


FIG. 16. Cross sections of  $p$ -on- $n$  DLHJ HgCdTe photodiodes: (a) mesa structure; (b) planar structure. The active  $n$ -type regions are sandwiched between CdZnTe substrates and high-doped, wider-gap regions.

This  $n^+-n^-p$  architecture is formed around the via, both by the etching process itself and by a subsequent ion implant step. Low-background indium  $n^-$ -doping levels of  $1.5$  to  $5 \times 10^{14} \text{ cm}^{-3}$  are routinely used. The  $p$ -type dopant is usually copper (acceptor concentration about  $4 \times 10^{16} \text{ cm}^{-3}$ ). The  $p^+-p$  noninjection contacts are formed in each cell of the FPA and are joined electrically by a top surface metal grid as shown in Fig. 15.

The cross sections of the second type of structure, heterojunction  $p$ -on- $n$  HgCdTe photodiode are illustrated in Fig. 16. In these so-called double-layer heterojunction (DLHJ) structures, an absorber layer about  $10 \mu\text{m}$  thick is doped with indium at  $1 \times 10^{15} \text{ cm}^{-3}$  or less and is sandwiched between the CdZnTe substrate and the highly arsenic-doped, wider-gap region. Contacts are made to the  $p^+$ -layer in each pixel and to the common  $n$ -type layer at the edge of the array (not shown). IR flux is incident through the IR-transparent substrate.

The formation of planar  $p$ -on- $n$  photodiodes [see Fig. 16(b)] is achieved by selective area arsenic ion implantation through the cap layer into the narrow-gap base layer.<sup>64</sup> Dopant activation step is achieved by a two-step thermal annealing under Hg overpressure: the first step, at high temperature, activates the dopant by substituting As atoms on the Te sublattice, and the second, at lower temperature, annihilates the Hg vacancies formed in the HgCdTe lattice during growth and high-temperature annealing step.

The key technology needed to make high-performance photodiodes was surface passivation. Passivation technologies can be classified into three categories: native films (oxides, sulfides, fluorides), deposited dielectrics ( $\text{ZnS}$ ,  $\text{SiO}_x$ ,  $\text{Si}_3\text{N}_4$ , polymers), and *in situ* grown heterostructures where a wider bandgap material is the passivant.<sup>65,66</sup> A two-layer combination of a thick deposited dielectric film on a thin native film of wider bandgap material is often the preferred passivation. Based on the success in silicon technology, passivation efforts were initially focused mainly on native oxides. Anodic oxide was adequate for photoconductors due to their fixed positive charge. However, when applied to photodiodes, anodic oxide shorted out the devices by inverting the  $p$ -type surface. Silicon oxide was employed for photodiode passivation in the early 1980s, based on low-temperature deposition using a photochemical reaction. It appears, however, that the excellent surface properties (with low interface trap densities and excellent photodiode properties) could not be maintained when the devices were heated in vacuum for extended periods of time, a procedure required for good vacuum packaging integrity. Also, surface charge buildup occurred when the devices were operated in a space-radiation environment. Recent efforts are concentrated mostly on passivation with CdTe and CdZnTe. Much of the pioneering work in this area was initially undertaken in France at Societe Anonyme de Telecommunication (SAT) in the mid-1970s.<sup>67,68</sup> CdZnTe passivation is stable during vacuum packaging bake cycles and shows little effect from the radiation found in space applications. The diodes do not show variation in the  $R_0A$  product with diode size, indicating that surface perimeter effects can be neglected.

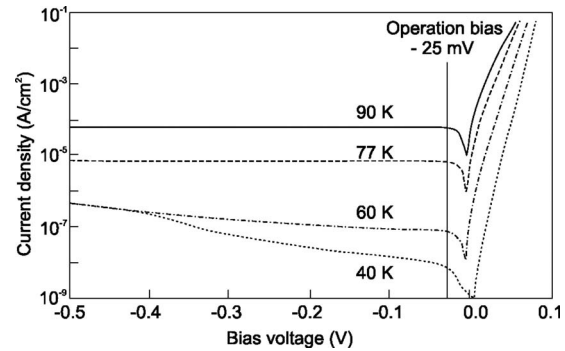


FIG. 17. Current-voltage characteristics at various temperatures for a  $12 \mu\text{m}$  cutoff HgCdTe photodiode.

In ideal photodiodes the diffusion current is dominant, indicating that leakage current is very low and insensitive to detector bias. Leakage current is the primary contributor to unwanted noise. Figure 17 shows typical current-voltage characteristics of an HgCdTe photodiode at temperatures between 40 and 90 K for a  $12 \mu\text{m}$  cutoff detector (at 40 K). The leakage current is less than  $10^{-5} \text{ A/cm}^2$  at 77 K. The bias-independent leakage current makes it easier to achieve better FPA uniformity, as well as to reduce the detector bias-control requirements during changes in photocurrent.

A key figure of merit of photodiodes is the  $R_0A$  product which should be maximized to reduce detector dark current and associated noise. Figure 18 illustrates the highest measurable  $R_0A$  values of  $p$ -on- $n$  HgCdTe photodiodes versus cutoff wavelength at different temperatures. The solid lines are theoretically calculated using a one-dimensional (1D) model that assumes diffusion current from narrower band gap  $n$ -side is dominant and minority carrier recombination via Auger and radiative process. The  $R_0A$  of Rockwell Scientific Company (RSC) HgCdTe photodiodes exhibit near theoretical performance for various growth material cutoffs at various temperatures.

The average value of the  $R_0A$  product at 77 K for a  $10 \mu\text{m}$  cutoff HgCdTe photodiode at 77 K is around

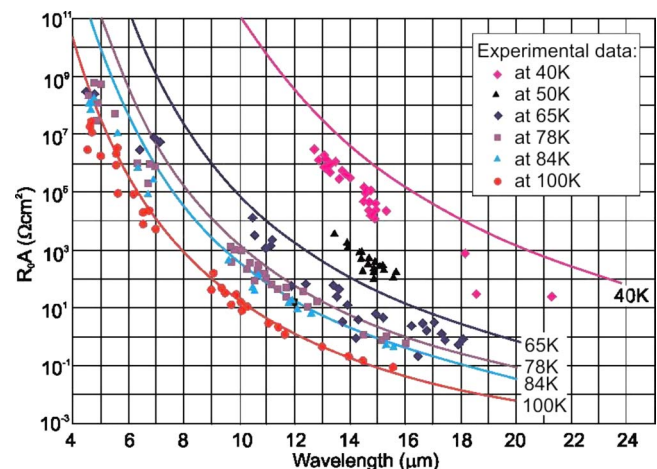


FIG. 18. (Color online)  $R_0A$  vs cutoff wavelength for RSC's  $P$ -on- $n$  HgCdTe photodiode data at various temperatures compared to the theoretical 1D diffusion model (after Ref. 69).



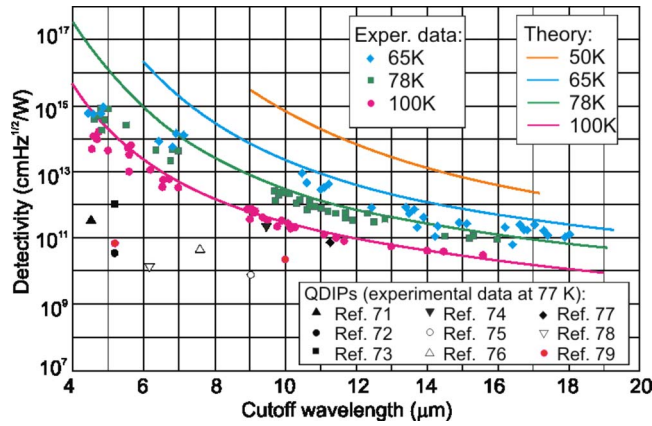


FIG. 19. (Color online) The measured (Teledyne Scientific and Imaging) and predicted detectivity of *P-on-n* HgCdTe photodiodes as a functions of wavelength and temperature (after Ref. 70). For comparison, the measured detectivities of QDIPs (Refs. 71–79) at 77 K are shown.

500  $\Omega \text{ cm}^2$  and drops to 50  $\Omega \text{ cm}^2$  at 12  $\mu\text{m}$  cutoff. At 40 K, the  $R_oA$  product varies between  $10^6$  and  $10^8 \Omega \text{ cm}^2$  for HgCdTe with a 11.2  $\mu\text{m}$  cutoff.

Figure 19 shows experimental detectivity data (Teledyne Scientific and Imaging) at 65, 78, and 100 K plotted as a function of cutoff wavelength. The solid lines are the theoretical  $D^*$  values given by

$$D^* = \frac{\eta \lambda q}{2hc} \left( \frac{R_o A}{kT} \right)^{1/2}, \quad (10)$$

calculated using typical values for the *n*-side donor concentration ( $N_d = 1 \times 10^{15} \text{ cm}^{-3}$ ), the narrow bandgap active layer thickness (10  $\mu\text{m}$ ), and the quantum efficiency (60%). The theory and measured data show good agreement over the entire wavelength and temperature range.

## B. QWIPs

Among the different types of QWIPs that have been developed, the technology based on GaAs–AlGaAs multiple-quantum-well detectors is the most mature. Rapid progress has recently been made in the performance of these detectors.<sup>39,80</sup> Detectivities have improved dramatically, and they are now high enough so that large  $1024 \times 1024$  FPAs with LWIR imaging performance comparable to state-of-the-art of HgCdTe are being fabricated.<sup>81,82</sup>

Despite large research and development efforts, large photovoltaic HgCdTe FPAs remain expensive, primarily because of the low yield of operable arrays. The low yield is due to the sensitivity of LWIR HgCdTe devices to defects and surface leakage, which is a consequence of basic material properties. With respect to HgCdTe detectors, GaAs/AlGaAs quantum-well devices have a number of potential advantages, including the use of standard manufacturing techniques based on mature GaAs growth and processing technologies, highly uniform and well-controlled MBE growth on greater than 6 in. GaAs wafers, high yield and thus low cost, higher thermal stability, and intrinsic radiation hardness. These detectors are extrinsic devices in which the dopant concentrations are limited by the epitaxial growth processes. As a result, the optical cross sections for absorp-

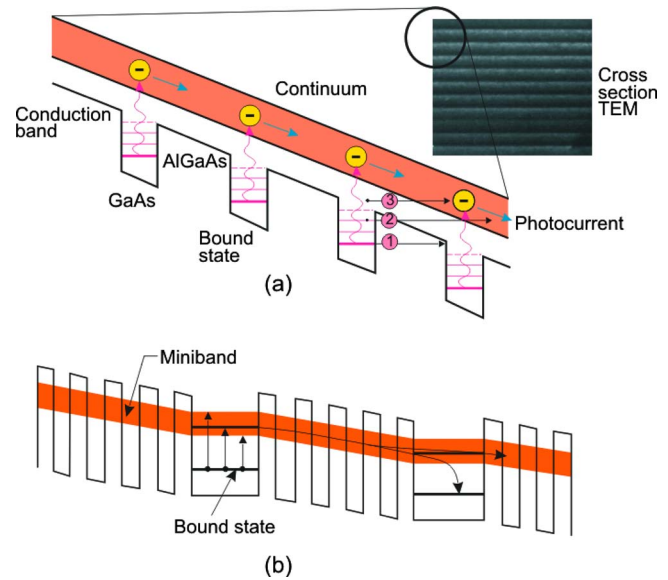


FIG. 20. (Color online) Band diagram of demonstrated QWIP structures: (a) bound to extended (after Ref. 83) and (b) bound to miniband. Three mechanisms creating dark current are also shown in (a): ground-state sequential tunneling (1), intermediate thermally assisted tunneling (2), and thermionic emission (3). The gray indicates extended states through which current flows.

tion are also limited. In addition, the intersubband lifetimes in QWIP detectors are inherently short (about  $10^{-11}$  s) which results in low quantum efficiency and relatively poor performance at temperatures  $> 50$  K. At these higher temperatures, thermally stimulated carriers dominate over optically produced carriers, resulting in a low signal-to-noise ratio. However, the signal-to-noise ratio is usually sufficient for the most common imaging applications.

All QWIPs are based on bandgap engineering of layered structures of wide-band-gap (relative to thermal IR energies) materials. The structure is designed such that the energy separation between two of the states in the structure matches the energy of the IR photons to be detected. Several QWIP configurations have been reported based on transitions from bound to extended states, from bound to quasibound states, from bound to quasibound states, and from bound to miniband states.

Figure 20 shows two detector configurations used in fabrication of multicolor QWIP FPAs. The major advantage of the bound-to-continuum QWIP [Fig. 20(a)] is that the photoelectron can escape from the QW to the continuum transport states without being required to tunnel through the barrier. As a result, the voltage bias required to efficiently collect the photoelectrons can be reduced dramatically, thereby lowering the dark current. Furthermore, since the photoelectrons are collected without having to tunnel through a barrier, the AlGaAs barriers can be made thicker without reducing the photoelectron collection efficiency. The multilayer structure consists of a periodic array of Si-doped ( $N_d \approx 10^{18} \text{ cm}^{-3}$ ) GaAs QWs of thickness  $L_w$  separated by undoped  $\text{Al}_x\text{Ga}_{1-x}\text{As}$  barriers of thickness  $L_b$ . The heavy *n*-type doping in the wells is required to ensure that freezeout does occur at low temperatures and that a sufficient number of electrons are available to absorb the IR radiation. For

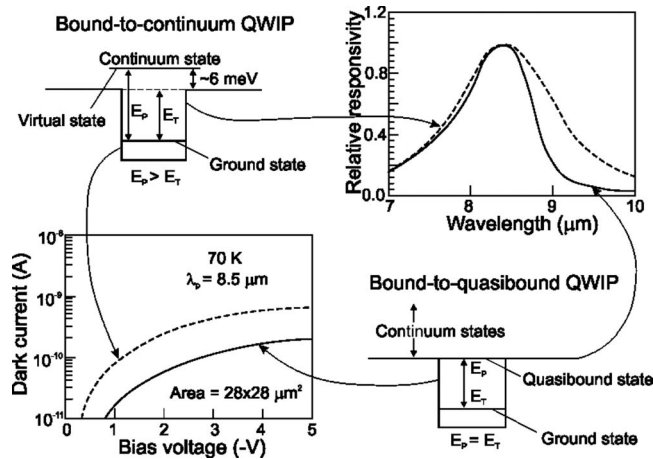


FIG. 21. In typical photoresponse curves of bound-to-quasibound and bound-to-continuum  $8.5 \times 10^{-4}$  m QWIPs at a temperature of 77 K the dark current (lower left) decreases significantly when the first excited state is dropped from the continuum to the well top, bound-to-quasibound QWIP, without sacrificing the responsivity (upper right). The first excited state now resonating with barrier top produces sharper absorption and photoresponse (after Ref. 84).

operation at  $\lambda = 7\text{--}11 \mu\text{m}$ , typically  $L_w = 40 \text{ \AA}$ ,  $L_b = 500 \text{ \AA}$ ,  $x = 0.25\text{--}0.30$ , and 50 periods are grown. In order to shift the intersubband absorption to longer wavelength the  $x$  value is decreased to  $x = 0.15$  and, in addition, in order to maintain the strong optical absorption and reasonably sharp-cutoff line shape, the quantum-well width is increased from 50 to 60  $\text{\AA}$ . This optimization allows the same bound state to excited continuum state optical absorption and efficient hot-electron transport and collection. It appears that the dark current decreases significantly when the first excited state is decreased in energy from the continuum to the well top in a bound-to-quasibound QWIP (Fig. 21), without sacrificing responsivity. The active structures are sandwiched between about  $1\text{-}\mu\text{m}$ -thick heavily doped (also  $N_d \approx 10^{18} \text{ cm}^{-3}$ ) GaAs contact layers. The photoconductive detectors are then fabricated by etching mesas through the SL, followed by Ohmic contacts made to the  $n^+$ -doped GaAs contact layers.

A miniband transport QWIP contains two bound states, the higher-energy one being in resonance with the ground state miniband in the SL barrier [see Fig. 20(b)]. In this approach, IR radiation is absorbed in the doped QWs, exciting an electron into the miniband which provides the transport mechanism, until it is collected or recaptured into another QW. Thus, the operation of this miniband QWIP is analogous to that of a weakly coupled multiquantum well (MQW) bound-to-continuum QWIP. In this device structure, the continuum states above the barriers are replaced by the miniband of the SL barriers. The miniband QWIPs have lower photoconductive gain than bound-to-continuum QWIPs because the photoexcited electron transport occurs in the miniband where electrons have to pass through many thin heterobarriers, resulting in a lower mobility.

A key factor affecting QWIP FPA performance is the light-coupling scheme. Different light-coupling mechanisms used in QWIPs are shown in Fig. 22. A distinct feature of  $n$ -type QWIPs is that the optical absorption strength is proportional to an incident photon's electric-field polarization

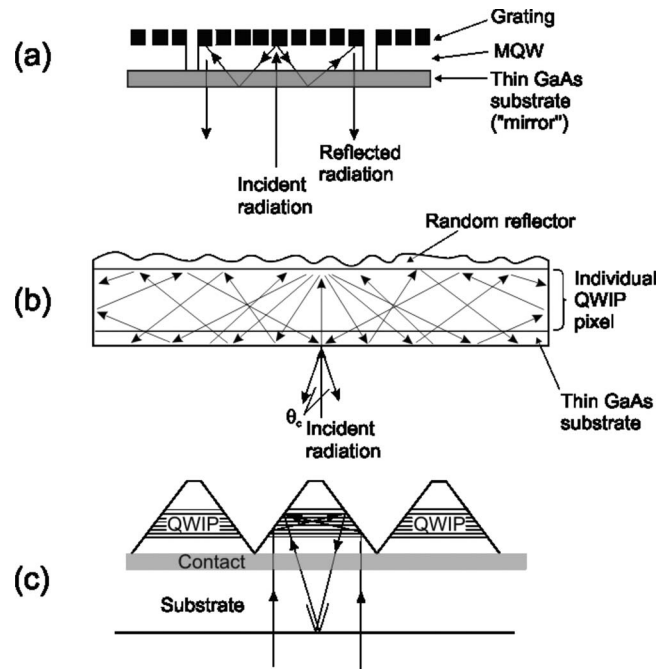


FIG. 22. Grating light-coupling mechanisms used in QWIPs: (a) gratings with optical cavity, (b) random scatterer reflector, and (c) corrugated QWs.

component normal to the QWs. This implies that a photon propagating normal to the QWs, whose polarization is entirely in the plane of the QWs, will not be absorbed. Therefore, these detectors have to be illuminated through a  $45^\circ$  polished facet. For imaging, it is necessary to be able to couple light uniformly to 2D arrays of these detectors, so a diffraction grating or other similar structure is typically fabricated on one side of the detectors to redirect a normally incident photon into propagation angles more favorable for absorption. The pixels of 2D arrays are thinned to about  $5 \mu\text{m}$  in thickness, which traps diffracted light inside the illuminated pixels, thus increasing responsivity and eliminating cross-talk. The thinning also renders the detector array more flexible, allowing it to accommodate the thermal expansion mismatch with the indium bump-bonded Si ROIC.

Light-coupling structures, such as diffraction gratings and random gratings, achieve high quantum efficiency only when the detector size is large. In addition, because of its wavelength dependence, each grating design is only suitable for a specific wavelength. Further work is needed to develop a size and wavelength independent coupling scheme. In order to simplify array production, a corrugated QWIP has been proposed.<sup>85,86</sup> The device structure is shown in Fig. 22(c). This structure utilizes total internal reflection at the sidewalls of triangular trenches which define the pixel as well as create favorable optical polarization for IR absorption. These trenches are created by chemically etching an array of V grooves through the detector active region along a specific crystallographic direction.

LWIR QWIPs cannot compete with HgCdTe photodiodes as single devices, especially for higher temperature operation ( $>70 \text{ K}$ ) due to fundamental limitations associated with intersubband transitions. In addition, QWIP detectors have relatively low quantum efficiencies, typically less

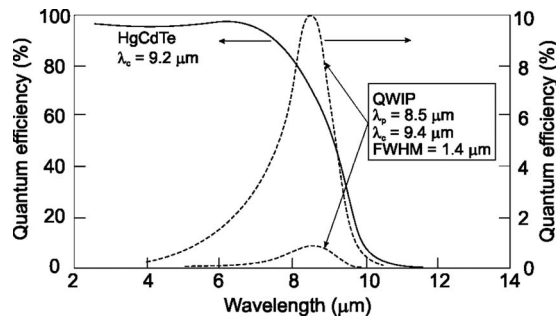


FIG. 23. Quantum efficiency vs wavelength for a HgCdTe photodiode and GaAs/AlGaAs QWIP detector with similar cutoffs.

than 10%. Figure 23 compares the spectral  $\eta$  of a HgCdTe photodiode to that of a QWIP. A higher bias voltage can be used to boost  $\eta$  in the QWIP. However, an increase in the reverse bias voltage also causes an increase in the leakage current and associated noise, which limits any potential improvement in system performance. HgCdTe has high optical absorption and a wide absorption band irrespective of the polarization of the radiation, which greatly simplifies the detector array design. The quantum efficiency of HgCdTe photodiodes is routinely around 70% without an antireflection (AR) coating and is in excess of 90% with an AR coating. Moreover, it is independent of the wavelength over the range from less than 1  $\mu\text{m}$  to near the cutoff of the detector. The wide-band spectral sensitivity with a near-perfect  $\eta$  enables greater system collection efficiency and allows a smaller aperture to be used. This makes HgCdTe FPAs useful for imaging, spectral radiometry, and long-range target acquisition. It should be noted, however, that because of high photon fluxes, current LWIR staring array performance is mostly limited by the charge handling capacity of the ROIC and the background (warm optics). Thus, the spectral response band of QWIP detectors, with a full width at half maximum of about 15%, is not a major drawback at LWIR wavelengths.

The magnitude of QWIP dark current can be modified using different device structures, doping densities, and bias conditions. Figure 24 shows the QWIP  $I$ - $V$  characteristics for temperatures ranging from 35 to 77 K, measured in a device at the 9.6  $\mu\text{m}$  spectral peak. It shows typical operation at 2 V applied bias in the region where the current varies slowly

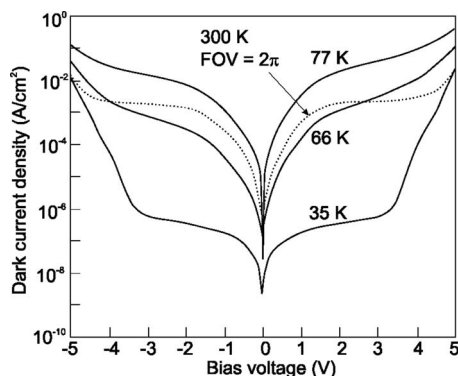


FIG. 24. Current-voltage characteristics of a QWIP detector having a peak response of 9.6  $\mu\text{m}$  at various temperatures, along with the 300 K background window current measured at 30 K with an 180° FOV (after Ref. 87).

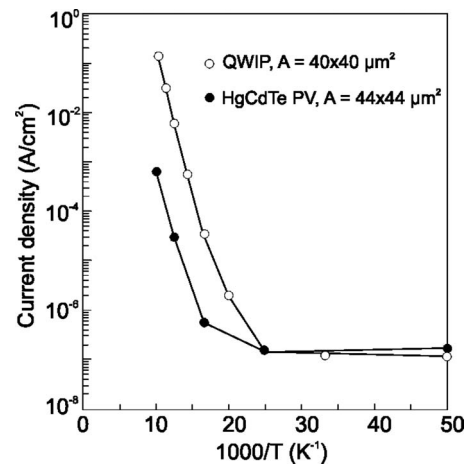


FIG. 25. Current density vs temperature for a HgCdTe photodiode and a GaAs/AlGaAs QWIP with  $\lambda_c = 10 \mu\text{m}$  (after Ref. 88).

with bias, between the initial rise in current at low voltage and the later rise at high bias. Typical LWIR QWIP dark current is about  $10^{-4} \text{ A/cm}^2$  at 77 K. Thus, a 9.6  $\mu\text{m}$  QWIP must be cooled to 60 K to have a leakage current comparable to that of a 12  $\mu\text{m}$  HgCdTe photodiode operating at a temperature that is 25 °C higher. Additional insight into the difference in the temperature dependence of the dark currents is given by Fig. 25, where the current density versus inverse temperature for a GaAs/AlGaAs QWIP and a HgCdTe photodiode, both with  $\lambda_c = 10 \mu\text{m}$ , is shown. The current density of both detectors at temperatures lower than 40 K is similar and is limited by tunneling which is temperature independent. The thermionic emission regime for the QWIP ( $\geq 40 \text{ K}$ ) is highly temperature dependent, and “cuts on” very rapidly. At 77 K, the QWIP has a dark current which is approximately two orders of magnitude higher than that of the HgCdTe photodiode.

All the QWIP detectivity data for devices with cutoff wavelength near 9  $\mu\text{m}$  are clustered between  $10^{10}$  and  $10^{11} \text{ cm Hz}^{1/2}/\text{W}$  at an operating temperature close to 77 K. However, the advantage of HgCdTe is less distinct in temperature range below 50 K due to the problems associated with HgCdTe material ( $p$ -type doping, Shockley–Read–Hall recombination, trap-assisted tunneling, surface and interface instabilities). A more detailed comparison of the two technologies has been given by Tidrow *et al.*<sup>2</sup> and Rogalski.<sup>40,45,49</sup> Table V compares the essential properties of three types of LWIR devices at 77 K.

Even though QWIPs are photoconductive devices, several of its properties such as high impedance, fast response time, and low power consumption are well matched with the requirements for large FPA fabrication. The main drawbacks of LWIR QWIP FPA technology are the performance limitations for applications requiring short integration time and the requirement to operate at a lower temperature than HgCdTe of comparable cutoff wavelength. The main advantages of QWIPs are linked to pixel performance uniformity and to the availability of large size arrays. The large established industrial infrastructure in III-V materials/device growth, processing, and packaging brought about by the application of GaAs-based devices in the telecommunications industry



TABLE V. Essential properties of LWIR HgCdTe and type-II SL photodiodes and QWIPs at 77 K.

Parameter	HgCdTe	QWIP ( <i>n</i> -type)	InAs/GaInSb SL
IR absorption	Normal incidence	$E_{\text{optical}} \perp$ plane of well required Normal incidence: no absorption	Normal incidence
Quantum efficiency	$\geq 70\%$	$\leq 10\%$	$\approx 30\% - 40\%$
Spectral sensitivity	Wide-band	Narrow band (FWHM $\approx 1 - 2 \mu\text{m}$ )	Wide band
Optical gain	1	0.2 (30–50 wells)	1
Thermal generation lifetime	$\approx 1 \mu\text{s}$	$\approx 10 \text{ ps}$	$\approx 0.1 \mu\text{s}$
$R_0A$ product ( $\lambda_c = 10 \mu\text{m}$ )	$300 \Omega \text{ cm}^2$	$10^4 \Omega \text{ cm}^2$	$100 \Omega \text{ cm}^2$
Detectivity			
( $\lambda_c = 10 \mu\text{m}$ , FOV = 0)	$2 \times 10^{12} \text{ cm Hz}^{1/2} \text{ W}^{-1}$	$2 \times 10^{10} \text{ cm Hz}^{1/2} \text{ W}^{-1}$	$5 \times 10^{11} \text{ cm Hz}^{1/2} \text{ W}^{-1}$

gives QWIPs a potential advantage in producibility and cost, whereas the only major use of HgCdTe, to date, is for IR detectors.

State-of-the-art QWIP and HgCdTe FPAs provide similar performance figures of merit because they are predominantly limited by the readout circuits. It can be shown that NEDT values for charge-limited HgCdTe photodiodes can be determined by the equation<sup>89</sup>

$$\text{NEDT} = \frac{2kT_B^2 \bar{\lambda}}{hc \sqrt{2N_w}}, \quad (11)$$

where  $\bar{\lambda} = (\lambda_1 + \lambda_2)/2$  is the average wavelength of the spectral band between  $\lambda_1$  and  $\lambda_2$ . If one assumes a typical storage capacity of  $2 \times 10^7$  electrons,  $\bar{\lambda} = 10 \mu\text{m}$ , and  $T_B = 300 \text{ K}$ , Eq. (11) yields NEDT of 19.8 mK.

Under the same conditions, the NEDT for QWIPs is given by<sup>89</sup>

$$\text{NEDT} = \frac{2kT_B^2 \bar{\lambda}}{hc} \sqrt{\frac{g}{N_w}}, \quad (12)$$

where  $g$  is the photoconductive gain.

Comparing Eqs. (11) and (12) it is evident that the value of NEDT in charge-limited QWIP detectors is better than that of HgCdTe photodiodes by a factor of  $(2g)^{1/2}$ , since a reasonable value of  $g$  is 0.4. Assuming the same operating conditions as for the above HgCdTe photodiode, the value of NEDT is 17.7 mK. Thus, a low photoconductive gain actually increases the  $S/N$  ratio, and a QWIP FPA can have a better NEDT than a HgCdTe FPA with a similar charge-storage capacity.

The above result was confirmed experimentally by researchers at Fraunhofer IAF for a photovoltaic QWIP structure.<sup>90,91</sup> The photoconduction mechanism of the photovoltaic “low-noise” QWIP structure is indicated in the inset of Fig. 26(b), where four zones (1)–(4) of each period are shown. Because of the periodic layout, the detector structure has been called a four-zone QWIP.<sup>65</sup> The first two zones (1 and 2) are analogous to the barrier and well of a conventional QWIP [see Fig. 20(a)]. Two additional zones are present in order to control the relaxation of the photoexcited carriers, namely a capture zone (3) and a tunneling zone (4). The tunneling zone has two functions; it blocks the carriers in the quasicontinuum (carriers can be captured more efficiently into a capture zone) and transmits the carriers from the

ground state of the capture zone into the excitation zone of the subsequent period. In this way, the noise associated with carrier capture is suppressed.

Figure 26 summarizes the performance of a typical 20-period low-noise QWIP with a cutoff wavelength of  $9.2 \mu\text{m}$ . The peak responsivity is 11 mA at zero bias (photovoltaic operation) and about 22 mA/W in the range between  $-2$  and  $-3 \text{ V}$ . Between  $-1$  and  $-2 \text{ V}$ , a gain of about 0.05 is observed. The detectivity has its maximum at a bias of approximately  $-0.8 \text{ V}$ , and about 70% of this value is obtained at zero bias. Due to the asymmetric nature of the transport process, the detectivity strongly depends on the sign of the bias voltage. This behavior is in strong contrast with a conventional QWIP where the detectivity vanishes at zero bias.

Based on the photovoltaic low-noise four-zone QWIP structure, the Fraunhofer group<sup>90,91</sup> has manufactured a  $256 \times 256$  FPA camera operating at 77 K with a  $9 \mu\text{m}$  cutoff wavelength. The camera exhibits record-low NEDT values of 7.4 mK with 20 ms integration time and 5.2 mK with 40 ms. It is the best temperature resolution ever obtained in the LWIR regime.

The very short integration time of LWIR HgCdTe devices (typically below  $300 \mu\text{s}$ ) is very useful to freeze a

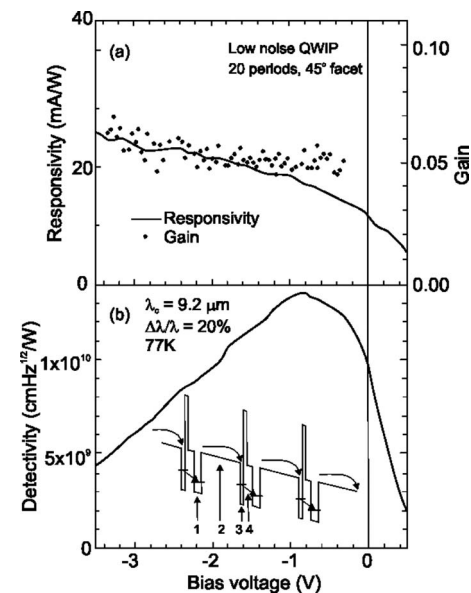


FIG. 26. Peak responsivity, gain (a), and peak detectivity (b) of a low-noise QWIP vs bias voltage (after Ref. 91).

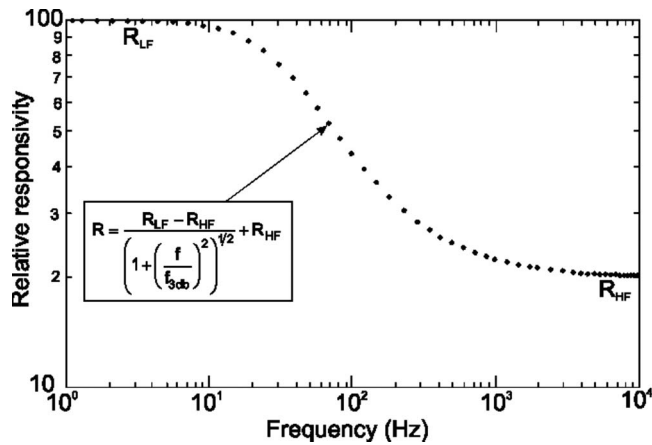


FIG. 27. Generalized frequency response of QWIP detector (after Ref. 94).

scene with rapidly moving objects. Due to excellent uniformity and low photoelectrical gain QWIP devices achieve a better NEDT than HgCdTe, however, the integration time must be 10 to 100 times longer, typically 5–20 ms in order to achieve that figure. Decisions regarding which technology is superior are consequently driven by the specific needs of the system and application. Even though HgCdTe photodiodes intrinsically exhibit higher performance than QWIP detectors, the latter are used for large formats (e.g.,  $1024 \times 1024$  and larger) with low frame rates and long integration times. Recently, 1 magapixel hybrid MWIR and LWIR QWIP with  $18 \mu\text{m}$  pixel size has been demonstrated with excellent imaging performance.<sup>92,93</sup> The MWIR detector arrays have demonstrated a NEDT of 17 mK at 95K operating temperature with  $f/2.5$  optics and a 300 K background, and the LWIR detector array has demonstrated a NEDT of 13 mK at 70 K operating temperature with the same optical and background conditions as the MWIR detector array.<sup>92</sup> This technology can be readily extended to a  $2K \times 2K$  array, but at present the limitation is the readout availability and cost.

At the present stage of technology development, QWIP devices are not suitable for space based remote-sensing applications due to dielectric relaxation effects and flux memory effects. In low irradiance environments and associated low-temperature operation, the responsivity of QWIPs depends on frequency and the frequency response depends on the operating conditions (temperature, photon irradiance, bias voltage, and the dynamic resistance of the detector). The typical frequency response is empirically similar to dielectric relaxation effects observed in bulk extrinsic silicon and germanium photoconductors under similar operational conditions. The frequency response has flat regions at both low and at high frequencies and the response rolls off between these two levels at a frequency point that is proportional to the inverse of the dynamic resistance of the detector<sup>94</sup> (see Fig. 27). The dynamic resistance is set by a combination of detector bias, photon irradiance, and operating temperature. Under typical ambient background conditions, the dynamic resistance is low and the roll-off, which takes place at frequencies in the range of 100 kHz, is not normally evident.

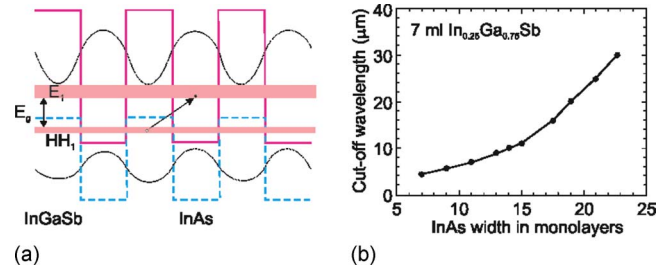


FIG. 28. (Color online) InAs/GaInSb SLS: (a) band edge diagram illustrating the confined electron and hole minibands which form the energy band gap; (b) change in cutoff wavelength with change in one SL parameter—InAs layer width (after Ref. 96).

### C. InAs/GaInSb type-II SLS photodiodes

InAs/Ga<sub>1-x</sub>In<sub>x</sub>Sb (InAs/GaInSb) SLSs can be considered as an alternative candidate to the HgCdTe and GaAs/AlGaAs IR material systems for third-generation IR detectors. The low quantum efficiency of QWIPs is largely due to the fact that the optical transition is forbidden for light of normal incidence. Straylight generated by reflecting gratings is required to achieve reasonable quantum efficiency. In the case of InAs/GaInSb SLS structures, optical absorption is strong for normal incidence of light. Consequently, SLS structures provide high responsivity, similar to that already achieved with HgCdTe, without any need for gratings. Further advantages are a photovoltaic mode of operation, operation at elevated temperatures, and well established III-V process technology.

The InAs/GaInSb material system is, however, in a very early stage of development. Problems still exist with material growth, processing, substrate preparation, and device passivation.<sup>95</sup> Optimization of SL growth is a trade-off between interface roughness, with smoother interfaces obtained at higher temperature, and residual background carrier concentration, which is minimized at the low-temperature end of the growth window. The thin nature of InAs and GaInSb layers ( $<8 \text{ nm}$ ) necessitates low growth rates for control of each layer thickness to within 1 (or  $\frac{1}{2}$ ) monolayer (ML). Monolayer fluctuations of the InAs layer thickness can shift the cutoff wavelength by about  $\pm 2 \mu\text{m}$  for a  $20 \mu\text{m}$  designed cutoff. Typical growth rates are less than 1 ML/s for each layer.

#### 1. Material properties

Type-II SLs have a staggered band alignment such that the conduction band of the InAs layer is lower than the valence band of the InGaSb layer, as shown in Fig. 28. This creates a situation in which the energy band gap of the SL can be adjusted to form either a semimetal (for wide InAs and GaInSb layers) or a narrow band gap (for narrow layers) semiconductor material. In the SL, the electrons are mainly located in the InAs layers, whereas holes are confined to the GaInSb layers. This suppresses Auger recombination mechanisms and thereby enhances carrier lifetime. Optical transitions occur spatially indirectly and, thus, the optical matrix element for such transitions is relatively small. The band gap of the SL is determined by the energy difference between the electron miniband  $E_L$  and the first heavy hole state  $HH_L$  at

the Brillouin zone center and can be varied continuously in a range between 0 and about 250 meV. An example of the wide tunability of the SL is shown in Fig. 28(b).

It has been suggested that the InAs/Ga<sub>1-x</sub>In<sub>x</sub>Sb SLS material system can have some advantages over bulk HgCdTe, including lower leakage currents and greater uniformity.<sup>97,98</sup> Electronic properties of SLSs may be superior to those of the HgCdTe alloy.<sup>98</sup> The effective masses are not directly dependent on the band gap energy, as is the case in a bulk semiconductor. The electron effective mass in an InAs/GaInSb SLS is larger ( $m^*/m_0 \approx 0.02-0.03$ , compared to  $m^*/m_0 = 0.009$  in HgCdTe alloy with the same band gap  $E_g \approx 0.1$  eV), thus, diode tunneling currents in the SL can be reduced in comparison to the HgCdTe alloy.<sup>99</sup> Although in-plane mobilities drop precipitously for thin wells, electron mobilities approaching  $10^4$  cm<sup>2</sup>/V s have been observed in InAs/GaInSb SLs with layers less than 40 Å thick. While mobilities in these SLs are found to be limited by the same interface roughness scattering mechanism, detailed band structure calculations reveal a much weaker dependence on layer thickness, in reasonable agreement with experiment.<sup>100</sup>

A consequence of the type-II band alignment of the InAs/GaInSb material system is spatial separation of electrons and holes. This is particularly disadvantageous for optical absorption, where a significant overlap of electron and hole wave functions is needed. However, a reduction in the electronic confinement can be achieved by growing thinner GaInSb barriers or by introducing more indium into the GaInSb layers leading to an optical absorption coefficient comparable to that of HgCdTe.

Theoretical analysis of band-to-band Auger and radiative recombination lifetimes for InAs/GaInSb SLSs indicate that the *p*-type Auger recombination rates are suppressed by several orders of magnitude, compared to those of bulk HgCdTe with similar band gap.<sup>101,102</sup> Predictions for *n*-type materials are less advantageous. However, the promise of Auger suppression has not been observed in practical device material due to the dominance of Shockley–Read–Hall recombination.<sup>103</sup> The longer lifetime values from recently published experimental data<sup>104</sup> coincide well with the HgCdTe trend line in the range of low carrier concentration.<sup>47</sup> In general, however, the SL carrier lifetime is limited by the influence of trap centers located at an energy level of  $\sim 1/3$  band gap below the effective conduction band edge.

Narrow band gap materials require the doping to be controlled to at least  $1 \times 10^{15}$  cm<sup>-3</sup> or below to avoid deleterious high-field tunneling currents across the very narrow depletion widths at temperature below 77 K. Lifetimes must be increased to enhance carrier diffusion and reduce related dark currents. At the present stage of development, the residual doping concentration (both *n*-type as well as *p*-type) is typically about  $5 \times 10^{15}$  cm<sup>-3</sup> in SLs grown at substrate temperatures ranging from 360 to 440 °C.<sup>95</sup> Low to mid- $10^{15}$  cm<sup>-3</sup> residual carrier concentrations are the best that have been achieved so far.

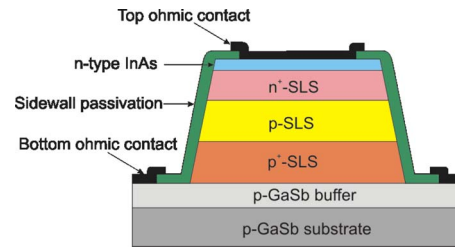


FIG. 29. (Color online) Cross section schematic of *p-i-n* InAs/GaInSb SL photodiode.

## 2. SL photodiodes

InAs/GaInSb SL photovoltaic detectors are predicted to have very high performance based on the theoretical promise of longer intrinsic lifetimes due to the suppression of Auger recombination mechanism. Considering the *n-on-p* and the *p-on-n* structures, the *n-on-p* geometry (*n*-type cap contact layer on a *p*-type absorber) has been theoretically shown to be advantageous, a result based on favorable Auger lifetimes and superior minority carrier transport properties associated with lightly doped *p*-type SLS.

SL photodiodes are based on *p-i-n* structures with an unintentionally doped, intrinsic region between the heavily doped contact portions of the device. A cross sectional view of a completely processed mesa detector is presented in Fig. 29. The layers are usually grown by MBE at substrate temperatures around 400 °C on undoped (001) oriented 2 in. GaSb substrates. Despite the relatively low absorption coefficients, GaSb substrates require thinning to less than 25 μm in order to transmit appreciable IR radiation.<sup>105</sup> Since the GaSb substrates and buffer layers are intrinsically *p*-type, the *p*-type contact layer, intentionally doped with beryllium at an acceptor concentration of  $1 \times 10^{18}$  at./cm<sup>3</sup>, is grown first (see Fig. 29).

Sensors for the MWIR and LWIR spectral ranges are based on binary InAs/GaSb short-period SLs.<sup>106,107</sup> The layers needed are already so thin that there is no benefit to using GaInSb alloys. For the formation of *p-i-n* photodiodes the lower periods of the SL are *p*-doped with  $1 \times 10^{17}$  cm<sup>-3</sup> Be in the GaSb layers. These acceptor doped SL layers are followed by a 1–2 μm thick, nominally undoped, SL region. The width of the intrinsic region does vary with each particular design. The width should be correlated with the carrier diffusion lengths for improved performance. The upper stack of the SL is doped with silicon ( $1 \times 10^{17}$  to  $1 \times 10^{18}$  cm<sup>-3</sup>) in the InAs layers and is typically 0.5 μm thick. The top of the SL stack is then capped with an InAs:Si ( $n \approx 10^{18}$  cm<sup>-3</sup>) layer to provide good Ohmic contact. For a cutoff in the 8–12 μm wavelength range, the InAs/GaInSb short-period SL *p-i-n* photodiodes are fabricated, with the indium molar fraction in the ternary GaInSb layers close to 20%.

The main technological challenge for the fabrication of small area photodiodes is the occurrence of surface leakage currents mainly due to tunneling electrons. Besides efficient suppression of surface leakage currents, a passivation layer suitable for production purposes must be able to withstand various treatments occurring during subsequent processing



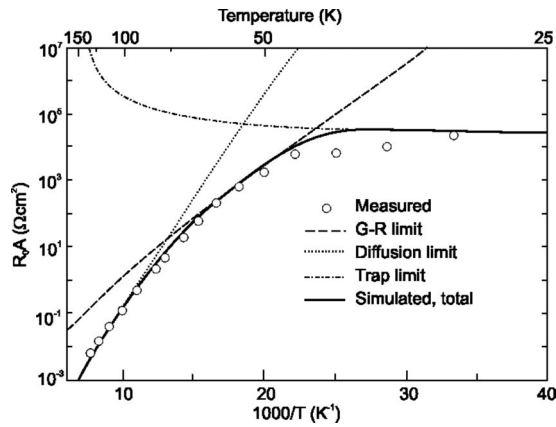
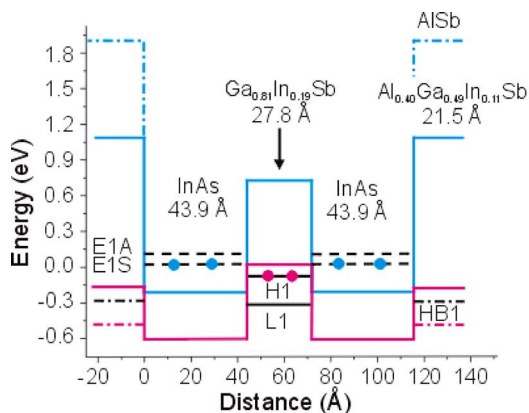


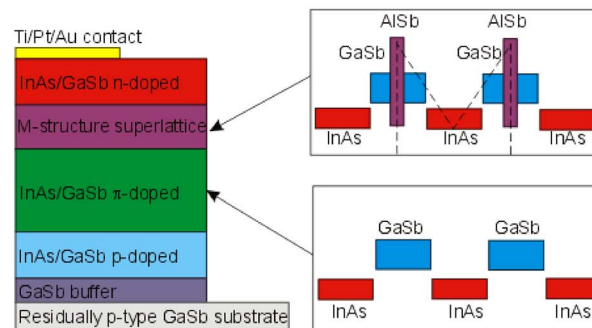
FIG. 30. Experimental data and theoretical prediction of the  $R_0A$  product as a function of temperature for InAs/GaInSb photodiode with 11  $\mu\text{m}$  cutoff wavelength. The activated trap density is taken as a constant ( $1 \times 10^{12} \text{ cm}^{-3}$ ) in the simulation over the whole temperature range (after Ref. 104).

of the device. Several materials and processes have been explored. Some of the more prominent thin film passivation layers studied have been silicon nitride, silicon oxide, ammonium sulfide, and, most recently, aluminum gallium antimonide alloys.<sup>106</sup> At present, it appears that the reproductivity and long-term stability achieved by a dielectric passivation layer are not adequate for photodiodes in the LWIR range. The mesa sidewalls are a source of excess currents. Rehm *et al.*<sup>108</sup> demonstrated good results achieved with lattice matched AlGaAsSb overgrowth by MBE on etched mesas. It is expected that the exposed sidewalls passivated with wider band gap material will generate less excess currents.

The performance of LWIR photodiodes in the high temperature range is limited by diffusion processes. For example, Fig. 30 shows the experimental data and theoretical prediction of the  $R_0A$  product as a function of temperature for an InAs/GaInSb photodiode with 11  $\mu\text{m}$  cutoff wavelength. The photodiodes are depletion region (generation-recombination) limited in the temperature range between 80 and 50 K. Trap-assisted tunneling is dominant only at low temperature ( $<50$  K) with almost constant activation trap density ( $1 \times 10^{12} \text{ cm}^{-3}$ ).



(a)



(b)

FIG. 31. (Color online) Schematic of modified type-II LWIR photodiodes: (a) band profiles at  $k=0$  of enhanced WSL (after Ref. 107), (b)  $p-\pi$ -M-n SL (band alignment of standard and M shape SLs are shown) (after Ref. 110).

Optimization of the SL photodiode architecture is still an ongoing area of research. Since some of the device design parameters depend on material properties, such as carrier lifetime and diffusion length, these properties are still being improved. Also, additional design modification can dramatically improve photodiode performance. For example, recently Aifer *et al.*<sup>109</sup> reported W-structured type-II SL (WSL) LWIR photodiodes with  $R_0A$  values comparable to state-of-the-art HgCdTe. These structures, initially developed to increase the gain in MWIR lasers, are now showing promise as LWIR and VLWIR photodiode materials. In this design, illustrated in Fig. 31(a), the AlSb barriers are replaced with shallower  $\text{Al}_{0.40}\text{Ga}_{0.49}\text{In}_{0.11}\text{Sb}$  quaternary barrier layers (QBLs) that have a much smaller conduction band offset with respect to InAs, resulting in higher electron mobility, with a miniband width of about 35 meV, compared to 20 meV for AlSb barrier layers. The QBL also uses 60% less Al, which improves material quality, since the optimal QBL growth temperature is much closer to 430  $^{\circ}\text{C}$  for the InAs and InGaSb layers, in comparison to AlSb at  $\sim 500$   $^{\circ}\text{C}$ . In such a structure, two InAs “electron wells” are located on either side of an InGaSb “hole well” and are bound on either side by AlGaInSb “barrier” layers. The barriers confine the electron wave functions symmetrically about the hole well, increasing the electron-hole overlap while nearly localizing the wave functions. The resulting quasidimensional densities of states give the WSL its characteristically strong absorption near the band edge. However, care is taken to not fully localize the wave functions, since an electron miniband is required to allow vertical transport of the photoexcited minority carriers.

The new W-structured type-II SL photodiode design employs a graded band-gap  $p-i-n$  design. The grading of the band gap in the depletion region suppresses tunneling and generation-recombination currents in the depletion region and have resulted in an order of magnitude improvement in dark current performance, with  $R_0A=216 \text{ } \Omega \text{ cm}^2$  at 78 K for devices with a 10.5  $\mu\text{m}$  cutoff wavelength. The sidewall resistivity of  $\approx 70 \text{ k}\Omega \text{ cm}$  for untreated mesas is considerably

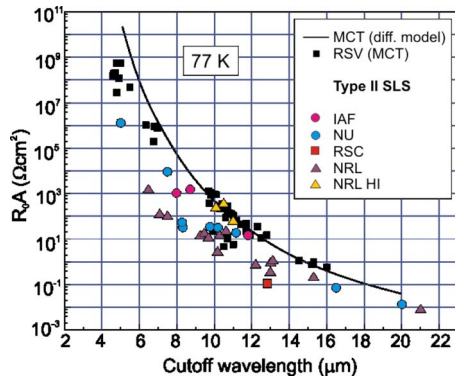


FIG. 32. (Color online) Dependence of the  $R_0A$  product of InAs/GaInSb SLS photodiodes on cutoff wavelength compared to theoretical and experimental trendlines for comparable HgCdTe photodiodes at 77 K (after Ref. 111).

higher than previously reported for type-II LWIR photodiodes, apparently indicating self-passivation by the graded band gap.<sup>109</sup>

Another type-II SL photodiode design with an M-structure barrier is shown in Fig. 31(b). This structure significantly reduces the dark current and, on the other hand, does not have a strong impact on the optical properties of the devices.<sup>110</sup> The AlSb layer in one period of the M structure, having a wider energy gap, blocks the interaction between electrons in two adjacent InAs wells, thus reducing the tunneling probability and increasing the electron effective mass. The AlSb layer also acts as a barrier for holes in the valence band and converts the GaSb hole-QW into a double QW. As a result, the effective well width is reduced, and the hole energy level becomes sensitive to the well dimension. Devices with a cutoff wavelength of 10.5  $\mu\text{m}$  exhibit a  $R_0A$  product of 200  $\Omega\text{cm}^2$  when a 500 nm thick M structure was used.

Figure 32 compares the  $R_0A$  values of InAs/GaInSb SL and HgCdTe photodiodes in the long-wavelength spectral range. The solid line denotes the theoretical diffusion limited performance of  $p$ -type HgCdTe material. As evident from the figure, the most recent photodiode results for SL devices ri-

val that of practical HgCdTe devices, indicating that substantial improvement has been achieved in SL detector development.

Figure 33 compares the calculated detectivity of type-II SLS and  $P$ -on- $n$  HgCdTe photodiodes as a function of wavelength and temperature of operation, with the experimental data of type-II detectors operated at 78 K. The solid lines are theoretical thermal limited detectivities for HgCdTe photodiodes, calculated using a 1D model that assumes that the diffusion current from the narrower band gap  $n$ -side is dominant, and minority carrier recombination is determined via Auger and radiative processes. In calculations the typical values for the  $n$ -side donor concentration ( $N_d = 1 \times 10^{15} \text{ cm}^{-3}$ ), the narrow bandgap active layer thickness (10  $\mu\text{m}$ ), and quantum efficiency (60%) have been used. It is noted that the predicted thermally limited detectivities of type-II SLSs are larger than those for HgCdTe.<sup>102,112</sup>

From Fig. 33 it can be seen that the measured thermally limited detectivities of type-II SLS photodiodes are still inferior to current HgCdTe photodiodes, since their performance has not yet achieved theoretical values. This limitation appears to be due to two main factors: relatively high background doping concentrations (about  $5 \times 10^{15} \text{ cm}^{-3}$ , although values below  $10^{15} \text{ cm}^{-3}$  have been reported<sup>70,113</sup>) and a short minority carrier lifetime (typically tens of nanoseconds in lightly doped  $p$ -type material). Up until now nonoptimized carrier lifetimes have been observed which at the desired low carrier concentrations are limited by Shockley–Read–Hall recombination mechanisms. The minority carrier diffusion length is in the range of several micrometers. Improving these fundamental parameters is essential in order to realize the predicted performance of type-II photodiodes.

The theory and technology of type-II InAs/GaInSb based detectors have made rapid progress over the past few years. The presented results indicate that fundamental material properties of InAs/GaInSb SLs allow for practical realization of high-performance FPAs.

Recently, first  $256 \times 256$  SL MWIR detectors have been hybridized.<sup>42,114</sup> The cutoff wavelength of these detectors is 5.3  $\mu\text{m}$ . An excellent NEDT value of approximately 10 mK measured with  $f/2$  optics and integration time  $\tau_{\text{int}} = 5 \text{ ms}$  has been presented. Tests with reduced integration time down to 1 ms show that the NEDT scales inversely proportional to the square root of the integration time [see Eq. (6)], which indicates that even for short integration time the detectors are background limited. A very important feature of InAs/GaInSb FPAs is their high uniformity. The responsivity spread shows a standard deviation of approximately 3%. It is estimated that the pixel outages are in the order of 1%–2% and are statistically distributed as single pixels without large clusters.

## D. QDIP

The beginning of QD research can be traced back to a suggestion by Arakawa and Sakaki<sup>115</sup> in 1982 that the performance of semiconductor lasers could be improved by reducing the dimensionality of the active regions of these devices. Initial efforts at reducing the dimensionality of the

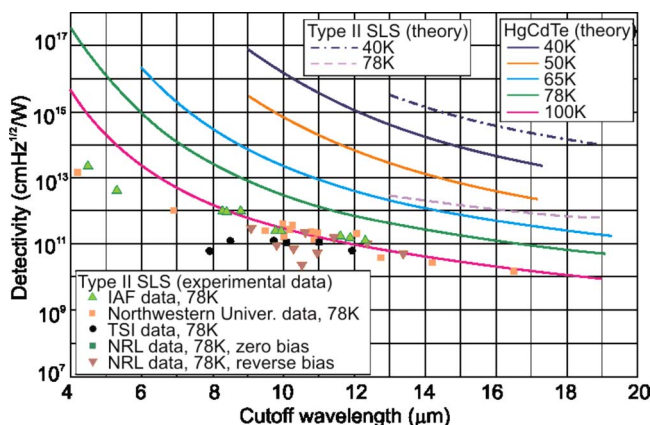


FIG. 33. (Color online) The predicted detectivity of type-II and  $P$ -on- $n$  HgCdTe photodiodes as functions of wavelength and temperature (after Ref. 70).

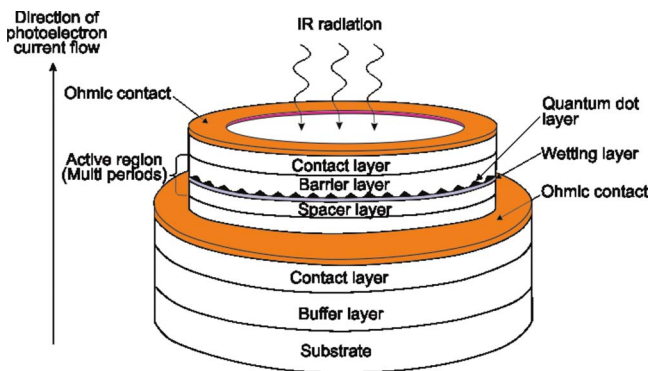


FIG. 34. (Color online) Schematic of conventional QD detector structure.

active regions focused on using ultrafine lithography coupled with wet or dry chemical etching to form three-dimensional (3D) structures. It was soon realized, however, that this approach introduced defects (high density of surface states) that greatly limited the performance of such QDs. Subsequent efforts were mainly focused on the growth of InGaAs nanometer-sized islands on GaAs substrates. In 1993, the first epitaxial growth of defect-free QD nanostructures was achieved by using MBE.<sup>116</sup> Most of the practical QD structures today are synthesized by either MBE or MOCVD.

Under certain growth conditions, when the thickness of the film, with the larger lattice constant, exceeds a certain critical thickness, the compressive strain within the film is relieved by the formation of coherent islands. These islands may be regarded as QDs. Coherent QD islands are generally formed only when the growth proceeds in what is known as the Stranski–Krastanow growth mode.<sup>117</sup> The onset of transformation of the growth process from a 2D layer-by-layer growth mode to a 3D island growth mode results in a spotty reflection high energy electron diffraction (RHEED) pattern. This is in contrast to the conventional streaky pattern, generally observed for the layer-by-layer growth mode. The transition typically occurs after the deposition of a certain number of monolayers. For InAs on GaAs, this transition occurs after about 1.7 ML of InAs have been grown; this is the onset of islanding and, hence, QD formation.

First observations of intersublevel transitions in the far IR were reported in the early 1990s, either in InSb-based electrostatically defined QDs<sup>118</sup> or in a structured 2D electron gas.<sup>119</sup> The first QD IR photodetector (QDIP) was demonstrated in 1998.<sup>120</sup> Since then, great progress has been made in their development and performance characteristics<sup>121,122</sup> as well as in their application to thermal imaging FPAs.<sup>123</sup>

### 1. Anticipated advantages of QDIPs

The success of quantum-well structures for IR detector applications has stimulated the development of QDIPs. In general, QDIPs are similar to QWIPs but with the QWs replaced by QDs, which have size confinement in all spatial directions.

Two types of QDIP structures have been proposed: the conventional structure (vertical) and the lateral structure. In a vertical QDIP, the photocurrent is collected through the ver-

tical transport of carriers between the top and bottom contacts (see Fig. 34). The device heterostructure comprises repeated InAs QD layers buried between GaAs barriers with top and bottom contact layers at the active region boundaries. The mesa height can vary from 1 to 4  $\mu\text{m}$  depending on the device heterostructure. The QDs are directly doped (usually with silicon) in order to provide free carriers during photoexcitation, and an AlGaAs barrier can be included in the vertical device heterostructure in order to block dark current created by thermionic emission.<sup>124,125</sup>

The lateral QDIP collects photocurrent through transport of carriers through a high-mobility channel between two top contacts, operating much like a field-effect transistor. Once again, AlGaAs barriers are present, but instead of blocking the dark current, these barriers are used to both modulation dope the QDs and to provide the high-mobility channel. Lateral QDIPs have demonstrated lower dark currents and higher operating temperatures than vertical QDIPs since the major components of the dark current arise from interdot tunneling and hopping conduction.<sup>126</sup> However, these devices will be difficult to incorporate into a FPA hybrid-bump bonded to a silicon readout circuit. Because of this, more efforts are currently being directed at improving the performance of vertical QDIPs, which are more compatible with commercially available readout circuits.

The quantum-mechanical nature of QDIPs leads to several advantages over QWIPs and other types of IR detectors that are currently available. Similar to the HgCdTe, QWIP, and type-II superlattice technologies, QDIPs can also provide multiwavelength detection. However, QDs provide many additional parameters for tuning the energy spacing between energy levels, such as QD size and shape, strain, and material composition.

The potential advantages in using QDIPs over QWs are as follows.

- Intersubband absorption may be allowed at normal incidence (for *n*-type material). In QWIPs, only transitions polarized perpendicularly to the growth direction are allowed due to absorption selection rules. The selection rules in QDIPs are inherently different, and normal incidence absorption is observed.
- Thermal generation of electrons is significantly reduced due to energy quantization in all three dimensions. As a result, the electron relaxation time from excited states increases due to phonon bottleneck. Generation by LO phonons is prohibited unless the gap between the discrete energy levels exactly equals that of the phonon. This prohibition does not apply to QWs, since the levels are quantized only in the growth direction and a continuum exists in the other two directions (hence the presence of generation recombination by LO phonons with capture time of few picoseconds). Thus, it is expected that the S/N ratio in QDIPs will be significantly larger than that of QWIPs.
- Dark current of QDIPs is expected to be lower than in HgCdTe detectors and QWIPs due to 3D quantum confinement of the electron wave function.



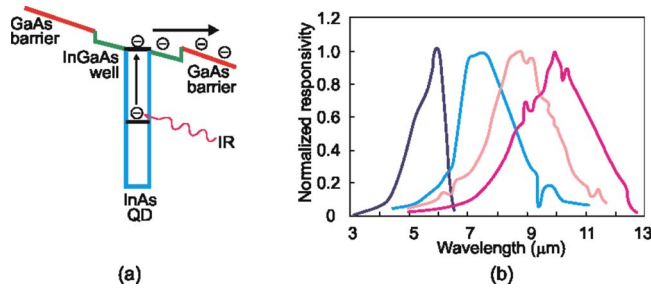


FIG. 35. (Color online) DWELL IR detector: (a) the operation mechanism, (b) experimentally measured spectral tunability by varying well width from 55 to 100 Å (after Ref. 75).

In addition to the standard InAs/GaAs QDIP, several other heterostructure designs have been investigated for use as IR photodetectors.<sup>127,128</sup> An example is InAs QDs embedded in a strain-relieving InGaAs QW which are known as dot-in-a-wall (DWELL) heterostructures (see Fig. 35).<sup>129</sup> This device offers two advantages: challenges in wavelength tuning through dot-size control can be compensated in part by engineering the quantum-well sizes, which can be controlled precisely, and, second, QWs can trap electrons and aid in carrier capture by QDs, thereby facilitating ground state refilling. Figure 35(b) shows DWELL spectral tuning by varying the well geometry.

As was indicated by Kinch,<sup>130</sup> the normalized thermal generation,

$$G_{th} = n_{th}/(\alpha\tau), \quad (13)$$

predicts the ultimate performance of any IR material and can be used to compare the relative performance of different materials as a function of temperature and energy gap (cutoff wavelength). In the above equation,  $n_{th}$  is the density of thermal carriers at temperature  $T$ ,  $\tau$  is the carrier lifetime, and  $\alpha$  is the absorption coefficient of the material.

In further considerations we will use a simple set of fundamental detector parameters described in the excellent paper by Kinch<sup>130</sup> to compare the performance of different material systems used in IR detector technology. In the case

of QDIPs, a model developed by Phillips is adopted.<sup>131</sup> The normalized thermal generation directly determines thermal detectivity,

$$D^* = \frac{\eta}{qh\nu\sqrt{2G_{th}}}. \quad (14)$$

Figure 36 compares the thermal detectivities of various photodetectors with cutoff wavelength in the MWIR ( $\lambda_c = 5 \mu\text{m}$ ) and LWIR ( $\lambda_c = 10 \mu\text{m}$ ) regions. The assumed typical quantum efficiencies are indicated in the figure. Theoretical estimates for QDIPs are carried out assuming two quantum efficiencies of  $\approx 2\%$  (often measured in practice) and 67%, which is typical for HgCdTe photodiodes (without AR coating). It should be noted, however, that rapid progress has recently been made in the performance of QDIP devices, especially for operation at near room temperature. Lim *et al.*<sup>71</sup> announced a quantum efficiency of 35% for QDIPs with peak detection wavelength around 4.1  $\mu\text{m}$ . Theoretical predictions indicate potential performance capabilities of type-II SL photodiodes and QDIPs which are expected to be competitive with HgCdTe photodiodes.

Both the increased electron lifetime and the reduced dark current indicate that QDIPs should be able to provide high temperature operation. In practice, however, it has been a challenge to meet all of the above expectations. Carrier relaxation times in QDs are longer than the typical 1–10 ps measured for QWs. It is predicted that the carrier relaxation time in QDs is limited by electron-hole scattering,<sup>132</sup> rather than phonon scattering. For QDIPs, the carrier lifetime is expected to be even longer, (1 ns) since QDIPs are majority carrier devices due to the absence of holes.

The main disadvantage of QDIPs is the large inhomogeneous linewidth of the QD ensemble variation of dot size in the Stranski–Krastanow growth mode.<sup>131,133</sup> As a result, the absorption coefficient is reduced, since it is inversely proportional to the ensemble linewidth. Large, inhomogeneously broadened linewidth has a deleterious effect on QDIP performance. Subsequently, the quantum efficiency of QD devices tends to be lower than what is predicted theoretically. Vertical coupling of QD layers reduces the inhomogeneous linewidth of the quantum-dot ensemble; however, it may also

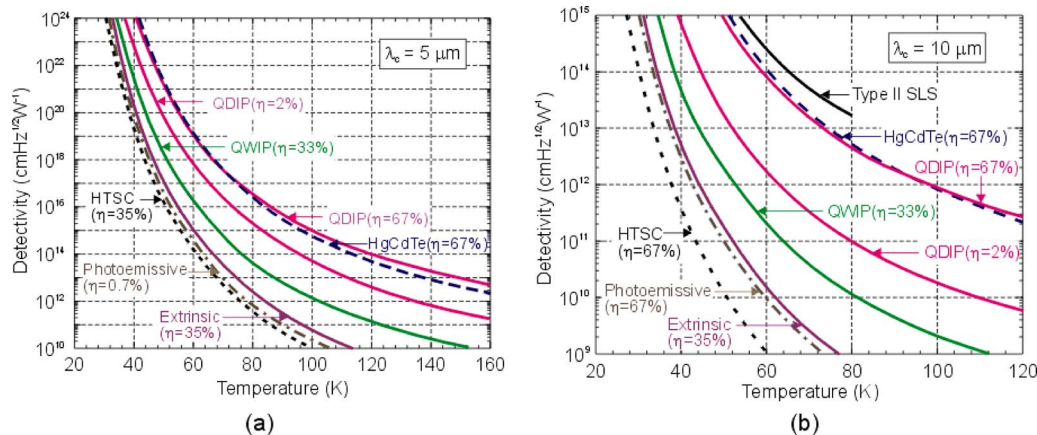


FIG. 36. (Color online) The predicted thermal detectivity vs temperature for various MWIR ( $\lambda_c = 5 \mu\text{m}$ ) (a) and LWIR ( $\lambda_c = 10 \mu\text{m}$ ) (b) photodetectors. The assumed quantum efficiencies are indicated.

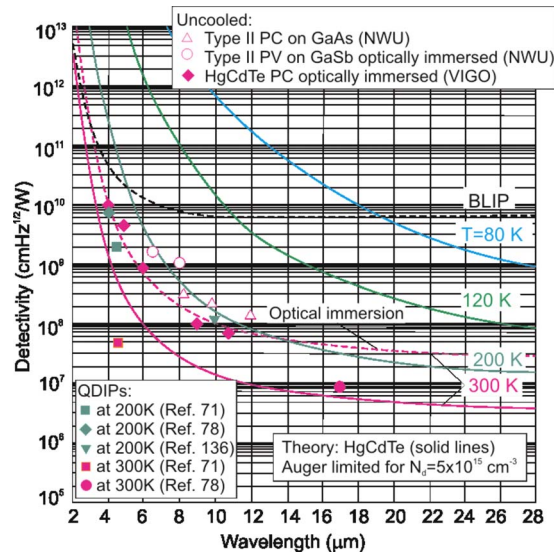


FIG. 37. (Color online) Calculated performance of Auger generation-recombination limited HgCdTe photodetectors as a function of wavelength and operating temperature. BLIP detectivity has been calculated for 2 $\pi$  FOV, the background temperature is  $T_{\text{BLIP}}=300$  K, and the quantum efficiency  $\eta=1$ . The calculations have been performed for a doping level equal to  $N_d=5 \times 10^{15} \text{ cm}^{-3}$ . The experimental data are taken for commercially available uncooled HgCdTe photoconductors (produced by Vigo System) and uncooled type-II detectors at the Center for Quantum Devices, Northwestern University. The experimental data for QDIPs are gathered from the marked literature for detectors operated at 200 and 300 K.

increase the dark current of the device, since carriers can tunnel between adjacent dot layers more easily. As in other types of detectors, a nonuniform dopant incorporation adversely affects the performance of the QDIP. Therefore, improving QD uniformity is a key issue in increasing the absorption coefficient and improving performance. Consequently, the growth and design of unique QD heterostructures are the most important issues related to achieving the theoretically predicted QDIP performance.<sup>134</sup>

## 2. Experimental verification

Figure 19 compares the highest measurable detectivities at 77 K of QDIPs found in the literature, along with the predicted detectivities of *P*-on-*n* HgCdTe photodiodes. The solid lines are theoretical thermal limited detectivities for HgCdTe photodiodes, calculated using a 1D model assuming that diffusion current from the narrower band gap *n*-side is dominant. It should be noted that for HgCdTe photodiodes, theoretically predicted curves for the temperature range between 50 and 100 K coincide very well with experimental data. The measured values of QDIP detectivities at 77 K gathered in Fig. 19 indicate that QD device detectivities are as yet considerably lower than current HgCdTe detector performance. In LWIR region, the best experimental QDIP data at 77 K coincide with that for HgCdTe at a temperature of 100 K.

One of the main potential advantages of QDIPs is low dark current, which enables higher operating temperatures. Up until now, however, most QDIP devices reported in the literature have demonstrated operation in the temperature range of 77–200 K. On account of this fact, it is interesting

to consider potentially achievable QDIP performance at temperatures above 200 K in comparison with other types of detectors.

Figure 37 compares the calculated detectivity of Auger generation-recombination limited HgCdTe photodetectors as a function of wavelength and operating temperature with the experimental data of uncooled type-II InAs/GaInSb SLS detectors and QDIPs. The Auger mechanism is likely to impose fundamental limitations on the LWIR HgCdTe detector performance. The calculations for HgCdTe photodiodes have been performed for optimal *p*-type doping levels equal to  $p = \gamma^{1/2} n_i$ . The experimental data for QDIPs are gathered from the literature for detectors operated at 200 and 300 K.

Uncooled LWIR HgCdTe photodetectors are commercially available and manufactured in significant quantities, mostly as single-element devices.<sup>135,136</sup> They have found important applications in IR systems that require fast response. The results presented in Fig. 36 confirm that type-II SL devices are a good candidate for IR detectors operating in the spectral range from the midwavelength to the very long-wavelength IR. However, comparison of QDIP performance both with HgCdTe and type-II SL detectors provides evidence that QDIPs are suitable for high temperature operation. Especially encouraging results have been achieved for very long-wavelength QDIP devices with a double-barrier resonant tunneling filter with each quantum-dot layer in the absorption region.<sup>137</sup> In this type of device photoelectrons are selectively collected from the QDs by resonant tunneling, while the same tunnel barriers block electrons of dark current due to their broad energy distribution. For a 17  $\mu\text{m}$  cutoff detector, a peak detectivity of  $8.5 \times 10^6 \text{ cm}^2 \text{ Hz}^{1/2}/\text{W}$  has been measured. Up until now, this novel device has demonstrated the highest performance of any room temperature photodetector.

IR FPAs (see Fig. 3) have individual-amplifier-per-detector readouts based on metal oxide semiconductor field effect transistors (MOSFETs). To receive high injection efficiency, the input impedance of the MOSFET must be much lower than the internal dynamic resistance of the detector at its operating point, and the following condition should be fulfilled:<sup>138</sup>

$$IR_d \gg \frac{nkT}{q}, \quad (15)$$

where  $n$  is an ideality factor that can vary with temperature and geometry of the detector and is usually in the range of 1–2. For most applications, the detector performance depends on operating the detector at a low reverse bias where the dynamic resistance is at its maximum. It is then necessary to minimize any extraneous leakage currents. The control of these leakage currents and the associated low-frequency noise is therefore of crucial interest.

The above requirement is especially critical for near-room temperature HgCdTe photodetectors operating in the LWIR region, since their resistance is very low due to a high thermal generation rate. In materials with a high electron to hole mobility ratio, such as HgCdTe, the resistance is reduced even further by ambipolar effects. Small size uncooled 10.6  $\mu\text{m}$  cutoff photodiodes ( $50 \times 50 \mu\text{m}^2$ ) exhibit less

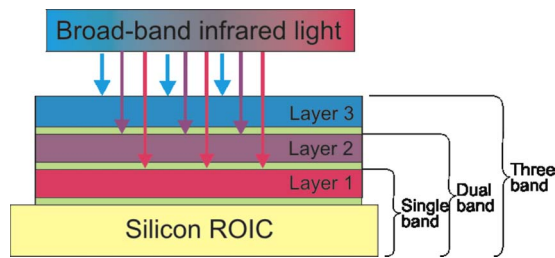


FIG. 38. (Color online) Structure of a three-color detector pixel. IR flux from the first band is absorbed in layer 3, while longer wavelength flux is transmitted through the next layers. The thin barriers separate the absorbing bands.

than  $1 \Omega$  zero bias junction resistances, which is well below the series resistance of the diode. As a result, the performance of conventional devices is very poor, which renders them unsuitable for practical applications. To fulfill the inequality in Eq. (15) and effectively couple the detector with the silicon readout, the detector incremental resistance should be  $R_d \gg 2 \Omega$ .

It is expected that further improvements in technology and design can result in the future application of QDIPs in room temperature FPAs with the added advantage of higher operating speed (shorter frame time) in comparison with thermal detectors (bolometers and pyroelectric devices).

In the past few years, several groups have independently demonstrated cryogenically cooled QD FPAs with midformat size  $256 \times 256$ ,<sup>139,140</sup>  $320 \times 256$ ,<sup>52</sup> and  $640 \times 512$ .<sup>55,75</sup> Recently, DWELL structures with peak responsivity out to  $8.1 \mu\text{m}$  and detectivity of  $\approx 10^{10} \text{ cm Hz}^{1/2}/\text{W}$  at 77 K fabricated into  $640 \times 512$  pixel FPA have produced IR imagery with NEDT of 40 mK at 60 K operating temperature.<sup>75</sup>

## VII. HgCdTe MULTICOLOR DETECTORS

The standard method to detect multiwavelength simultaneously is to use optical components such as lenses, prisms, and gratings to separate the wavelength components before they impinge on the IR detectors. Another simpler method is a stacked arrangement in which the shorter wavelength detector is placed optically ahead of the longer wavelength detector. In such a way, two-color detectors using HgCdTe (Ref. 141) and InSb/HgCdTe (Ref. 142) photoconductors have been demonstrated in the early 1970s. At present, however, considerable efforts are directed to fabricating a single FPA with multicolor capability to eliminate the spatial alignment and temporal registration problems that exist whenever separate arrays are used, to simplify optical design, and to reduce size, weight, and power consumption.

The unit cell of integrated multicolor FPAs consists of several colocated detectors, each sensitive to a different spectral band [see Fig. 38]. Radiation is incident on the shorter band detector, with the longer wave radiation passing through to the next detector. Each layer absorbs radiation up to its cutoff, and hence is transparent to the longer wavelengths, which are then collected in subsequent layers. In the case of HgCdTe, this device architecture is realized by placing a longer wavelength HgCdTe photodiode optically behind a shorter wavelength photodiode.

Back-to-back photodiode two-color detectors were first implemented using quaternary III–V alloy ( $\text{Ga}_x\text{In}_{1-x}\text{As}_y\text{P}_{1-y}$ ) absorbing layers in a lattice matched InP structure sensitive to two different SWIR bands.<sup>143</sup> A variation in the original back-to-back concept was implemented using HgCdTe at Rockwell<sup>144</sup> and Santa Barbara Research Center.<sup>145</sup> Following the successful demonstration of multispectral detectors in LPE-grown HgCdTe devices,<sup>145</sup> the MBE and MOCVD techniques have been used for the growth of a variety of multispectral detectors at Raytheon,<sup>36,146–149</sup> BAE Systems,<sup>150</sup> Leti,<sup>31,37,151–153</sup> Selex and QinetiQ,<sup>38,154,155</sup> DRS,<sup>35,61,156</sup> Teledyne and NVESD.<sup>157,158</sup> For more than a decade steady progression has been made in a wide variety of pixel sizes (to as small as  $20 \mu\text{m}$ ), array formats (up to  $1280 \times 720$ ), and spectral-band sensitivity (MWIR/MWIR, MWIR/LWIR, and LWIR/LWIR).

### A. HgCdTe dual-band detectors

The unit cell of an integrated two-color FPA consists of two colocated detectors, each sensitive to a different spectral band. In back-illuminated dual-band detectors, the photodiode with the longer cutoff wavelength is grown epitaxially on top of the photodiode with the shorter cutoff wavelength. The shorter-cutoff photodiode acts as a long-wavelength pass filter for the longer-cutoff photodiode.

Both sequential mode and simultaneous mode detectors are fabricated from multilayer materials. The simplest two-color HgCdTe detector, and the first to be demonstrated, was the bias-selectable *n*-*P*-*N* triple-layer heterojunction (TLHJ), back-to-back photodiode shown in Fig. 39(a) (capital letter means wider band gap structure). The *n*-type base absorbing regions are deliberately doped with indium at a level of about  $(1 \text{ to } 3) \times 10^{15} \text{ cm}^{-3}$ . A critical step in device formation is ensuring that the *in situ* *p*-type As-doped layer (typically  $1\text{--}2 \mu\text{m}$  thick) has good structural and electrical properties to prevent internal gain from generating spectral crosstalk. The band-gap engineering effort consists of increasing the CdTe mole fraction and the effective thickness of the *p*-type layer to keep out-of-band carriers from being collected at the terminal.

The sequential-mode detector has a single indium bump per unit cell that permits sequential bias selectivity of the spectral bands associated with operating back-to-back photodiodes. When the polarity of the bias voltage applied to the bump contact is positive, the top (LW) photodiode is reverse biased and the bottom (SW) photodiode is forward biased. The SW photocurrent is shunted by the low impedance of the forward-biased SW photodiode, and the only photocurrent to emerge in the external circuit is the LW photocurrent. When the bias voltage polarity is reversed, the situation reverses; only SW photocurrent is available. Switching times within the detector can be relatively short, on the order of microseconds, so detection of slowly changing targets or images can be achieved by switching rapidly between the MW and LW modes. The problems with the bias-selectable device are the following: its construction does not allow independent



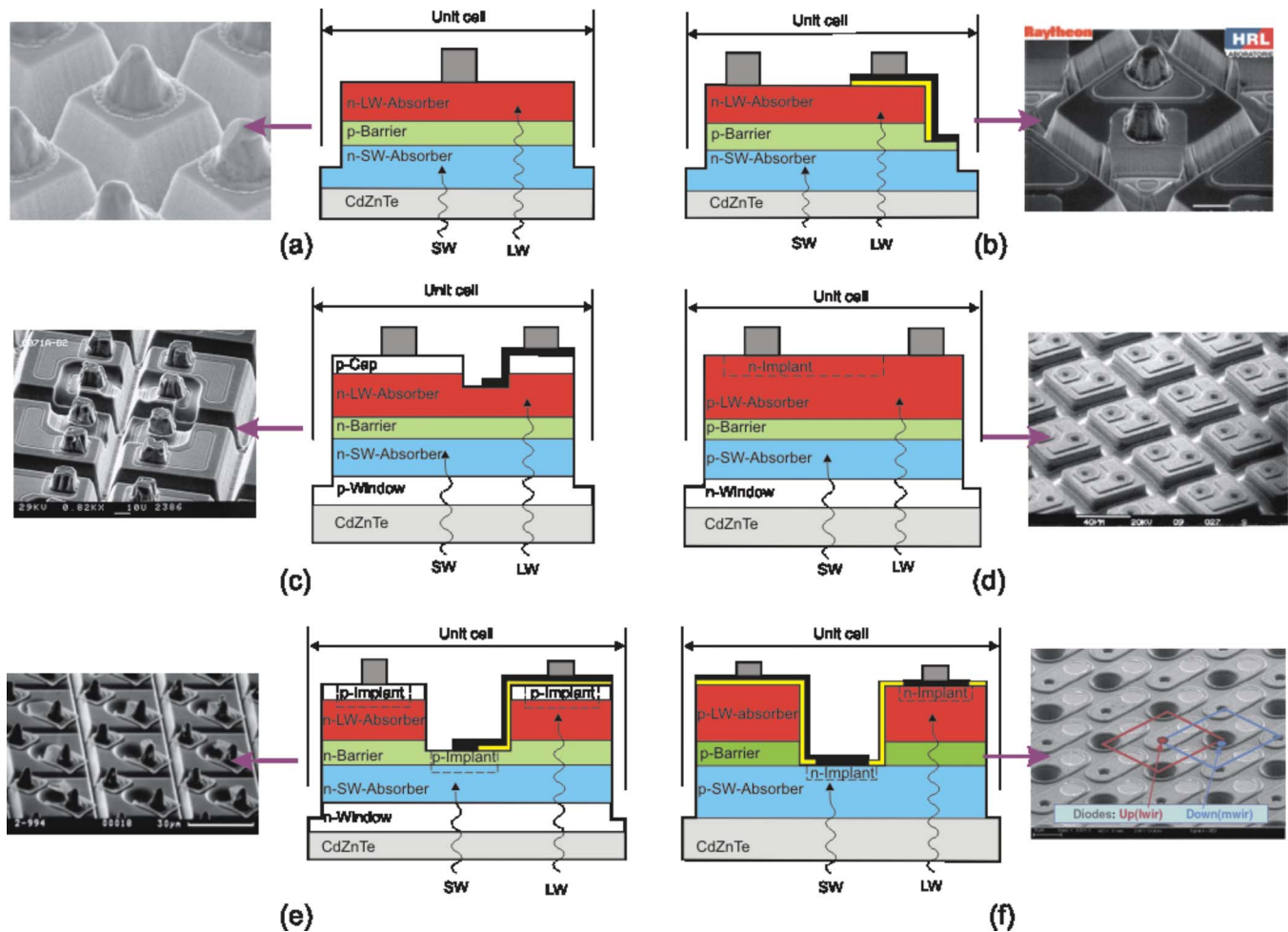


FIG. 39. (Color online) Cross section views of unit cells for various back-illuminated dual-band HgCdTe detector approaches: (a) bias-selectable  $n$ - $p$ - $n$  structure reported by Raytheon (Ref. 145), (b) simultaneous  $n$ - $p$ - $n$  design reported by Raytheon (Ref. 146), (c) simultaneous  $p$ - $n$ - $n$ - $p$  reported by BAE Systems (Ref. 150), (d) simultaneous  $n$ - $p$ - $p$ - $n$  design reported by Leti (Ref. 151), (e) simultaneous structure based on  $p$ -on- $n$  junctions reported by Rockwell (Ref. 157), and simultaneous structure based on  $n$ -on- $p$  junctions reported by Leti (Ref. 31).

selection of the optimum bias voltage for each photodiode, and there can be substantial MW cross-talk in the LW detector.

Multicolor detectors require deep isolation trenches to cut completely through the relatively thick (at least 10  $\mu\text{m}$ ) LWIR absorbing layer. The design of small two-color TLHJ detectors of less than 20  $\mu\text{m}$  pitch requires at least 15  $\mu\text{m}$  deep trenches, which are no more than 5  $\mu\text{m}$  wide at the top. Dry etching technology has been used for a number of years to produce two-color detectors. One of the material technologies being developed in order to meet the challenge of shrinking the pixel size to below 20  $\mu\text{m}$  is advanced etching technology. Recently, Raytheon developed an inductively coupled plasma (ICP) dry mesa etching capability to replace electron cyclotron resonance (ECR) dry mesa etching. The ICP, when compared to ECR, has shown reduced lateral mask erosion during etching, less significant etch-lag effects, and improved etch depth uniformity.<sup>157</sup> For the pseudoplanar devices the etching step is easier to perform because of the lower aspect ratio. Moreover, there is no electrical cross-talk as the pixels are electrically independent.

Many applications require true simultaneous detection in the two spectral bands. This has been achieved in a number

of ingenious architectures shown in Figs. 39(b)–39(f). Two different architectures are shown. The first one is the classical  $n$ - $P$ - $N$  back-to-back photodiode structure [Fig. 39(b)]. In the case of the architecture developed at Leti [Fig. 34(d)], the two absorption materials are  $p$ -type separated by a barrier to prevent any carrier drift between the two  $n$ -on- $p$  diodes. Each pixel consists of two standard  $n$ -on- $p$  photodiodes, where the  $p$ -type layers are usually doped with Hg vacancies. The shorter wavelength diode is realized during epitaxy by simply doping part of the first absorbing layer with In. The longer wavelength junction is obtained by a planar implantation process. It should be noted that the electron mobility is around 100 times greater in  $n$ -type material than holes in  $p$ -type material and, hence, the  $n$ -on- $p$  structures will have a much lower common resistance. This is an important consideration for large area FPAs with detection in the LW range due to the larger incident-photon flux.

The last two architectures shown in Figs. 39(e) and 39(f), called “pseudoplanar,” present a totally different approach. They are close to the structure proposed by Lockwood *et al.*<sup>159</sup> in 1976 for PbTe/PbSnTe heterostructure two-color photodiodes. They are based on the concept of two  $p$ -on- $n$  [Fig. 39(e)] or  $n$ -on- $p$  [Fig. 39(f)] diodes fabricated

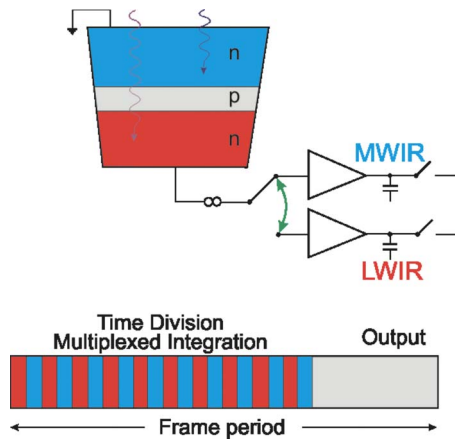


FIG. 40. (Color online) Raytheon's two-color FPAs with a TDMI scheme in which the detector bias polarity is alternated many times within a single frame period (after Ref. 147).

by *p*-type or *n*-type implantation, respectively, but on two different levels of a three layer heterostructure. The architecture developed by Rockwell is a simultaneous two-color MWIR/LWIR FPA technology based on a double-layer planar heterostructure MBE technology [Fig. 39(e)]. To prevent the diffusion of carriers between two bands, a wide-bandgap 1  $\mu\text{m}$  thick layer separates these two absorbing layers. The diodes are formed by implanting arsenic as a *p*-type dopant and activating it with an anneal. This results in a unipolar operation for both bands. The implanted area of band 2 is a concentric ring around the band 1 dimple. Because the lateral carrier-diffusion length is larger than the pixel pitch in the MWIR material, and band 1 junction is shallow, each pixel is isolated by dry etching a trench around it to reduce carrier cross-talk. The entire structure is capped with a layer of material with a slightly wider bandgap to reduce surface recombination and simplify passivation.

All these simultaneous dual-band detector architectures require an additional electrical contact from an underlying layer in the multijunction structure to both the SW and the LW photodiode. The most important distinction is the requirement of a second readout circuit in each unit cell.

It is expected that with the TLHJ architecture, pixel size could decrease to 15  $\mu\text{m}$ , and array format could increase to several megapixels. With the pseudoplanar architecture, MWIR/LWIR devices should be produced more easily, with large-format arrays having pixel size around 20  $\mu\text{m}$ .

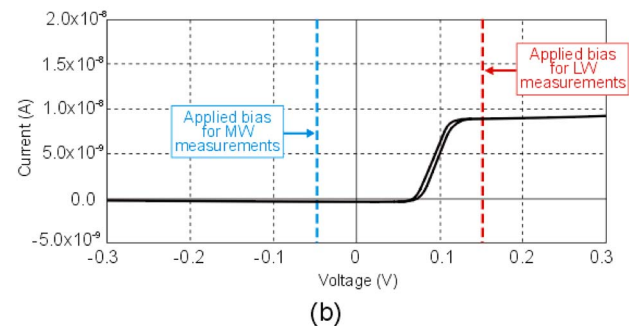
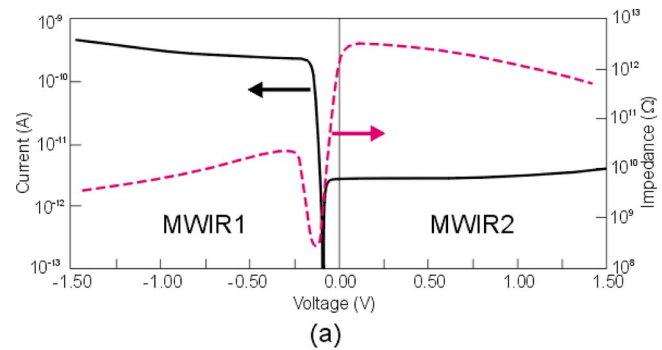


FIG. 41. (Color online) Typical *I*-*V* characteristics for a single mesa, single indium bump two-color TLHJ unit-cell detector design: (a) MWIR1/MWIR2 25  $\mu\text{m}$  pixel with cutoff wavelength at 3.1 and 5.0  $\mu\text{m}$  at 77 K and 30° FOV (after Ref. 160) and (b) MWIR/LWIR 20  $\mu\text{m}$  pixel with cutoff wavelength at 5.5 and 10.5  $\mu\text{m}$  (after Ref. 161).

Having only one bump contact per unit cell, as for single-color hybrid FPAs, is the major advantage of the bias-selectable detector. In addition, it is compatible with existing silicon readout chips. This structure achieves approximately 100% optical fill factor in each band due to total internal reflection of the incident radiation off the mesa sidewalls. Raytheon's approach employs a ROIC with time division multiplexed integration (TDMI),<sup>147</sup> see Fig. 40. As the detector bias is changed the detector current is directed to separate input circuitry and integration capacitors. The bias switching is performed at times much shorter than the frame period. Fast subframe switching of less than 1 ms is typically employed. The MWIR band is integrated by summing the charge collected from the individual subframe integration periods. The LWIR band is integrated by averaging the charge collected from the individual subframe integrations.

Figure 41 shows the current-voltage characteristics for a single mesa, single indium bump two-color MWIR1/

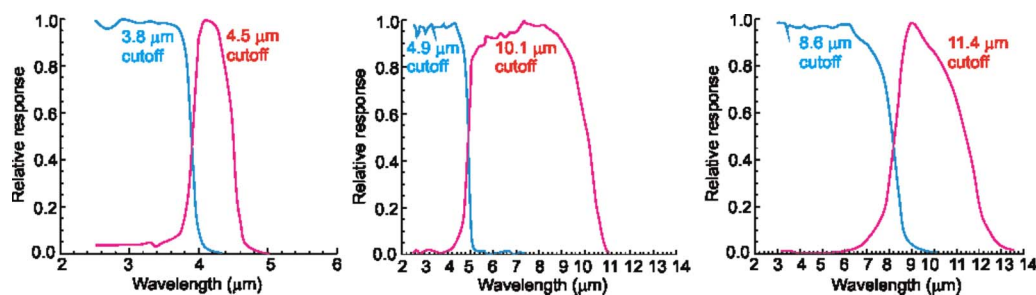


FIG. 42. (Color online) Spectral response curves for two-color HgCdTe detectors in various dual-band combinations of MWIR and LWIR spectral bands (after Ref. 38).

TABLE VI. Typical measured performance parameters for single- and dual-color HgCdTe MWIR and LWIR detector configurations for  $256 \times 256$   $30 \mu\text{m}$  unit-cell FPAs (after Ref. 148).

256 $\times$ 256 $30 \mu\text{m}$ unit-cell performance parameters	DLHJ single color		TLHJ sequential dual color					
	MWIR	LWIR	MWIR/MWIR		MWIR/LWIR		LWIR/LWIR	
Spectral band	MWIR	LWIR	Band 1	Band 2	Band 1	Band 2	Band 1	Band 2
78 K cutoff ( $\mu\text{m}$ )	5	10	4	5	5	10	8	10
Operating temperature (K)	78	78	120	120	70	70	70	70
Cross-talk (%)	...	...	<5	<10	<5	<10	<5	<10
Quantum efficiency (%)	>70	>70	>70	>65	>70	>50	>70	>50
$R_0A$ , zero FOV ( $\Omega \text{ cm}^2$ )	$>1 \times 10^7$	>500						
$R_A^a$ , zero FOV ( $\Omega \text{ cm}^2$ )	...	...	$6 \times 10^5$	$2 \times 10^5$	$1 \times 10^6$	$2 \times 10^2$	$5 \times 10^4$	$5 \times 10^2$
Interconnect operability (%)	>99.9	>99.9	>99.9	>99.9	>99.9	>99.9	>99.9	>99.9
Response operability (%)	>99	>98	>99	>97	>99	>97	>98	>95

<sup>a</sup>Resistance area product at nonzero bias.

MWIR2, and MWIR/LWIR TLHJ unit-cell detector design. With appropriate polarity and voltage bias at the pixel contact, the junctions respond to either shorter or longer wavelength IR radiation. The  $I$ - $V$  curves exhibit the serpentine shapes expected for a back-to-back diode structure; the “flatness” displayed in both effective reverse bias regions is a key indicator of high quality two-color diodes. Figure 42 illustrates examples of the spectral response from different two-color devices. Note that there is minimal cross-talk between the bands, since the short-wavelength detector absorbs nearly 100% of the shorter wavelengths. Test structures indicate that the separate photodiodes in a two-color detector perform exactly like single-color detectors in terms of achievable  $R_0A$  variation with wavelength at a given temperature (see Table VI).

The best performing bias-selectable dual-color FPAs being produced at Raytheon Vision Systems exhibit out-of-band cross-talk below 10%, 99.9% interconnect operability, and 99% response operability that is comparable to state-of-the-art, single-color technology. It is predicted that ongoing development of material growth and fabrication processes will translate to further improvements in dual-color FPA performance.

Recently, Raytheon Vision Systems has developed two-color, large-format IR FPAs to support the U.S. Army’s third-generation FLIR systems. RVS has produced  $1280 \times 720$  two-color FPAs with a  $20 \mu\text{m}$  pixel pitch. High-quality MWIR/LWIR  $1280 \times 7200$  FPAs have cutoffs ranging out to  $11 \mu\text{m}$  at 78 K. These FPAs have demonstrated excellent sensitivity and pixel operabilities exceeding 99.9% in the MW band and greater than 98% in the LW band. Table VII provides a summary of the sensitivity and operability data measured for the three best  $1280 \times 720$  FPAs fabricated to

date. Median 300 K NEDT values at  $f/3.5$  of approximately 20 mK for the MW and 25 mK for the LW have been measured for dual-band TDMI operation at 60 Hz frame rate with integration times corresponding to roughly 40% (MW) and 60% (LW) of full well charge capacities. As shown in Fig. 43, excellent high resolution IR camera imaging with  $f/2.8$  field of view (FOV) broadband refractive optics at 60 Hz frame rate has been achieved.

Impressive results have also been demonstrated for other architectures. For example, the NEDT of  $128 \times 128$  simultaneous MWIR1-MWIR2 FPAs [see device architecture in Fig. 39(b)] for both bands (2.5–3.9 and 3.9–4.6  $\mu\text{m}$ ) was below 25 mK (see Fig. 44), and imagery was acquired at temperatures as high as 180 K with no visible degradation in image quality. The camera used for these measurements had a 50 mm,  $f/2.3$  lens. Also, high-performance two-color  $128 \times 128$  FPAs with  $40 \mu\text{m}$  pitch have also been obtained using the pseudoplanar simultaneous architecture shown in Fig. 39(e). Background-limited detectivity performance has been obtained for MWIR (3–5  $\mu\text{m}$ ) devices at  $T < 130$  K and for LWIR (8–10  $\mu\text{m}$ ) devices at  $T \approx 80$  K (see Fig. 45). The FPA also exhibits low NEDT values: 9.3 mK for the MW band and 13.3 mK for the LW band, similar to good quality single-color FPAs.

Two-color MWIR/LWIR HgCdTe detectors have been examined theoretically.<sup>38,164–166</sup> It has been shown that it is possible to predict, with relatively good accuracy, the performance of complex detectors by using numerical models. Furthermore, the simulation technique is also useful for understanding the effects of different material parameters and geometrical characteristics on the detector performance.

TABLE VII. Performance summary of three best  $1280 \times 720$  MW/LW FPAs fabricated to date (after Ref. 36).

FPA	Wafer	MW $t_{\text{int}}$ (ms)	MW median NETD (mK)	MW response operability (%)	LW $t_{\text{int}}$ (ms)	LW median NETD (mK)	LW response operability (%)
760 7780	3827	3.14	23.3	99.7	0.13	30.2	98.5
761 6474	3852	3.40	18.0	99.8	0.12	27.0	97.0
761 6475	3848	3.40	18.0	99.9	0.12	26.8	98.7



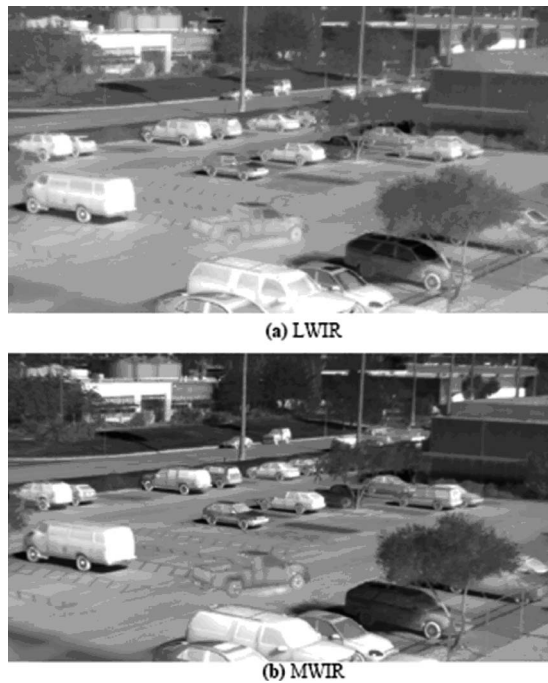


FIG. 43. A still camera image taken at 78 K with  $f/2.8$  FOV and 60 Hz frame rate using two-color 20  $\mu\text{m}$  unit-cell MWIR/LWIR HgCdTe/CdZnTe TLHJ  $1280 \times 720$  FPA hybridized to a  $1280 \times 720$  TDMI ROIC (after Ref. 162).

The HgCdTe HDVIP or loophole concept (see Fig. 15), developed at DRS and BAE Southampton, represents an alternative approach to IR FPA architecture. It differs from the more entrenched FPA architectures in both its method of diode formation and the manner of its hybridization to the silicon ROIC.<sup>61</sup> The monocular HDVIP architecture consists of a single HgCdTe epilayer grown on CdZnTe substrate by LPE or MBE.<sup>156</sup> After epitaxial growth, the substrate is removed and the HgCdTe layer is passivated on both surfaces with interdiffused layers of evaporated CdTe (the interdiffusion at 250 °C on the Te-rich side of the phase field generates about  $10^{16} \text{ cm}^{-3}$  metal vacancies). During this process the Cu can also be indiffused from a doped ZnS source providing an alternative to doping during growth. This single-color architecture has been extended to two colors at DRS by gluing two monocular layers together into a composite and forming an insulated via through the lower layer in order to read out the upper color, as illustrated in Fig. 46. Contact to

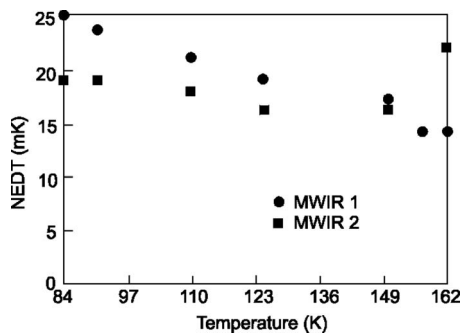


FIG. 44. NEΔT for a two-color camera having 50 mm,  $f/2.3$  lens, as a function of the operating temperature (after Ref. 163).

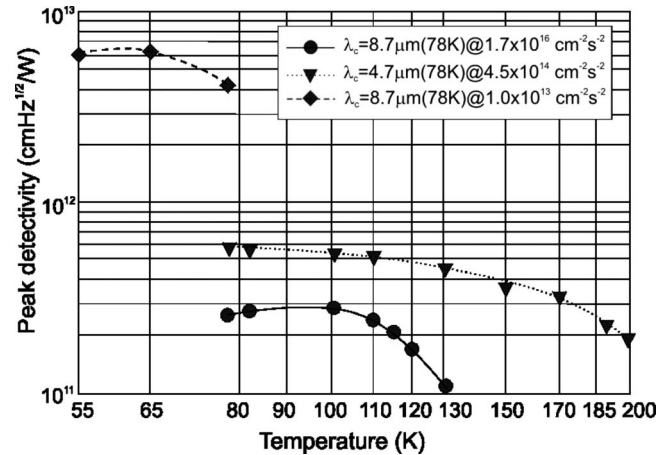


FIG. 45. Detectivity of two color pseudoplanar simultaneous MWIR/LWIR  $128 \times 128$  HgCdTe FPA (after Ref. 157).

the Si ROIC is obtained by etching holes (or vias) through the HgCdTe down to contact pads on the Si [see Fig. 46(c)]. The ROIC used for the dual-band FPA was originally designed for a single-color  $640 \times 480$  array with 25  $\mu\text{m}$  (square) pixels. The even-numbered rows of the ROIC have no detectors attached to them, so the chip is operated in a mode that only outputs the odd rows. Odd-numbered columns connect to LWIR detectors, and the MWIR detectors are on the even columns. This approach has been utilized to fabricate both MW-LW and MW-MW  $240 \times 320$  FPAs on a 50  $\mu\text{m}$  pitch. Higher densities are being investigated with dedicated two-color ROIC designs, enabling pitches of  $<30 \mu\text{m}$  for two-color FPAs.

Performance data for representative DRS two-color MW-LW and MW-MW  $240 \times 320$  FPAs utilizing  $f/3$  optics and a 60 Hz frame rate are shown in Table VIII. Composite operabilities  $>92.5\%$  have been achieved. However, relatively low collection efficiency (the product of quantum efficiency and unit cell fill factor) has been measured on the LWIR layer. A recently published paper describes operabilities in excess of 99%.<sup>156</sup>

### B. Three-color HgCdTe detectors

Some system considerations suggest that three-color FPAs would be more generally useful than two-color ones. The successful development of three-color HgCdTe FPAs requires further improvement in the material quality, adequate processing techniques, and a better understanding of imager operation both in terms of pixel performance and interaction between different pixels in the array.

Recently, the first concept for achieving three-color HgCdTe detectors has been demonstrated by British workers.<sup>167</sup> The concept of a back side illuminated HgCdTe detector is shown schematically in Fig. 47. The bias-dependent cutoff is achieved by using three absorbers in a  $n$ - $p$ - $n$  structure in which the first  $n$ -layer defines the shorter wavelength (SW) region; the  $p$ -type layer—the intermediate wavelength region (IW); and the top layer—the long-wavelength (LW) region. Note that the terms SW and LW used here are relative and do not necessarily coincide with the SW and LW IR bands. The cutoff wavelengths of the SW,

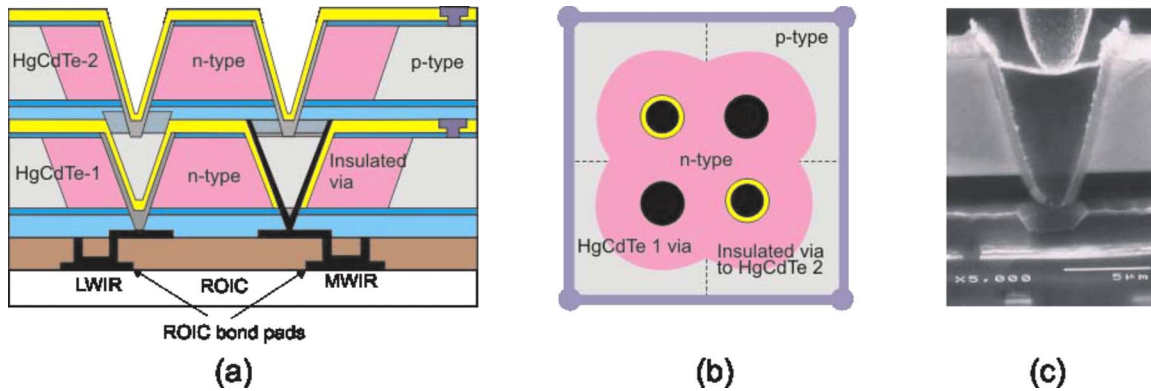


FIG. 46. (Color online) Two-color HDVIP architecture is composed to two layers of thinned HgCdTe epoxied to a silicon readout: (a) side view, (b) top view (after Ref. 156), and (c) small hole etched to form junction and to contact the Si readout.

IW, and LW regions are, respectively, marked as  $\lambda_{c1}$ ,  $\lambda_{c2}$ , and  $\lambda_{c3}$ . Since the barrier region is low doped, the applied bias mainly falls on this side of the junction. For the device configuration shown in Fig. 47, the negative bias denotes higher potential of contact A in comparison with contact B.

It is expected that at low biases either the SW or LW response would dominate, depending on which junction is reverse biased. In this case we have the same situation as in the bias-selectable two-color detector since the barriers prevent electron flow from the IW layer—both generated photoelectrons as well as direct injected carriers from the forward biased junction. Increasing reverse bias reduces the barrier and electrons photogenerated in the IW layer can cross the junction. As a result, the cutoff wavelength changes from the SW to the IW as the bias is increased. This situation, with negative bias, and corresponding changes in spectral response, is shown in Fig. 48(c). Changing the bias direction to positive shifts the cutoff wavelength to the LW region [see Fig. 48(d)]. Similarly, increasing positive bias moves the cut-on from being coincident with the IW cutoff to the SW cutoff. It should be noted that the above considerations concern the ideal case of the detector structure. The ideal LW response may not be achievable in practice due to the IW absorber being insufficiently thick to absorb all the IW radiation.

The three-color HgCdTe detectors were grown by MOVPE on GaAs substrates oriented off the (100) direction to reduce the size of pyramidal hillock growth defects. Figure 49 shows the spectral response with cutoff wavelengths of 3 (SW), 4 (IW), and 6  $\mu\text{m}$  (LW). In positive bias mode the LW/IW junction is in reverse bias and a bias independent LW spectrum is obtained above 0.2 V (shown only for +0.6 V). No barrier lowering at the LW/IW junction at these applied biases is observed due to the chosen doping levels.

The response below  $\lambda_2$  is due to incomplete absorption in the IW layer resulting in carrier generation in the LW layer at these wavelengths (carriers generated in the IW absorber have insufficient energy to surmount the LW barrier). As the positive bias is reduced below 0.2 V, the LW response collapses and a signal from the SW layer appears with the current flowing in the opposite direction. For this bias regime the built-in fields dominate and the largest field is at the SW/IW junction due to the larger band gap. Further reduction in the bias voltage causes the SW response to grow. The negative voltage puts the SW/IW junction into reverse bias and results in a SW response with cutoff  $\lambda_1$ . Further increase in the negative bias lowers the barrier at this junction and allows a response from the IW layer, thus moving the cutoff to  $\lambda_2$ . The observed increase in the SW signal with increasing negative bias is caused by incomplete absorption in the SW absorption.

Because of the complicated and expensive fabrication process, numerical simulation has become a critical tool for the development of HgCdTe bandgap engineered devices. The numerical simulations can provide valuable guidelines for the design and optimization of the pixel structure and the array geometry. Up until now, only a limited number of theoretical papers have been published that study the performance of three-color detectors.<sup>167,168</sup> Józwiński and Rogalski<sup>168</sup> showed that the performance of a three-color detector is critically dependent on the barrier doping level and position in relation to the junction. A small shift of the barrier location and doping level causes significant changes in spectral responsivity. This behavior is a serious disadvantage of the considered three-color detector. Therefore, this type of detector structure presents some serious technological challenges.

TABLE VIII. Performance data of two-color MW/LW and MW/MW  $240 \times 320$  HgCdTe FPAs:  $f/3$  optics, 60 Hz frame rate (after Ref. 61).

	Spectral bands ( $\mu\text{m}$ )	Pitch ( $\mu\text{m}$ )	SNR operability (%)	CE (%)	Response uniformity ( $\sigma/\text{mean}$ )	NEDT (mK)
$320 \times 240$ MW/LW	3.0–5.2/8.0–10.2	50	97.1/96.3	60/35	4.9%/4.2%	9/23
$320 \times 240$ MW/MW	3.0–4.2/4.2–5.2	50	99.4/99.6	58/58	4.3%/3.7%	18.1/8.3

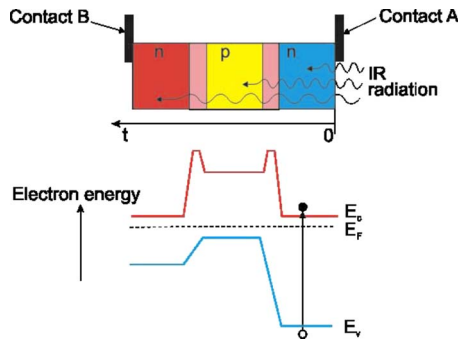


FIG. 47. (Color online) Three-color concept and associated zero-bias band diagram (after Ref. 167).

## VIII. MULTIBAND QWIPS

QWIPs are ideal detectors for the fabrication of pixel coregistered simultaneously readable two-color IR FPAs because a QWIP absorbs IR radiation only in a narrow spectral band and is transparent outside of that absorption band. Thus it provides zero spectral cross-talk when two spectral bands are more than a few microns apart. Individual pixels in a multiband QWIP detector array are fabricated using a process similar to that used for their singleband counterparts, except for the via holes that need to be added to electrically connect with the silicon ROIC.

Sanders was the first organization to fabricate two-color,  $256 \times 256$  bound-to-miniband QWIP FPAs in each of four important combinations: LWIR/LWIR, MWIR/LWIR, near-IR (NIR)/LWIR, and MWIR/MWIR—with simulta-

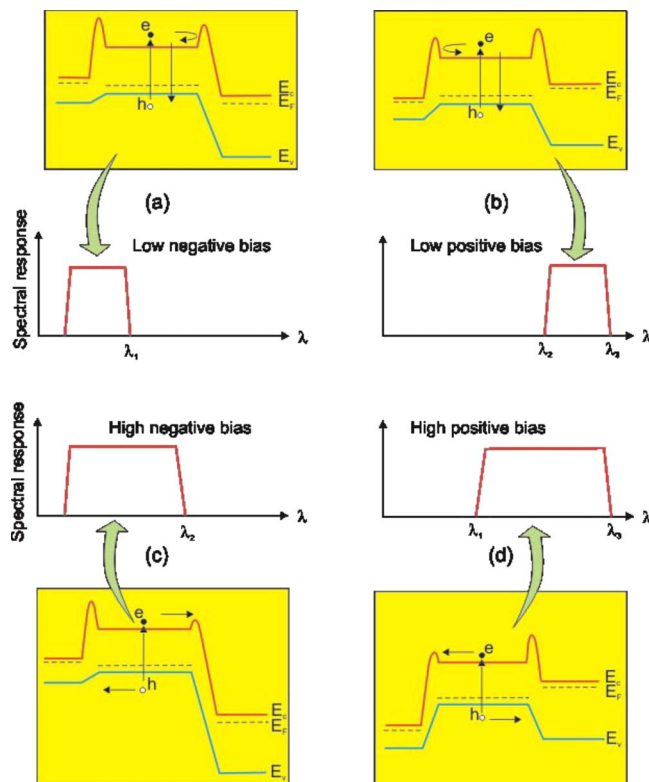


FIG. 48. (Color online) Idealized spectral responses of three-color detector. Effect of negative and positive bias voltages on band gap structure is also show (after Ref. 167).

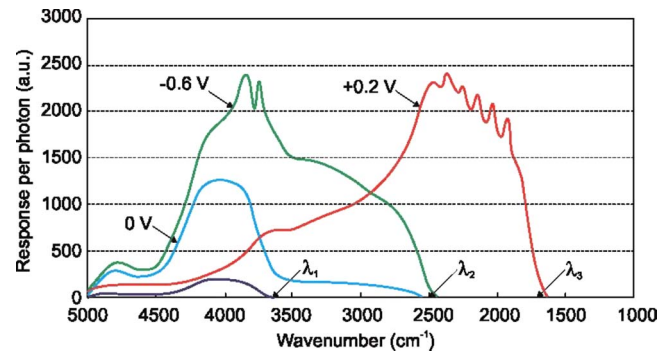


FIG. 49. (Color online) Spectral response of a three-color HgCdTe detector with cutoff wavelengths of 3, 4, and 6  $\mu\text{m}$  at various biases (after Ref. 167).

neous integration.<sup>169,170</sup> At present multicolor QWIP detectors are fabricated at Jet Propulsion Laboratory (JPL),<sup>28,43,171–174</sup> Army Research Laboratory,<sup>89,175</sup> Goddard,<sup>176</sup> Thales,<sup>41,44,177</sup> and AIM<sup>42,114,178,179</sup> with the majority being based on bound-to-extended transitions.

Devices capable of simultaneously detecting two separate wavelengths can be fabricated by vertical stacking of the different QWIP layers during epitaxial growth. Separate bias voltages can be applied to each QWIP simultaneously via doped contact layers that separate the MQW detector heterostructures. Figure 50(a) shows schematically the structure of a two-color stacked QWIP with contacts to all three Ohmic-contact layers. The device epilayers are grown by MBE on up to 6 in. semi-insulating GaAs substrates. An undoped GaAs layer, called an isolator, is grown between two AlGaAs etch stop layers, followed by a 0.5  $\mu\text{m}$  thick doped GaAs layer. Next, the two QWIP heterostructures are grown, separated by another Ohmic contact. The long-wavelength-sensitive stack (red QWIP) is grown above the shorter-wavelength-sensitive stack (blue QWIP). Typical responsivity spectra at 77 K using a common bias of 1.5 V, recorded simultaneously for two QWIPs at the same pixel, are shown in Fig. 50(b). Each QWIP consists of about 20-period GaAs/ $\text{Al}_x\text{Ga}_{1-x}\text{As}$  MQW stack in which the thickness of the Si-doped GaAs QWs (with typical electron concentration of  $5 \times 10^{17} \text{ cm}^{-3}$ ) and the Al composition of the undoped  $\text{Al}_x\text{Ga}_{1-x}\text{As}$  barriers ( $\approx 550$  to  $600 \text{ \AA}$  thick) is adjusted to yield the desired peak responsivity position and spectral width. The gaps between FPA detectors and the readout multiplexer are backfilled with epoxy. The epoxy backfilling provides the necessary mechanical strength to the detector array and readout hybrid prior to array thinning. The initial GaAs substrate of dual-band FPAs is completely removed leaving only a 50 nm thick GaAs membrane. This allows the array to accommodate any thermal expansion by eliminating the thermal mismatch between the silicon readout and the detector array. It also eliminates pixel-to-pixel cross-talk and, finally, significantly enhances the optical coupling of IR radiation into the QWIP pixels. Using the above-described fabrication process, significant progress has been made toward development of a megapixel dual-band QWIP FPA.<sup>43</sup>

Figure 51 provides additional insight into dual-band QWIP processing technology developed at JPL, based on 4 in. wafers to fabricate  $320 \times 256$  MWIR/LWIR dual-band



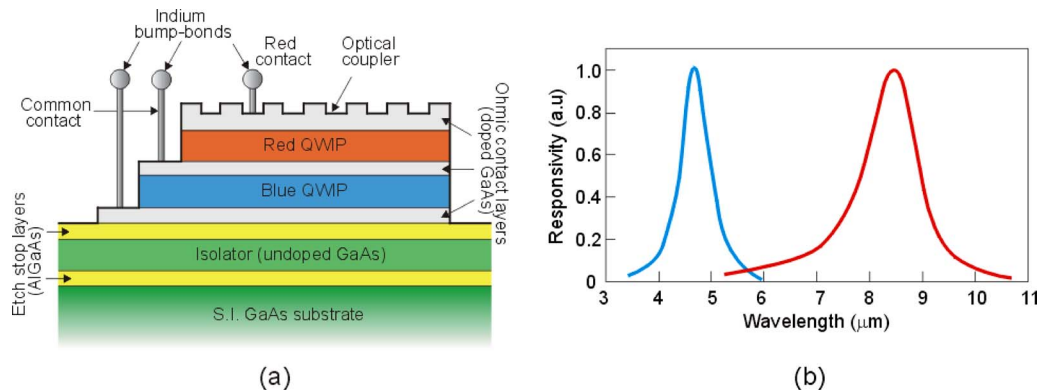


FIG. 50. (Color online) Schematic representation of the dual-band QWIP detector structure (a) and typical responsivity spectra at 77 K and a common bias of 1 V, recorded simultaneously for two QWIPs at the same pixel (b) (after Ref. 43).

QWIP devices with pixels colocated and simultaneously readable. As shown in Fig. 51(b), the carriers emitted from each MQW region are collected separately using three contacts. The middle contact layer [see Fig. 51(c)] is used as the detector common. The electrical connections to the detector common and the LWIR connection are brought to the top of each pixel using via connections. Electrical connections to the common contact and the LWIR pixel connection are brought to the top of each pixel using the gold via connections visible in Fig. 51. This elaborate processing technology could lead to 2D imaging arrays that can detect three separate bands on a single pixel.

Most QWIP arrays use a 2D grating, which has the disadvantage of being very wavelength dependent, combined with an efficiency that decreases as the pixel size is reduced. Lockheed Martin have used rectangular and rotated rectangular 2D gratings for their two-color LW-LW FPAs. Although random reflectors have achieved relatively high quantum efficiencies with large test device structures, it is not possible to achieve comparable quantum efficiencies with random reflectors on small FPA pixels due to the reduced

width-to-height aspect ratios.<sup>171</sup> In addition, it is more difficult to fabricate random reflectors for shorter-wavelength detectors because feature sizes of random reflectors are linearly proportional to the peak wavelength of the detectors. Thus, quantum efficiency becomes a more difficult issue for multicolor QWIP FPAs in comparison to single-color arrays. At JPL two different optical coupling techniques have been developed. The first technique uses a dual period Lamar grating structure, and the second is based on multiple diffraction orders [see Figs. 51(c) and 51(d)].<sup>180</sup>

Typical operating temperatures for QWIP detectors are in the range of 40–80 K. The bias across each QWIP can be adjusted separately, although it is desirable to apply the same bias to both colors. Results indicate that the complex two-color processing has not compromised the electrical and optical quality of either FPA in the two-color device, since the peak quantum efficiency for each of the 20-period QWIPs was estimated to be  $\approx 10\%$ . For comparison, a normal single-color QWIP with twice the number of periods has a quantum efficiency of around 20%. An accurate design methodology is needed to optimize the detector structure to meet different requirements. In the production process, the fabrication of gratings is still quite an involved process, and the detector quantum efficiency is rather uncertain in small pixels and in pixels with thick material layers.

Development of dual-band QWIP FPAs has been undertaken at JPL over the last decade with the objective of developing  $640 \times 480$  LWIR/VLWIR arrays for moderate background applications.<sup>172</sup> One of the key issues has been the scarcity of appropriate readout multiplexers. To overcome this problem, JPL has chosen to demonstrate initial dual-band concepts with existing multiplexers developed for

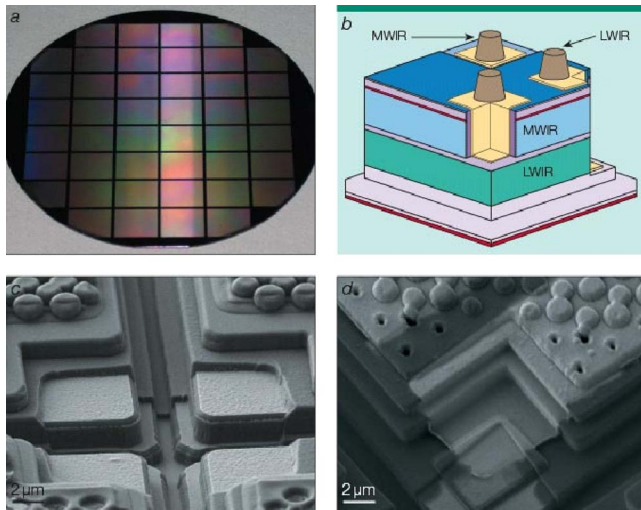


FIG. 51. (Color online) Two-color MWIR/LWIR QWIP FPA: (a) 48 FPAs processed on a 4 in. GaAs wafer, (b) 3D view of pixel structure, (c) electrical connections to the common contact, and (d) the pixel connections are brought to the top of each pixel using the gold via connections (after Ref. 180).

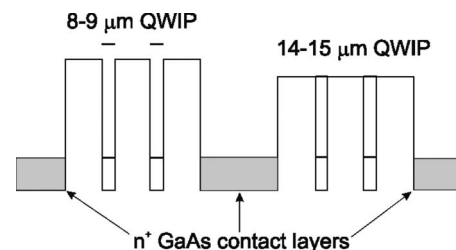


FIG. 52. Conduction band diagram of a LWIR and a VLWIR two-color detector (after Ref. 172).

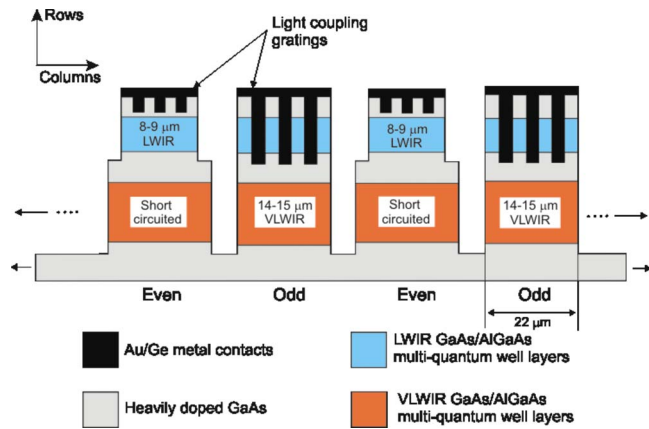


FIG. 53. (Color online) Structure cross section of the interlace dual-band FPA (after Ref. 172).

single-color applications and use a waveband-interlaced CMOS readout architecture (i.e., odd rows for one color and even rows for the other color). This scheme has the disadvantage that it does not provide a full fill factor for both wavelength bands, resulting in an approximate 50% fill factor for each wavelength band. The device structure, shown in Fig. 52, consists of a 30-period stack (500 Å AlGaAs barrier and 60 Å GaAs well) of VLWIR structure and an 18-period stack (500 Å AlGaAs barrier and 40 Å GaAs well) of LWIR structure, separated by a heavily doped 0.5 μm thick intermediate GaAs contact layer. The VLWIR QWIP structure has been designed to have a bound-to-quasibound intersubband absorption peak at 14.5 μm, whereas the LWIR QWIP structure has been designed to have a bound-to-continuum intersubband absorption peak at 8.5 μm, primarily because the photocurrent and dark current of the LWIR device structure are small compared to those of the VLWIR portion.

Figure 53 shows a schematic side view of the interlaced dual-band GaAs/AlGaAs FPA. Two different 2D periodic grating structures were designed to independently couple the 8–9 and 14–15 μm radiation into detector pixels in even and odd rows of the FPA, respectively. The top 0.7 μm thick GaAs cap layer was used to fabricate the light-coupling 2D periodic gratings for 8–9 μm detector pixels, whereas the light-coupling 2D periodic gratings of the 14–15 μm detector pixels were fabricated through the LWIR MQW layers. Thus, this grating scheme short circuited all 8–9 μm sensitive detectors in all odd rows of the FPAs. Next, the LWIR detector pixels were fabricated by dry etching through the photosensitive GaAs/AlGaAs MQW layers into the 0.5 μm thick doped GaAs intermediate contact layer. All VLWIR pixels in the even rows of the FPAs were short circuited. The VLWIR detector pixels were fabricated by dry etching through both MQW stacks into the 0.5 μm thick heavily doped GaAs bottom contact layer. After epoxy backfilling of the gaps between FPA detectors and the readout multiplexer, the substrate was thinned, and finally the remaining GaAs/AlGaAs material contained only the QWIP pixels and a very thin membrane ( $\approx 1000$  Å).

The 640×486 GaAs/AlGaAs array provided images with 99.7% of the LWIR pixels and 98% of VLWIR pixels working, demonstrating the high yield of GaAs technology.

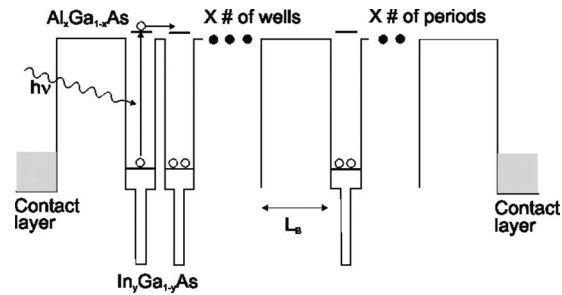


FIG. 54. Schematic of the conduction band in a bound-to-quasibound QWIP. A couple quantum-well structure has been used to broaden the responsivity spectrum (after Ref. 43).

The 8–9 μm detectors have shown BLIP at 70-K operating temperature, at 300 K background with an  $f/2$  cold stop. The 14–15 μm detectors show BLIP with the same operating conditions at 45 K. The performance of these dual-band FPAs was tested at a background temperature of 300 K, with  $f/2$  cold stop, and a 30 Hz frame rate. The estimated NEDTs of LWIR and VLWIR detectors at 40 K were 36 and 44 mK, respectively. The experimentally measured values of the LWIR NEDT, equal to 29 mK, were lower than the estimated ones. This improvement was attributed to the light-coupling efficiency of the 2D periodic grating. However, the experimental VLWIR NEDT value was higher than the estimated value. That was probably a result of inefficient light coupling in the 14–15 μm region, readout multiplexer noise, and noise of the proximity electronics. At 40 K, the performance of detector pixels in both bands was limited by photocurrent noise and readout noise.

To cover the MWIR range, a strained-layer InGaAs/AlGaAs material system is used. InGaAs in the MWIR stack produces high in-plane compressive strain, which enhances the responsivity. The MWIR-LWIR FPAs fabricated by the Sanders organization consisted of an 8.6 μm cutoff GaAs/AlGaAs QWIP on top of a 4.7 μm cutoff strained InGaAs/GaAs/AlGaAs heterostructure. The fabrication process allowed for fill factors of 85% and 80% for the MW and LW detectors, respectively. The first FPAs with this configuration had operability in excess of 97%, and NEDT values better than 35 mK with  $f/2$  optics.

The first dual-band QWIP FPA with pixel colocation and simultaneous operation in MWIR and LWIR has been described by Goldberg *et al.*<sup>175</sup> This 256×256 pixel FPA has achieved a NEDT of 30 mK in the MWIR spectral band and 34 mK in the LWIR spectral band.

Recently, Gunapala *et al.*<sup>43</sup> demonstrated a 320×256 MWIR/LWIR pixel collocated and simultaneously readable dual-band QWIP FPA. The device structures of the MWIR and LWIR devices are very similar to the structure shown in Fig. 54. Each period of the MQW structure consists of coupled QWs of 40 Å containing 10 Å GaAs, 20 Å In<sub>0.3</sub>Ga<sub>0.7</sub>As, and 10 Å GaAs layers (doped  $n=1 \times 10^{18}$  cm<sup>-3</sup>) and a 40 Å undoped barrier of Al<sub>0.3</sub>Ga<sub>0.7</sub>As between coupled QWs, and a 400 Å thick undoped barrier of Al<sub>0.3</sub>Ga<sub>0.7</sub>As. It is worth noting that the active MQW region of each QWIP device is transparent at other wavelengths, which is an important advantage over conventional interband

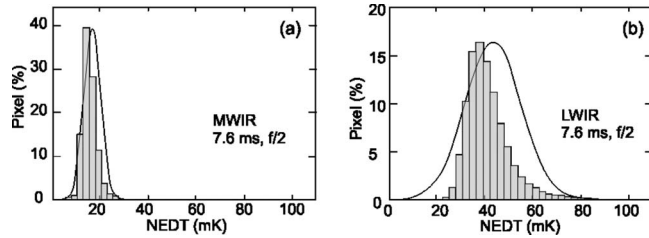


FIG. 55. NEDT-histogram of the MWIR (a) and LWIR (b) response of a dual-band QWIP FPA (after Ref. 179).

detectors. The experimentally measured NEDT of MWIR and LWIR detectors at 65 K were 28 and 38 mK, respectively.

Another design structure for dual-band MWIR/LWIR QWIPs has been proposed by Schneider *et al.*<sup>179</sup> This simultaneously integrated  $384 \times 288$  FPA with  $40 \mu\text{m}$  pitch comprises a photovoltaic and a photoconductive QWIP for the LWIR and MWIR, respectively (see Fig. 26). Excellent NEDT (17 mK) is obtained in the MWIR band (Fig. 55). Owing to the nonoptimized coupling for LWIR wavelengths, the observed NEDT is higher, but still shows a reasonable value of 43 mK. Due to improvements in the device design, excellent thermal resolution with  $\text{NEDT} < 30 \text{ mK}$  ( $f/2$  op-



FIG. 56. Images of the scene taken with a dual band  $384 \times 288$  QWIP demonstration camera with a 100 mm optics under severe weather conditions (cloudy sky, outside temperature below  $0^\circ\text{C}$  in winter, 2 pm). The church tower is at a distance of 1200 m. The left image shows the scene in the MW; the right image shows in the LW (after Ref. 181).

tics and full frame time of 6.8 ms) for both peak wavelengths ( $4.8$  and  $8.0 \mu\text{m}$ ) has been demonstrated. Examples of images taken with a dual-band  $384 \times 288$  FPA are shown in Fig. 56. The features and performance of the dual band QWIP fabricated by AIM GmbH are summarized in Table IX. This table also compares performance of the Eagle camera fabricated by commercial vendor QmagiQ LLC.<sup>181</sup>

The potential of QWIP technology is connected with multicolor detection. A four-band hyper spectral  $640 \times 512$  QWIP array was successfully developed under a joint

TABLE IX. Specification of the dual band QWIP FPAs. (a) AIM Infrarot-Module GmbH (after Ref. 42). (b) QmagiQ LLC (after Ref. 181).

(a) Technology		QWIP dual band, CMOC MUX	
Spectral bands		$\lambda_p = 4.8 \mu\text{m}$ ; $\lambda_p = 7.8 \mu\text{m}$ with temporal coincident integration in both spectral bands	
Type		Low noise for LW; photoconductive highly doped for MW	
Elements		$388 \times 284 \times 2$ ; $40 \mu\text{m}$ pitch	
Operability		$>99.5\%$	
Biasing		Individually for both bands	
NEDT		$<30 \text{ mK}$ at $f/2$ and 6.8 ms for both spectral bands	
Read put models		Snapshot, stare then scan, temporal signal coincidence in both bands	
Subframes		Arbitrary in steps of 8	
Data rate digital		80 MHz serial high speed link interface	
Full frame rate		50 Hz for $t_{\text{int}} = 16.8 \text{ ms}$ ; 100 Hz for $t_{\text{int}} = 6.8 \text{ ms}$	
IDCA		1.5 W split linear cooler	
(b) Parameter	MW	LW	Conditions
Array format	$320 \times 256$		
Pixel pitch ( $\mu\text{m}$ )	40		
Operating temperature (K)	68		
Optical response ( $\text{mV}/^\circ\text{C}$ )	$20 \pm 5$	$20 \pm 5$	$f/2.3$ cold shield, ROIC gain setting of 1, 1V bias, 300 K scene
Uncorrected response uniformity (%)	$5 \pm 2$	$3 \pm 2$	Aperture shading effects removed
Corrected response uniformity (%)	0.1–0.2	0.1–0.2	$30^\circ\text{C}$ scene temperature after a two-point NUC at 20 and $40^\circ\text{C}$
Temporal NEDT mean (mK)	35–45	25–35	$f/2.3$ , 17 ms integration time, 30 Hz frame rate
Temporal NEDT standard deviation (mK)	$3 \pm 1$	$3 \pm 1$	
Operating temperature (K)	68–70		Dark current and noise increase with operating temperature
Overall operability (%)	$>99.5$	$>99.5$	Actual value depends on performance specs.
ISC0006 power dissipation (MW)	$\sim 80$		



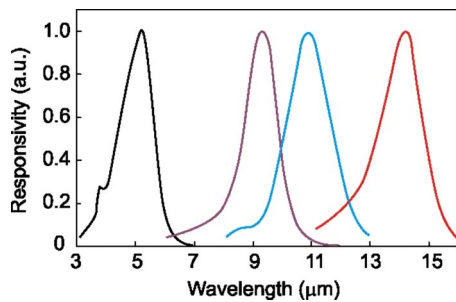


FIG. 57. (Color online) Normalized spectral response of the four-band QWIP FPA (after Ref. 183).

Goddard-Jet Propulsion Laboratory-Army Research Laboratory project funded by the Earth Science Technology Office of NASA. The device structure consists of a 15-period stack of 3–5  $\mu\text{m}$  QWIP structure, a 25-period stack of 8.5–10  $\mu\text{m}$  QWIP structure, a 25-period stack of 10–12  $\mu\text{m}$  QWIP structure, and a 30-period stack of 14–15.5  $\mu\text{m}$  QWIP structure (see Fig. 57).<sup>174,182</sup> The VLWIR QWIP structure has been designed to have bound-to-quasibound intersubband absorption, whereas the other QWIP device structures have been designed to have bound-to-continuum intersubband absorption, since the photocurrent and dark current of these devices are small in comparison to those of the VLWIR device.

The four bands of the QWIP array were fabricated in a manner similar to the two-band system described above (see Fig. 53). Four separate detector bands were defined by a deep trench etch process and the unwanted spectral bands were eliminated by a detector short-circuiting process using gold-coated reflective 2D etched gratings as shown in Fig. 58.

Video images were taken at a frame rate of 30 Hz and at a temperature of 45 K, using a ROIC capacitor having a charge capacity of  $1.1 \times 10^7$  electrons. As shown in Fig. 59, it is noticeable that the object in the 13–15  $\mu\text{m}$  spectral band is not very clear due to the reduced optical transmission of the germanium lens beyond 14  $\mu\text{m}$ . Figure 60 displays the peak detectivities of all spectral bands as a function of operating temperature. From Fig. 60 it is evident that the BLIP temperatures are 40, 50, 60, and 100 K for the 4–6, 8.5–10, 10–12, and 13–15  $\mu\text{m}$  spectral bands, respectively.

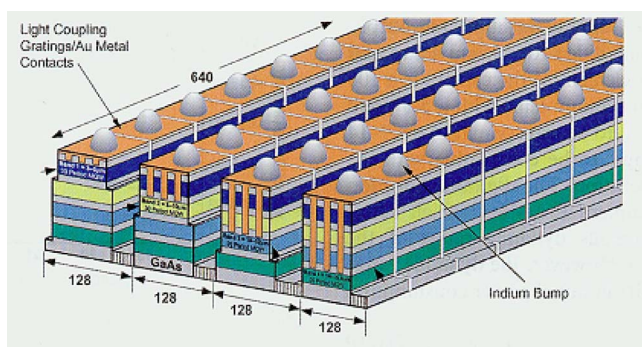


FIG. 58. (Color online) Layer diagram of the four-band QWIP device structure and the deep groove 2D-periodic grating structure. Each pixel represents a  $640 \times 128$  pixel area of the four-band FPA (after Ref. 183).

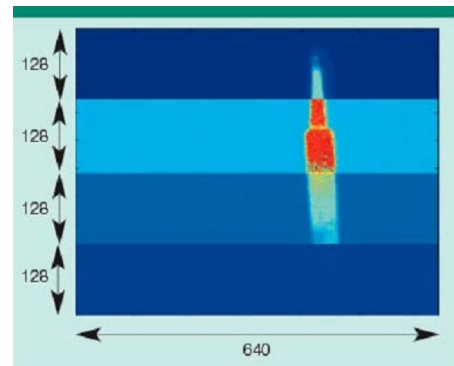


FIG. 59. (Color online) One frame of video image taken with the 4–15  $\mu\text{m}$  cutoff four-band  $640 \times 512$  pixel QWIP camera. The image is barely visible in the 13–15  $\mu\text{m}$  spectral band due to the poor optical transmission of the AR layer coated germanium lens (after Ref. 183).

The experimentally measured NEDT of 4–6, 8.5–10, 10–12, and 13–15  $\mu\text{m}$  detectors at 40 K are 21, 45, 14, and 44 mK, respectively.

The above results indicate that QWIPs have shown significant progress in recent years, especially in their applications to the multiband imaging problem. It is a niche in which they have an intrinsic advantage due to the comparative ease of growing multiband structures by MBE with very low defect density.

## IX. TYPE-II InAs/GaInSb DUAL-BAND DETECTORS

Recently, type-II InAs/GaInSb SLs have emerged as a third candidate for third-generation IR detectors.<sup>42,47–49,183</sup>

The highest quality two-color MWIR type-II SLS FPAs have been fabricated at the Fraunhofer Institute in Freiburg. The growth sequence starts with a 200 nm lattice matched AlGaAsSb buffer layer followed by a 700 nm thick *n*-type doped GaSb layer. Next, the “blue channel” consisting of 330 periods of *p*-type of a 7.5 ML InAs/10 ML GaSb is deposited. After the blue channel follows a common ground contact layer comprising 500 nm of *p*-type GaSb. The detection of the “red channel” is realized using 150 periods of a 9.5 ML InAs/10 ML GaSb SL. Finally, a 20 nm thick InAs terminates the structure. The thickness of the entire vertical pixel structure is only 4.5  $\mu\text{m}$ , which significantly reduces

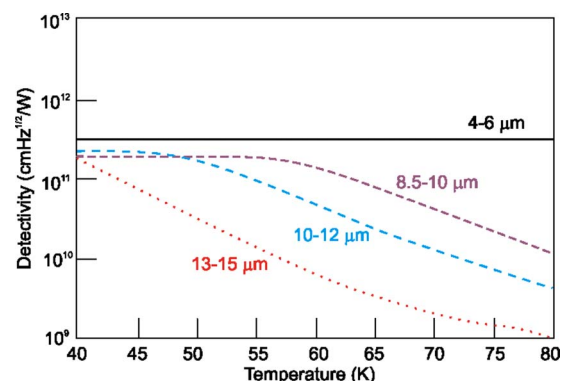


FIG. 60. (Color online) Detectivities of each spectral-band of the four-band QWIP FPA as a function of temperature. Detectivities were estimated using the single pixel test detector data taken at  $V_b = -1.5$  V and 300 K background with  $f/5$  optics (after Ref. 183).

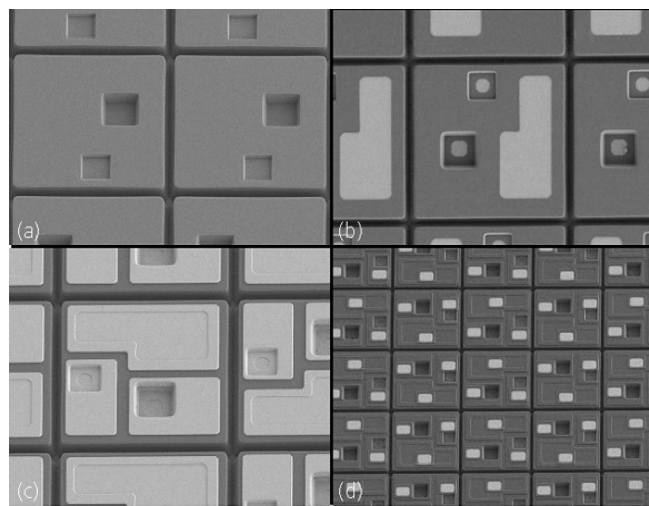


FIG. 61. SEM images illustrating the processing of  $288 \times 384$  dual-color InAs/GaSb SLS FPAs. At a pixel pitch of  $40\text{ }\mu\text{m}$ , three contact lands per pixel permit simultaneous and spatially coincident detection of both colors (after Ref. 42).

the technological challenge in comparison to dual-band HgCdTe FPAs with a typical total layer thickness around  $15\text{ }\mu\text{m}$ . For *n*-type and *p*-type doping of the SL regions and the contact layers Si, GaTe, and Be are used, respectively.

The first dual-band  $288 \times 384$  MWIR InAs/GaSb camera has already been demonstrated.<sup>42</sup> Figure 61 illustrates the device processing. In the first step via holes to the common *p*-type contact layer and to the *n*-type contact layer of the lower diode are etched by chlorine-based chemically assisted ion beam etching. Next, another chemical etching is used to fabricate deep trenches for complete electrical isolation of each pixel [see Fig. 61(a)]. After deposition of the diode passivation, a reactive ion etching is employed to selectively open the passivation to provide access to the contact layers [see Fig. 61(b)]. Next, the contact metallization is evaporated [see Fig. 61(c)]. A fully processed dual-color FPA is shown in Fig. 61(d).

In the above approach, simultaneous detection in a  $40\text{ }\mu\text{m}$  pixel has been achieved. Solid lines in Fig. 62 show normalized photocurrent spectra of both channels at 77 K and zero bias. With *f*/2 optics, 2.8 ms integration time, and 73 K detector temperature, the SL camera achieves NEDTs

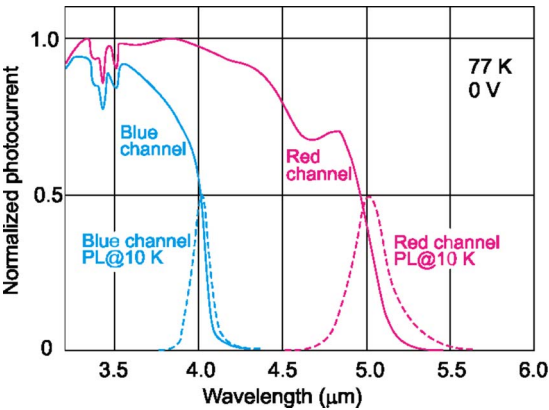


FIG. 62. (Color online) Normalized photocurrent at 77 K and the photoluminescence signal at 10 K vs wavelength (after Ref. 42).

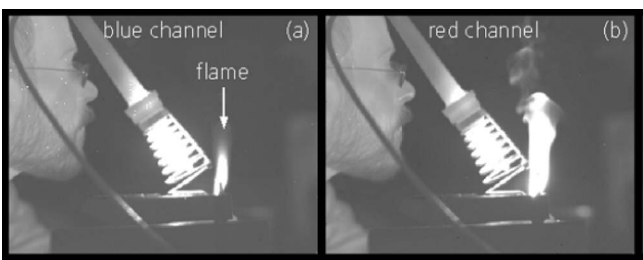


FIG. 63. Imagers delivered by the  $288 \times 384$  dual-color InAs/GaSb SLS camera (after Ref. 42).

TABLE X. Key characteristics of the  $384 \times 288$  dual-color SL IR-module (after Ref. 184).

Technology	Antimonide-type II SL, CMOC MUX
Spectral bands	Blue band: $3.4\text{--}4.0\text{ }\mu\text{m}$ Red band: $4.0\text{--}5.0\text{ }\mu\text{m}$ with temporal coincident integration in both spectral bands
Elements	$388 \times 284 \times 2$ ; $40\text{ }\mu\text{m}$ pitch
Element size	$38\text{ }\mu\text{m}$
Fill factor	$>80\%$ for both spectral bands
Biassing	Individually for both bands
Integration capacity for $3\text{--}4\text{ }\mu\text{m}$ (in Mio $e^-$ )	1,2/6 (two gain stages) $\pm 10\%$
Integration capacity for $4\text{--}5\text{ }\mu\text{m}$ (in Mio $e^-$ )	7/19 (two gain stages) $\pm 10\%$
Operability of elements	$>98\%$
Readout modes	Snapshot, stare then scan, temporal coincidence of signal in both bands
Read put models	Snapshot, stare then scan, temporal signal coincidence in both bands
Subframes	Arbitrary in steps of 8
Outputs	Four analog outputs for each color
Data rate digital	80 MHz serial high speed link interface
Full frame rate	150 Hz at $t_{\text{int}}=2\text{ ms}$
Environmental temperature range	$-54\text{ to }+71\text{ }^\circ\text{C}$
Vibration	MIL-STD-810F
IDCA	1–1.5 W linear split Stirling cooler or 0.7 W integral Stirling cooler
Weight of IDCA incl. electronics	$>2.5\text{ kg}$ for split linear Stirling cooler approximately 1 kg with integral cooler

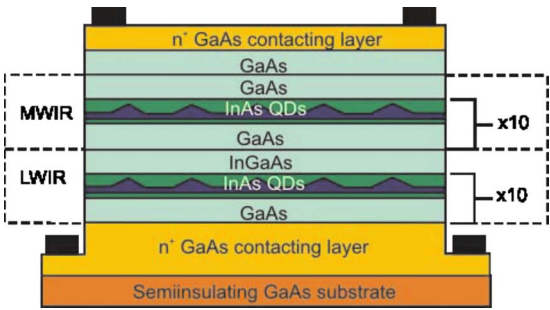


FIG. 64. (Color online) Schematic structure of the multispectral QDIP device (after Ref. 185).

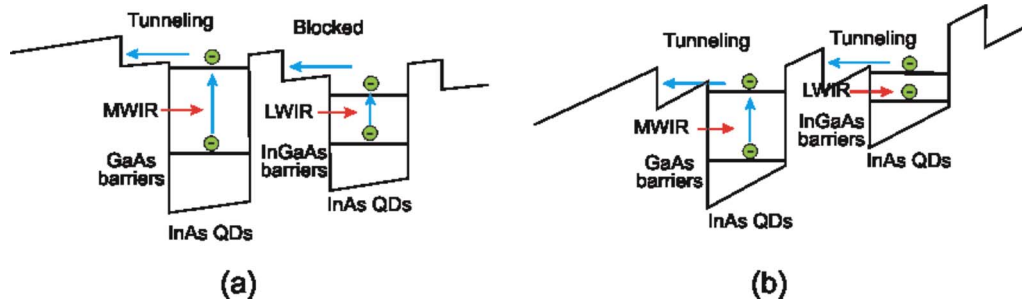


FIG. 65. (Color online) Simplified band diagram of the structure shown in Fig. 64 at different bias levels (after Ref. 185).

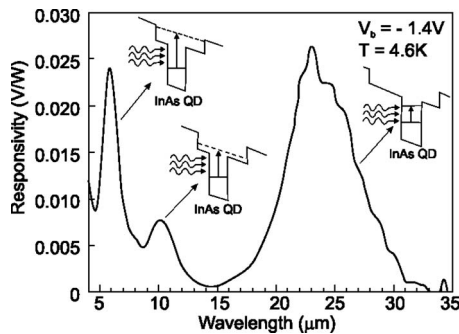


FIG. 66. Multicolor response from an InAs/In<sub>0.15</sub>Ga<sub>0.85</sub>As/GaAs DWELL detector. The MWIR (LWIR) peak is possibly a transition from a state in the dot to a higher (lower) lying state in the well, whereas the VLWIR response is possibly from two quantum-confined levels within the QD. This response is visible until 80 K (after Ref. 123).

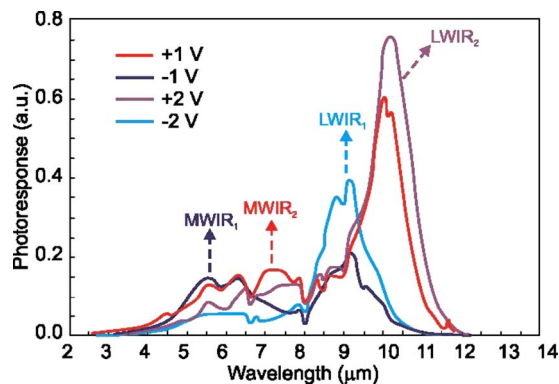


FIG. 67. (Color online) Spectral response from a DWELL detector with response at  $V_b = \pm 1$  V and  $\pm 2$  V. Note that the response in the two MWIR and LWIR bands can be measured using this detector. The relative intensities of the bands can be altered by the applied bias (after Ref. 55).

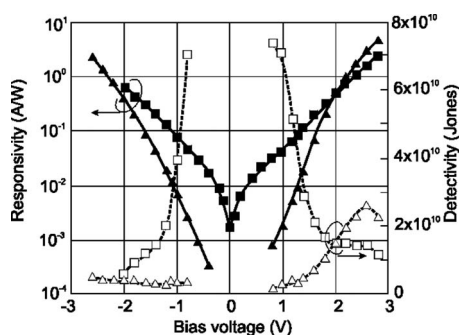
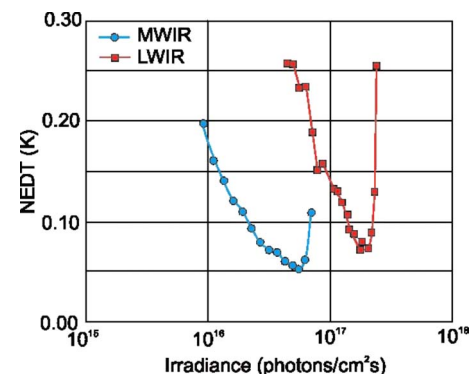


FIG. 68. Peak responsivity for a 15 stack DWELL detector at 78 K obtained using a calibrated blackbody source. Solid squares: MWIR responsivity; solid triangles: LWIR responsivity; open square: MWIR detectivity; open triangles: LWIR detectivity (after Ref. 52).



of 29.5 mK for the blue channel ( $3.4 \mu\text{m} \leq \lambda \leq 4.1 \mu\text{m}$ ) and 16.5 mK for the red channel ( $4.1 \mu\text{m} \leq \lambda \leq 5.1 \mu\text{m}$ ). As an example, the excellent imagery delivered by the  $288 \times 384$  InAs/GaSb dual-color camera is presented in Fig. 63. The image consists of a man, a hot soldering iron, and the burning flame of a cigarette lighter producing carbon dioxide. It is clearly evident that the carbon dioxide surrounding the burning gas flame only emits in the red channel. Table X overviews the figure of merit of the  $384 \times 288$  dual-color system.

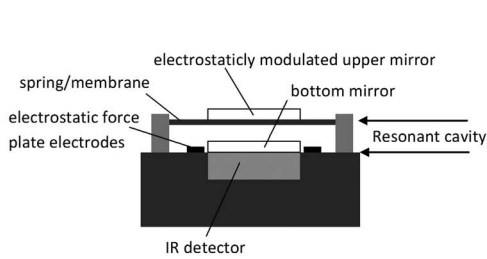
As one of the first representatives of a third-generation system, the dual-color SLS technology will be commercialized in a missile approach warning system. A square design of  $256 \times 256$  FPA with a reduced pitch of  $30 \times 30 \mu\text{m}^2$  is currently in development.<sup>184</sup> The reduction in pixel size can be achieved by using only two indium bumps per pixel. These very promising results confirm that the antimonide SL technology is now a direct competitor to MBE HgCdTe dual-color technology.

## X. MULTIBAND QDIPS

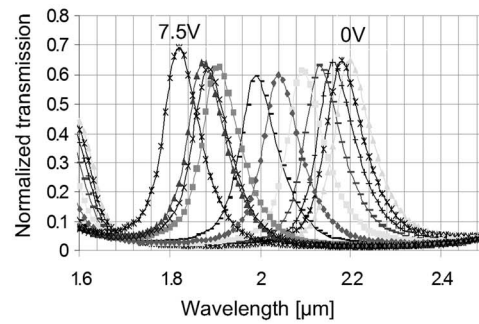
QDIP devices capable of detecting several separate wavelengths can be fabricated by vertical stacking of the different QWIP layers during epitaxial growth. The schematic structure is shown in Fig. 64. In the case of the structure described by Lu *et al.*<sup>185</sup> each QDIP absorption band consists of ten periods of InAs/InGaAs QD layers sandwiched between the top and bottom electrodes. Next figure shows the simplified band diagram of this structure at different bias levels. As Fig. 65 presents, the bias voltage selection

FIG. 69. (Color online) NEDT in the MWIR and LWIR bands at 77 K. Irradiance levels for MWIR and LWIR are  $3\text{--}5 \mu\text{m}$  ( $f/2$ ) and  $8\text{--}12 \mu\text{m}$  ( $f/2.3$ ), respectively (after Ref. 54).





(a)



(b)

FIG. 70. Measured optical transmission of a Fabry-Pérot tunable filter fabricated on an HgCdTe photoconductor. Applied filter drive voltages range from 0 to 7.5 V of a Fabry-Pérot filter formed on a detector (after Ref. 189).

of detection bands originates from the asymmetric band structure. At low bias voltage, the high energy GaAs barrier blocks the photocurrent generated by LWIR radiation and only a response to the MWIR incidence is detected. On the contrary, as the bias voltage increases, the barrier energy decreases, allowing LWIR signals to be detected at different bias voltage levels.

The first two-color QD FPA demonstration was based on a voltage-tunable InAs/InGaAs/GaAs DWELL structure.<sup>52,53</sup> As was described in Sec. VID 1, in this type of structure, InAs QDs are placed in an InGaAs well, which in turn is placed in a GaAs matrix (see Fig. 35).

Figure 66 shows the multicolor response from a DWELL detector. This device has demonstrated multicolor response ranging from the MWIR (3–5  $\mu\text{m}$ ) based on a bound-to-continuum transition to the LWIR (8–12  $\mu\text{m}$ ), which is based on a bound state in the dot to a bound state in the well. A very long-wavelength response (VLWIR) has also been observed and has been attributed to transitions between two bound states in the QDs, since the calculated energy spacing between the dot levels is about 50–60 meV. Moreover, by adjusting the voltage bias of the device, it is possible to modify the ratio of electrons promoted by MWIR, LWIR, and VLWIR absorptions. Typically; the MWIR response dominates at low to nominal voltages due to higher escape probability. With increasing voltage, the LWIR and eventually VLWIR responses are enhanced due to the increased tunneling probability of lower states in the DWELL detector (see Fig. 67). The bias-dependent shift of the spectral response is observed due to quantum-confined Stark effect. This voltage-control of spectral response can be exploited to

realize spectrally smart sensors whose wavelength and bandwidth can be tuned depending on the desired application.<sup>52,186,187</sup>

Typically, the detector structure consists of a 15-stack asymmetric DWELL structure sandwiched between two highly doped  $n$ -GaAs contact layers. The DWELL region consists of a 2.2 ML of  $n$ -doped InAs QDs in an  $\text{In}_{0.15}\text{Ga}_{0.85}\text{As}$  well, itself placed within a GaAs matrix. By varying the width of the bottom InGaAs well from 10 to 60 Å, the operating wavelength of the detector can be changed from 7.2 to 11  $\mu\text{m}$ . The responsivity and detectivity obtained from the test devices at 78 K are shown in Fig. 68. The measured detectivities were  $2.6 \times 10^{10} \text{ cm Hz}^{1/2}/\text{W}$  ( $V_b = 2.6 \text{ V}$ ) for the LWIR band and  $7.1 \times 10^{10} \text{ cm Hz}^{1/2}/\text{W}$  ( $V_b = 1 \text{ V}$ ) for the MWIR band.

Recently, Varley *et al.*<sup>54</sup> demonstrated a two-color, MWIR/LWIR,  $320 \times 256$  FPA based on DWELL detectors. Minimum NEDT values of 55 mK (MWIR) and 70 mK (LWIR) were measured (see Fig. 69).

## XI. ADAPTIVE FPAS

Research beyond third-generation detector arrays is focused on adaptive multi/hyperspectral imaging. Although not considered as a candidate for third-generation FPAs, and hence not discussed in this review, it is worth mentioning that a number of recent developments in the area of micro-electromechanical system (MEMS)-based tunable IR detectors have the potential to deliver voltage-tunable multiband IR FPAs. These technologies have been developed as part of

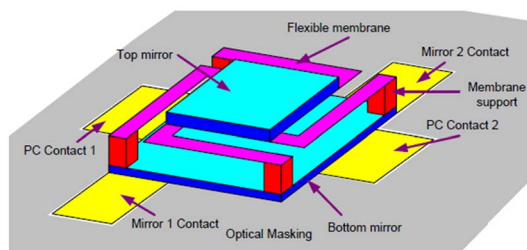


FIG. 71. (Color online) General concept of MEMS-based tunable IR detector. The detector is located totally under the bottom mirror.

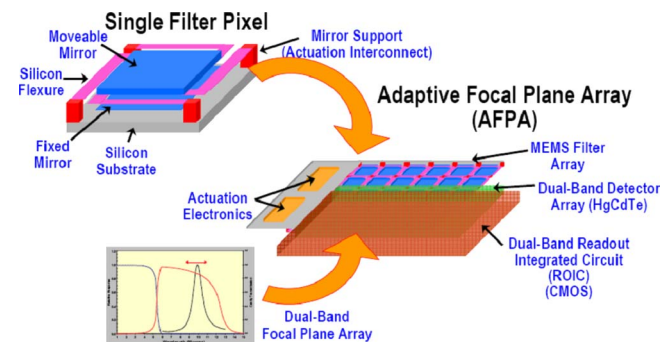


FIG. 72. (Color online) Dual band adaptive FPA (after Ref. 188).

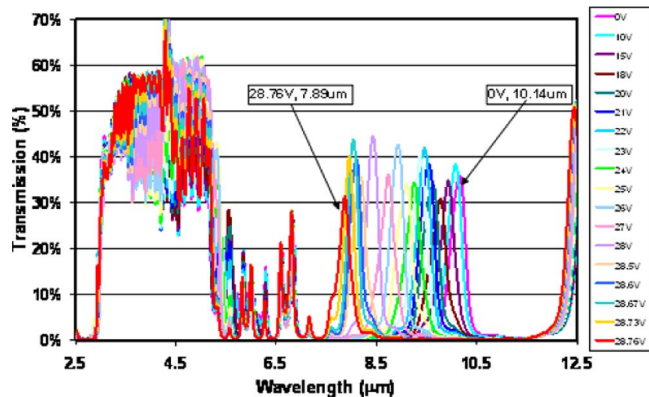


FIG. 73. (Color online) Measured room temperature spectral transmission of a MEMS tunable filter over a range of actuation voltages demonstrating tuning in the LWIR with broadband transmission in the MWIR (after Ref. 188).

the DARPA-funded adaptive FPA (AFPA) program and have demonstrated multispectral tunable IR detector structures.<sup>22,188–191</sup>

By use of MEMS fabrication techniques arrays of devices, such as etalons, can be fabricated on an IR detector array that permits tuning of the incident radiation on the detector. If the etalons can be programmed to change distance from the detector surface by the order of IR wavelengths, the detector responds to all wavelengths in a waveband sequentially. For example, Fig. 70(b) shows the room temperature spectral response data of the monolithic filter on a HgCdTe photoconductive detector, with released spacer layer to form an air cavity as shown in Fig. 70(a). The corresponding mirror displacement, at bias voltages in the range from 0 to 7.5 V, is 1.2–0.7  $\mu\text{m}$  and the peak spectral response shifts from 2.2–1.85  $\mu\text{m}$ . At the center wavelength of  $\sim 1950$  nm, the FWHM is  $\sim 100$  nm.

The integration of various component technologies into a AFPA involves a complex interplay across a broad range of disciplines, involving MEMS device processing, optical coating technology, microlenses, optical system modeling, and FPA devices. The goal of this integration is to produce an image-sensor array in which the wavelength sensitivity of each pixel can be independently tuned. In effect, the device would constitute a large-format array of electronically programmable microspectrometers.

Figure 71 presents the general concept of a MEMS-based tunable IR detector. The MEMS filters are individual electrostatically actuated Fabry–Pérot tunable filters. In the actual implementation, the MEMS filter array is mounted so that the filters are facing toward the detector to minimize spectral cross-talk.

Rockwell Scientific Co. has demonstrated simultaneous spectral tuning in the LWIR region while providing broadband imagery in MWIR band using dual band AFPA (see Fig. 72). The filter characteristics, including LWIR passband bandwidth and tuning range, are determined by the integral thin film reflector and AR coatings. The nominal dimension of each MEMS filter is between 100 and 200  $\mu\text{m}$  on a side and each filter covers a small subarray of the detector pixels. Employing dual-band FPA with 20  $\mu\text{m}$  pixel pitch results in

each MEMS filter covering a detector subarray ranging from  $5 \times 5$  to  $10 \times 10$  pixels. The MEMS filter array will then evolve to tunable individual pixels. The device will undoubtedly require a new ROIC to accommodate the additional control functions at each pixel.

Figure 73 shows the room temperature spectral transmission of a filter in dual-band AFPA illustrating filter tuning for various actuation voltages. The LWIR passbands exhibit low transmission and have measured bandwidths of 200–300 nm.

The realization of the AFPA concepts offers the potential for dramatic improvements in critical military missions involving reconnaissance, battlefield surveillance, and precision targeting.<sup>191</sup>

## XII. CONCLUSIONS

Future applications of FPAs for IR imaging systems require (i) higher pixel sensitivity; (ii) further increase in pixel density to above  $10^6$  pixels; (iii) cost reduction in IR imaging array systems as a result of reduced cooling requirements for the sensor technology, combined with integration of detectors and signal-processing functions, with much more on-chip signal processing; and (iv) improvements in functionality of IR imaging arrays through development of multispectral sensors.

Multicolor long-wavelength detector technology will be the emerging standard for future space and ground-based applications. For many systems, such as night-vision goggles, the IR image is viewed by the human eye, which can discern resolution improvements only up to about 1 megapixel, roughly the same resolution as high-definition television. Most high-volume applications can be completely satisfied with a format of  $1280 \times 1024$ . Although wide-area surveillance and astronomy applications could make use of larger formats, funding limits may prevent the exponential growth that has been seen in past decades.

Multicolor IR imagers are beginning a challenging road to deployment. For multiband sensors, boosting the sensitivity in order to maximize the identification range of threats and targets is the primary objective.

It is predicted that HgCdTe technology will continue in the near future to expand the envelope of its capabilities because of its excellent optoelectronic properties. Despite serious competition from alternative technologies and slower progress than expected, HgCdTe is unlikely to be seriously challenged for high-performance applications, especially those requiring multispectral capability and fast response. However, nonuniformity is a serious problem in the case of LWIR and VLWIR HgCdTe detectors. For applications that require operation in the LWIR band as well as two-color LWIR/VLWIR bands, it is likely that HgCdTe will not be the optimal solution.

In a two color sequential mode, one can make use of the existing single-color readout circuitry. However, for simultaneous mode of operations, new readout circuitry designs are needed with different integration charge capacities for separate spectral bands of interest. For long-wavelength multi-

color operation the integrating charge capacity is the major issue versus different flux levels as in the case of MWIR/LWIR two-color operation.

State-of-the-art QWIP and HgCdTe FPAs provide similar performance figures of merit, since they are predominantly limited by the readout circuit. The very short integration time of LWIR HgCdTe devices of typically below 300  $\mu$ s is very useful to freeze a scene with rapidly moving objects. For QWIP devices, however, the integration time must be 10–100 times longer and is typically in the range of 5–20 ms.

Recently, type-II InAs/GaInSb SLs and QDIPs have emerged as the next two candidates for third-generation IR detectors. The type-II InAs/GaInSb SL structure has great potential for LWIR/VLWIR spectral ranges, with performance comparable to HgCdTe for the same cutoff wavelength. Based on recent breakthroughs in Sb-based type-II SLS technology, it is evident that this material system is in a position to provide high thermal resolution for short integration times, that are comparable to HgCdTe. The fact that Sb-based SLs are processed using relatively standard III-V technology raises the potential for this technology to be more competitive than HgCdTe due to lower production costs in volume production.

QDIP detector technology is still at a very early stage of development. The bias-dependent spectral response of this type of detector can be exploited to realize spectrally smart sensors whose wavelength and bandwidth can be tuned depending on the desired application. Optimization of the QDIP architecture is still at an early stage of development.

Although in an early stage of development, the potential to deliver FPAs that can adapt their spectral response (Adaptive FPA:AFPA) to match the sensor requirements in real time presents a compelling case for future multispectral IR imaging systems. Such systems have the potential to deliver much-improved threat and target recognition capabilities for future defense combat systems.

### XIII. NOMENCLATURE

$a$  lattice constant  
 $A$  detector area  
 AFPA adaptive focal plane array  
 CCD charge-coupled device  
 CMOS complementary MOS  
 $D^*$  detectivity  
 DLHJ double-layer heterojunction  
 DWELL dot in a well  
 ECR electron cyclotron resonance  
 $E_g$  energy gap  
 $f/\#$   $f$  number (ratio of area to focal length of optics)  
 FOV field of view  
 FPA focal plane array  
 $g$  photoelectrical gain  
 $h$  Planck's constant  
 HDVIP high-density vertically integrated photodiode  
 ICP inductively coupled plasma  
 IR infrared

$k$  Boltzmann's constant  
 $l$  length  
 LO longitudinal phonon  
 LPE liquid phase epitaxy  
 LWIR long-wavelength infrared  
 $m$  free electron mass  
 $m^*$  effective mass  
 MBE molecular beam epitaxy  
 MEMS microelectromechanical systems  
 MIS metal-insulator-semiconductor  
 ML monolayer  
 MOCVD metal organic chemical vapor deposition  
 MOS metal-oxide semiconductor  
 MOSFET metal oxide semiconductor field effect transistor  
 MQW multiquantum well  
 MWIR medium-wavelength infrared  
 MTF modulation transfer function  
 $n$  electron concentration  
 $n_i$  intrinsic carrier concentration  
 $n_r$  refraction coefficient  
 $N_a$  acceptor concentration  
 $N_d$  donor concentration  
 NEDT noise equivalent temperature difference  
 $p$  hole concentration  
 $q$  electron charge  
 QD quantum dot  
 QDIP quantum dot IR photodetectors  
 QW quantum well  
 QWIP quantum-well IR photodetectors  
 $R_d$  incremental detector resistance  
 $R_o$  zero bias detector resistance  
 ROIC readout integrated circuit  
 SCA sensor chip assembly  
 SL superlattice  
 SLS strained-layer superlattice  
 SWIR short-wavelength infrared  
 $t$  thickness  
 $T$  temperature  
 TEC thermal expansion coefficient  
 TDI time delay and integration  
 TDMI time division multiplexed integration  
 TLHJ triple-layer heterojunction  
 UV ultraviolet  
 VIP vertically integrated photodiode  
 VISA vertically integrated sensor array  
 VLWIR very long-wavelength infrared  
 1D one dimensional  
 2D two dimensional  
 3D three dimensional  
 $\alpha$  absorption coefficient  
 $\epsilon_s$  static dielectric constant  
 $\epsilon_\infty$  optical dielectric constant  
 $\lambda$  wavelength  
 $\lambda_c$  cutoff wavelength  
 $\eta$  quantum efficiency  
 $\nu$  radiation frequency  
 $\mu_e$  electron mobility  
 $\mu_h$  hole mobility



$\tau$  carrier lifetime  
 $\tau_A$  Auger lifetime  
 $\tau_R$  radiative lifetime  
 $\Phi_B$  photon flux density  
 $\Delta f$  bandwidth  
 $\Delta x$  compositional uniformity  
 $x$  mole composition (composition)

## ACKNOWLEDGMENTS

The authors would like to express their gratitude to Gladden Visiting Senior Fellowships for financial support of this work. This paper has also been done under financial support of the Polish Ministry of Sciences and Higher Education, Key Project POIG.01.03.01-14-016/08 "New Photonic Materials and their Advanced Application."

- <sup>1</sup>P. Norton, J. Campbell, S. Horn, and D. Reago, *Proc. SPIE* **4130**, 226 (2000).
- <sup>2</sup>M. Z. Tidrow, W. A. Beck, W. W. Clark, H. K. Pollehn, J. W. Little, N. K. Dhar, P. R. Leavitt, S. W. Kennedy, D. W. Beekman, A. C. Goldberg, and W. R. Dyer, *Opto-Electron. Rev.* **7**, 283 (1999).
- <sup>3</sup>M. N. Abedin, T. F. Refaat, I. Bhat, Y. Xiao, S. Bandara, and S. D. Gunapala, *Proc. SPIE* **5543**, 239 (2004).
- <sup>4</sup>P. McCarley, *Proc. SPIE* **4288**, 1 (2001).
- <sup>5</sup>J. T. Caulfield, *Proceedings of the 32nd Applied Imagery Pattern Recognition Workshop*, (IEEE, New York, 2003).
- <sup>6</sup>R. A. Smith, F. E. Jones, and R. P. Chasmar, *The Detection and Measurement of Infrared Radiation* (Clarendon, Oxford, 1958).
- <sup>7</sup>P. W. Kruse, L. D. McGlauchlin, and R. B. McQuistan, *Elements of Infrared Technology* (Wiley, New York, 1962).
- <sup>8</sup>E. S. Barr, *Am. J. Phys.* **28**, 42 (1960).
- <sup>9</sup>[http://coolcosmos.ipac.caltech.edu/cosmic\\_classroom/timeline/timeline\\_onepage.html](http://coolcosmos.ipac.caltech.edu/cosmic_classroom/timeline/timeline_onepage.html).
- <sup>10</sup>H. J. Walker, *Astron. Geophys.* **41**, 10 (2000).
- <sup>11</sup>T. W. Case, *Phys. Rev.* **9**, 305 (1917).
- <sup>12</sup>R. J. Cashman, *Proc. IRE* **47**, 1471 (1959).
- <sup>13</sup>P. R. Norton, *Proc. SPIE* **3698**, 652 (1999).
- <sup>14</sup>A. Rogalski, *Infrared Detectors* (Gordon and Breach, Amsterdam, 2000).
- <sup>15</sup>R. Thorn, U.S. Patent No. 4,039,833 (August 17, 1977).
- <sup>16</sup>I. M. Baker and R. A. Ballingall, *Proc. SPIE* **510**, 121 (1984).
- <sup>17</sup>P. Norton, in *Encyclopedia of Optical Engineering*, edited by R. Driggers (Dekker, New York, 2003), pp. 320–348.
- <sup>18</sup>A. Hoffman, *Laser Focus World*, **42**, 81 (2006).
- <sup>19</sup>A. W. Hoffman, P. L. Love, and J. P. Rosbeck, *Proc. SPIE* **5167**, 194 (2004).
- <sup>20</sup>M. D. Morris, *Microscopic and Spectroscopic Imaging of the Chemical State* (Dekker, New York, 1993).
- <sup>21</sup>C. D. Tran, *Anal. Lett.* **38**, 735 (2005).
- <sup>22</sup>W. J. Gunning, J. DeNatale, P. Stupar, R. Borwick, R. Dannenberg, R. Sczupak, and P. O. Pettersson, *Proc. SPIE* **5783**, 336 (2005).
- <sup>23</sup>D. Reago, S. Horn, J. Campbell, and R. Vollmerhausen, *Proc. SPIE* **3701**, 108 (1999).
- <sup>24</sup>L. J. Kozlowski and W. F. Kosonocky, in *Handbook of Optics*, edited by M. Bass, E. W. Van Stryland, D. R. Williams, and W. L. Wolfe (McGraw-Hill, New York, 1995), Chap. 23.
- <sup>25</sup>S. Horn, P. Norton, K. Carson, R. Eden, and R. Clement, *Proc. SPIE* **5406**, 332 (2004).
- <sup>26</sup>R. Balcerak and S. Horn, *Proc. SPIE* **5783**, 384 (2005).
- <sup>27</sup>P. R. Norton, *Opto-Electron. Rev.* **14**, 283 (2006).
- <sup>28</sup>S. D. Gunapala, S. V. Bandara, J. K. Liu, J. M. Mumolo, C. J. Hill, D. Z. Ting, E. Kurth, J. Woolaway, P. D. LeVan, and M. Z. Tidrow, *Proc. SPIE* **6660**, 66600E (2007).
- <sup>29</sup>[http://www.teledyne-si.com/infrared\\_visible\\_fps/index.html](http://www.teledyne-si.com/infrared_visible_fps/index.html).
- <sup>30</sup>E. P. G. Smith, G. M. Venzor, Y. Petraitis, M. V. Liguori, A. R. Levy, C. K. Rabkin, J. M. Peterson, M. Reddy, S. M. Johnson, and J. W. Bangs, *J. Electron. Mater.* **36**, 1045 (2007).
- <sup>31</sup>G. Destefanis, J. Baylet, P. Ballet, P. Castelein, F. Rothan, O. Gravrand, J. Rothman, J.P. Chamonal, and A. Million, *J. Electron. Mater.* **36**, 1031 (2007).
- <sup>32</sup>G. Sarusi, *Infrared Phys. Technol.* **44**, 439 (2003).
- <sup>33</sup>S. Horn, P. Norton, T. Cincotta, A. Stolz, D. Benson, P. Perconti, and J. Campbell, *Proc. SPIE* **5074**, 44 (2003).
- <sup>34</sup>A. Rogalski, *Rep. Prog. Phys.* **68**, 2267 (2005).
- <sup>35</sup>P. D. Dreiske, *Proc. SPIE* **5783**, 325 (2005).
- <sup>36</sup>D. F. King, W. A. Radford, E. A. Patten, R. W. Graham, T. F. McEwan, J. G. Vodicka, R. F. Bornfreund, P. M. Goetz, G. M. Venzor, and S. M. Johnson, *Proc. SPIE* **6206**, 62060W (2006).
- <sup>37</sup>G. Destefanis, P. Ballet, J. Baylet, P. Castelein, O. Gravrand, J. Rothman, F. Rothan, G. Perrais, J. P. Chamonal, A. Million, P. Tribollet, B. Terrier, E. Sanson, P. Costa, and L. Vial, *Proc. SPIE* **6206**, 62060R (2006).
- <sup>38</sup>N. T. Gordon, P. Abbott, J. Giess, A. Graham, J. E. Hails, D. J. Hall, L. Hipwood, C. L. Lones, C. D. Maxeh, and J. Price, *J. Electron. Mater.* **36**, 931 (2007).
- <sup>39</sup>S. D. Gunapala and S. V. Bandara, in *Handbook of Infrared Detection Technologies*, edited by M. Henini and M. Razeghi (Elsevier, Oxford, 2002), pp. 83–119.
- <sup>40</sup>A. Rogalski, *J. Appl. Phys.* **93**, 4355 (2003).
- <sup>41</sup>A. Manissadjian, D. Gohier, E. Costard, and A. Nedelcu, *Proc. SPIE* **6206**, 62060E (2006).
- <sup>42</sup>M. Münzberg, R. Breiter, W. Cabanski, H. Lutz, J. Wendler, J. Ziegler, R. Rehm, and M. Walther, *Proc. SPIE* **6206**, 620627 (2006).
- <sup>43</sup>S. D. Gunapala, S. V. Bandara, J. K. Liu, J. M. Mumolo, C. J. Hill, S. B. Rafol, D. Salazar, J. Woolaway, P. D. LeVan, and M. Z. Tidrow, *Infrared Phys. Technol.* **50**, 217 (2007).
- <sup>44</sup>A. Nedelcu, E. Costard, P. Bois, and X. Marcadet, *Infrared Phys. Technol.* **50**, 227 (2007).
- <sup>45</sup>A. Rogalski, *Opt. Eng.* **42**, 3498 (2003).
- <sup>46</sup>R. Rehm, M. Walther, J. Schmitz, J. Fleißner, F. Fuchs, J. Ziegler, and W. Cabanski, *Opto-Electron. Rev.* **14**, 19 (2006).
- <sup>47</sup>A. Rogalski and P. Martyniuk, *Infrared Phys. Technol.* **48**, 39 (2006).
- <sup>48</sup>R. Rehm, M. Walther, J. Schmitz, J. Fleißner, J. Ziegler, W. Cabanski, and R. Breiter, *Proc. SPIE* **6294**, 629404 (2006).
- <sup>49</sup>A. Rogalski, *Opto-Electron. Rev.* **14**, 87 (2006).
- <sup>50</sup>S. M. Kim and J. S. Harris, *IEEE Photonics Technol. Lett.* **16**, 2538 (2004).
- <sup>51</sup>S. Chakrabarti, X. H. Su, P. Bhattacharya, G. Ariyawansa, and A. G. U. Perera, *IEEE Photonics Technol. Lett.* **17**, 178 (2005).
- <sup>52</sup>S. Krishna, D. Forman, S. Annamalai, P. Dowd, P. Varangis, T. Tumolillo, A. Gray, J. Zilko, K. Sun, M. Liu, J. Campbell, and D. Carothers, *Appl. Phys. Lett.* **86**, 193501 (2005).
- <sup>53</sup>S. Krishna, D. Forman, S. Annamalai, P. Dowd, P. Varangis, T. Tumolillo, A. Gray, J. Zilko, K. Sun, M. Liu, J. Campbell, and D. Carothers, *Phys. Status Solidi C* **3**, 439 (2006).
- <sup>54</sup>E. Varley, M. Lenz, S. J. Lee, J. S. Brown, D. A. Ramirez, A. Stintz, and S. Krishna, *Appl. Phys. Lett.* **91**, 081120 (2007).
- <sup>55</sup>S. Krishna, S. D. Gunapala, S. V. Bandara, C. Hill, and D. Z. Ting, *Proc. IEEE* **95**, 1838 (2007).
- <sup>56</sup>M. B. Reine, in *Encyclopedia of Modern Optics*, edited by R. D. Guenther, D. G. Steel, and L. Bayvel (Elsevier, Oxford, 2004), pp. 392–402.
- <sup>57</sup>P. Norton, *Opto-Electron. Rev.* **10**, 159 (2002).
- <sup>58</sup>J. M. Peterson, J. A. Franklin, M. Readdy, S. M. Johnson, E. Smith, W. A. Radford, and I. Kasai, *J. Electron. Mater.* **35**, 1283 (2006).
- <sup>59</sup>R. Bornfreund, J. P. Rosbeck, Y. N. Thai, E. P. Smith, D. D. Lofgreen, M. F. Vilela, A. A. Buell, M. D. Newton, K. Kosai, S. M. Johnson, T. J. DeLyon, J. J. Jensen, and M. Z. Tidrow, *J. Electron. Mater.* **36**, 1085 (2007).
- <sup>60</sup>M. Rodot, C. Verie, Y. Marfaing, J. Besson, and H. Lebloch, *IEEE J. Quantum Electron.* **2**, 586 (1966).
- <sup>61</sup>M. A. Kinch, *Proc. SPIE* **4369**, 566 (2001).
- <sup>62</sup>I. M. Baker and R. A. Ballingall, *Proc. SPIE* **510**, 121 (1984).
- <sup>63</sup>I. M. Baker, G. J. Crimes, J. E. Parsons, and E. S. O'Keefe, *Proc. SPIE* **2269**, 636 (1994).
- <sup>64</sup>J. M. Arias, J. G. Pasko, M. Zandian, S. H. Shin, G. M. Williams, L. O. Bubulac, R. E. DeWames, and W. E. Tennant, *J. Electron. Mater.* **22**, 1049 (1993).
- <sup>65</sup>Y. Nemirovsky and G. Bahir, *J. Vac. Sci. Technol. A* **7**, 450 (1989).
- <sup>66</sup>Y. Nemirovsky, N. Mainzer, and E. Weiss, in *Properties of Narrow Gap Cadmium-Based Compounds*, EMIS Datareviews Series No. 10, edited by P. P. Amer (IEE, London, 1994), pp. 284–290.
- <sup>67</sup>J. F. Ameurlaire and G. D. Cohen-Solal, U.S. Patent No. 3,845,494 (October 29, 1974).
- <sup>68</sup>G. D. Cohen-Solal and A. G. Lussereau, U.S. Patent No. 3,988,774 (October 26, 1976).
- <sup>69</sup>T. Chuh, *Proc. SPIE* **5563**, 19 (2004).

- <sup>70</sup>J. Bajaj, G. Sullivan, D. Lee, E. Aifer, and M. Razeghi, *Proc. SPIE* **6542**, 65420B (2007).
- <sup>71</sup>H. Lim, S. Tsao, W. Zhang, and M. Razeghi, *Appl. Phys. Lett.* **90**, 131112 (2007).
- <sup>72</sup>J. Jiang, S. Tsao, T. O'Sullivan, W. Zhang, H. Lim, T. Sills, K. Mi, M. Razeghi, G. J. Brown, and M. Z. Tidrow, *Appl. Phys. Lett.* **84**, 2166 (2004).
- <sup>73</sup>J. Szafraniec, S. Tsao, W. Zhang, H. Lim, M. Taguchi, A. A. Quivy, B. Movaghar, and M. Razeghi, *Appl. Phys. Lett.* **88**, 121102 (2006).
- <sup>74</sup>E.-T. Kim, A. Madhukar, Z. Ye, and J. C. Campbell, *Appl. Phys. Lett.* **84**, 3277 (2004).
- <sup>75</sup>S. D. Gunapala, S. V. Bandara, C. J. Hill, D. Z. Ting, J. K. Liu, B. Rafol, E. R. Blazejewski, J. M. Mumolo, S. A. Keo, S. Krishna, Y.-C. Chang, and C. A. Shott, *IEEE J. Quantum Electron.* **43**, 230 (2007).
- <sup>76</sup>S. Chakrabarti, X. H. Su, P. Bhattacharya, G. Ariyawansa, and A. G. U. Perera, *IEEE Photonics Technol. Lett.* **17**, 178 (2005).
- <sup>77</sup>R. S. Attaluri, S. Annamalai, K. T. Posani, A. Stintz, and S. Krishna, *J. Vac. Sci. Technol. B* **24**, 1553 (2006).
- <sup>78</sup>S. Chakrabarti, A. D. Stiff-Roberts, X. H. Su, P. Bhattacharya, G. Ariyawansa, and A. G. U. Perera, *J. Phys. D* **38**, 2135 (2005).
- <sup>79</sup>S. Krishna, D. Forman, S. Annamalai, P. Dowd, P. Varangis, T. Tumolillo, A. Gray, J. Zilko, K. Sun, M. Liu, J. Campbell, and D. Carothers, *Phys. Status Solidi C* **3**, 439 (2006).
- <sup>80</sup>B. F. Levine, *J. Appl. Phys.* **74**, R1 (1993).
- <sup>81</sup>S. D. Gunapala, S. V. Bandara, J. K. Liu, C. J. Hill, B. Rafol, J. M. Mumolo, J. T. Trinh, M. Z. Tidrow, and P. D. LeVan, *Semicond. Sci. Technol.* **20**, 473 (2005).
- <sup>82</sup>M. Jhabvala, K. K. Choi, C. Monroy, and A. La, *Infrared Phys. Technol.* **50**, 234 (2007).
- <sup>83</sup>S. D. Gunapala and S. V. Bandara, in *Handbook of Thin Devices*, edited by M. H. Francombe (Academic, San Diego, 2000), Vol. 2, pp. 63–99.
- <sup>84</sup>S. Gunapala, M. Sundaram, and S. Bandara, *Laser Focus World* **32**, 233 (1996).
- <sup>85</sup>C. J. Chen, K. K. Choi, M. Z. Tidrow, and D. C. Tsui, *Appl. Phys. Lett.* **68**, 1446 (1996).
- <sup>86</sup>C. J. Chen, K. K. Choi, W. H. Chang, and D. C. Tsui, *Appl. Phys. Lett.* **71**, 3045 (1997).
- <sup>87</sup>M. Z. Tidrow, J. C. Chiang, S. S. Li, and K. Bacher, *Appl. Phys. Lett.* **70**, 859 (1997).
- <sup>88</sup>A. Singh and M. O. Manasreh, *Proc. SPIE* **2397**, 193 (1995).
- <sup>89</sup>A. C. Goldberg, S. W. Kennerly, J. W. Little, H. K. Pollehn, T. A. Shafer, C. L. Mears, H. F. Schaake, M. Winn, M. Taylor, and P. N. Uppal, *Proc. SPIE* **4369**, 532 (2001).
- <sup>90</sup>H. Schneider, M. Walther, J. Fleissner, R. Rehm, E. Diwo, K. Schwarz, P. Koidl, G. Weimann, J. Ziegler, R. Breiter, and W. Cabanski, *Proc. SPIE* **4130**, 353 (2000).
- <sup>91</sup>H. Schneider, P. Koidl, M. Walther, J. Fleissner, R. Rehm, E. Diwo, K. Schwarz, and G. Weimann, *Infrared Phys. Technol.* **42**, 283 (2001).
- <sup>92</sup>M. Jhabvala, K. Choi, A. Goldberg, A. La, and S. Gunapala, *Proc. SPIE* **5167**, 175 (2004). 1 k × 1 k
- <sup>93</sup>S. D. Gunapala, S. V. Bandara, J. K. Liu, C. J. Hill, B. Rafol, J. M. Mumolo, J. T. Trinh, M. Z. Tidrow, and P. D. LeVan, *Semicond. Sci. Technol.* **20**, 473 (2005).
- <sup>94</sup>D. C. Arrington, J. E. Hubbs, M. E. Gramer, and G. A. Dole, *Proc. SPIE* **4028**, 289 (2000).
- <sup>95</sup>L. Bürkle and F. Fuchs, in *Handbook of Infrared Detection and Technologies*, edited by M. Henini and M. Razeghi (Elsevier, Oxford, 2002), pp. 159–189.
- <sup>96</sup>G. J. Brown, F. Szmulowicz, K. Mahalingam, S. Houston, Y. Wei, A. Gon, and M. Razeghi, *Proc. SPIE* **4999**, 457 (2003).
- <sup>97</sup>D. L. Smith and C. Mailhot, *J. Appl. Phys.* **62**, 2545 (1987).
- <sup>98</sup>C. Mailhot and D. L. Smith, *J. Vac. Sci. Technol. A* **7**, 445 (1989).
- <sup>99</sup>J. P. Omaggio, J. R. Meyer, R. J. Wagner, C. A. Hoffman, M. J. Yang, D. H. Chow, and R. H. Miles, *Appl. Phys. Lett.* **61**, 207 (1992).
- <sup>100</sup>C. A. Hoffman, J. R. Meyer, E. R. Youngdale, F. J. Bartoli, R. H. Miles, and L. R. Ram-Mohan, *Solid-State Electron.* **37**, 1203 (1994).
- <sup>101</sup>C. H. Grein, P. M. Young, and H. Ehrenreich, *Appl. Phys. Lett.* **61**, 2905 (1992).
- <sup>102</sup>C. H. Grein, P. M. Young, M. E. Flatté, and H. Ehrenreich, *J. Appl. Phys.* **78**, 7143 (1995).
- <sup>103</sup>E. R. Youngdale, J. R. Meyer, C. A. Hoffman, F. J. Bartoli, C. H. Grein, P. M. Young, H. Ehrenreich, R. H. Miles, and D. H. Chow, *Appl. Phys. Lett.* **64**, 3160 (1994).
- <sup>104</sup>O. K. Yang, C. Pfahler, J. Schmitz, W. Pletschen, and F. Fuchs, *Proc. SPIE* **4999**, 448 (2003).
- <sup>105</sup>J. L. Johnson, *Proc. SPIE* **3948**, 118 (2000).
- <sup>106</sup>G. J. Brown, *Proc. SPIE* **5783**, 65 (2005).
- <sup>107</sup>M. Razeghi, Y. Wei, A. Gin, A. Hood, V. Yazdanpanah, M. Z. Tidrow, and V. Nathan, *Proc. SPIE* **5783**, 86 (2005).
- <sup>108</sup>R. Rehm, M. Walther, J. Schmitz, J. Fleißner, F. Fuchs, W. Cabanski, and J. Ziegler, *Proc. SPIE* **5783**, 123 (2005).
- <sup>109</sup>E. H. Aifer, J. G. Tischler, J. H. Warner, I. Vurgaftman, W. W. Bewley, J. R. Meyer, C. L. Canedy, and E. M. Jackson, *Appl. Phys. Lett.* **89**, 053519 (2006).
- <sup>110</sup>B.-M. Nguyen, D. Hoffman, P.-Y. Delaunay, and M. Razeghi, *Appl. Phys. Lett.* **91**, 163511 (2007).
- <sup>111</sup>C. L. Canedy, H. Aifer, I. Vurgaftman, J. G. Tischler, J. R. Meyer, J. H. Warner, and E. M. Jackson, *J. Electron. Mater.* **36**, 852 (2007).
- <sup>112</sup>C. H. Grein, H. Cruz, M. E. Flatté, and H. Ehrenreich, *Appl. Phys. Lett.* **65**, 2530 (1994).
- <sup>113</sup>A. Hood, D. Hoffman, Y. Wei, F. Fuchs, and M. Razeghi, *Appl. Phys. Lett.* **88**, 052112 (2006).
- <sup>114</sup>W. Cabanski, K. Eberhardt, W. Rode, J. Wendler, J. Ziegler, J. Fleißner, F. Fuchs, R. Rehm, J. Schmitz, H. Schneider, and M. Walther, *Proc. SPIE* **5406**, 184 (2004).
- <sup>115</sup>Y. Arakawa and H. Sakaki, *Appl. Phys. Lett.* **40**, 939 (1982).
- <sup>116</sup>D. Leonard, M. Krishnamurthy, C. M. Reaves, S. P. Denbaars, and P. M. Petroff, *Appl. Phys. Lett.* **63**, 3203 (1993).
- <sup>117</sup>I. N. Stranski and L. Krastanow, *Sitzungsber. Akad. Wiss. Wien, Math.-Naturwiss. Kl., Abt. 2B* **146**, 797 (1937).
- <sup>118</sup>Ch. Sikorski and U. Merkt, *Phys. Rev. Lett.* **62**, 2164 (1989).
- <sup>119</sup>T. Demel, D. Heitmann, P. Grambow, and K. Ploog, *Phys. Rev. Lett.* **64**, 788 (1990).
- <sup>120</sup>J. Phillips, K. Kamath, and P. Bhattacharya, *Appl. Phys. Lett.* **72**, 2020 (1998).
- <sup>121</sup>P. Bhattacharya and Z. Mi, *Proc. IEEE* **95**, 1723 (2007).
- <sup>122</sup>J. C. Campbell and A. Madhukar, *Proc. IEEE* **95**, 1815 (2007).
- <sup>123</sup>P. Boucaud and S. Sauvage, *C. R. Phys.* **4**, 1133 (2003).
- <sup>124</sup>S. Y. Wang, S. D. Lin, W. Wu, and C. P. Lee, *Appl. Phys. Lett.* **78**, 1023 (2001).
- <sup>125</sup>V. Ryzhii, *J. Appl. Phys.* **89**, 5117 (2001).
- <sup>126</sup>S. W. Lee, K. Hirakawa, and Y. Shimada, *Appl. Phys. Lett.* **75**, 1428 (1999).
- <sup>127</sup>P. Bhattacharya and Z. Mi, *Proc. IEEE* **95**, 1723 (2007).
- <sup>128</sup>J. C. Campbell and A. Madhukar, *Proc. IEEE* **95**, 1815 (2007).
- <sup>129</sup>S. Krishna, *J. Phys. D* **38**, 2142 (2005).
- <sup>130</sup>M. A. Kinch, *J. Electron. Mater.* **29**, 809 (2000).
- <sup>131</sup>J. Phillips, *J. Appl. Phys.* **91**, 4590 (2002).
- <sup>132</sup>I. Vurgaftman, Y. Lam, and J. Singh, *Phys. Rev. B* **50**, 14309 (1994).
- <sup>133</sup>E. Towe and D. Pan, *IEEE J. Sel. Top. Quantum Electron.* **6**, 408 (2000).
- <sup>134</sup>X. Lu, J. Vaillancourt, and M. J. Meisner, *Appl. Phys. Lett.* **91**, 051115 (2007).
- <sup>135</sup>J. Piotrowski and A. Rogalski, *Infrared Phys. Technol.* **46**, 115 (2004).
- <sup>136</sup>Vigo System, [www.vigo.com.pl](http://www.vigo.com.pl).
- <sup>137</sup>X. H. Su, S. Chakrabarti, P. Bhattacharya, A. Ariyawansa, and A. G. U. Perera, *IEEE J. Quantum Electron.* **41**, 974 (2005).
- <sup>138</sup>J. L. Vampola, in *The Infrared and Electro-Optical Systems Handbook*, edited by W. D. Rogatto (SPIE Optical Engineering, Bellingham, WA, 1993), Vol. 3, pp. 285–342.
- <sup>139</sup>J. Jiang, K. Mi, S. Tsao, W. Zhang, H. Lim, T. O'Sullivan, T. Sills, M. Razeghi, G. J. Brown, and M. Z. Tidrow, *Appl. Phys. Lett.* **84**, 2232 (2004).
- <sup>140</sup>S.-F. Tang, C.-D. Chiang, P.-K. Weng, Y.-T. Gau, J.-J. Luo, S.-T. Yang, C.-C. Shih, A.-Y. Lin, and S.-C. Lee, *IEEE Photonics Technol. Lett.* **18**, 986 (2006).
- <sup>141</sup>H. Halpert and B. I. Musicant, *Appl. Opt.* **11**, 2157 (1972).
- <sup>142</sup>InSb/HgCdTe two-color detector, <http://www.irassociates.com/inshhgcdte.htm>.
- <sup>143</sup>J. C. Campbell, A. G. Dentai, T. P. Lee, and C. A. Burrus, *IEEE J. Quantum Electron.* **16**, 601 (1980).
- <sup>144</sup>E. R. Blazejewski, J. M. Arias, G. M. Williams, W. McLevige, M. Zandian, and J. Pasko, *J. Vac. Sci. Technol. B* **10**, 1626 (1992).
- <sup>145</sup>J. A. Wilson, E. A. Patten, G. R. Chapman, K. Kosai, B. Baumgratz, P. Goetz, S. Tighe, R. Risser, R. Herald, W. A. Radford, T. Tung, and W. A. Terre, *Proc. SPIE* **2274**, 117 (1994).
- <sup>146</sup>R. D. Rajavel, D. M. Jamba, J. E. Jensen, O. K. Wu, J. A. Wilson, J. L. Johnson, E. A. Patten, K. Kasai, P. M. Goetz, and S. M. Johnson, *J. Electron. Mater.* **27**, 747 (1998).

- <sup>147</sup>W. A. Radford, E. A. Patten, D. F. King, G. K. Pierce, J. Vodicka, P. Goetz, G. Venzor, E. P. Smith, R. Graham, S. M. Johnson, J. Roth, B. Nosh, and J. Jensen, *Proc. SPIE* **5783**, 331 (2005).
- <sup>148</sup>E. P. G. Smith, L. T. Pham, G. M. Venzor, E. M. Norton, M. D. Newton, P. M. Goetz, V. K. Randall, A. M. Gallagher, G. K. Pierce, E. A. Patten, R. A. Coussa, K. Kosai, W. A. Radford, L. M. Giegerich, J. M. Edwards, S. M. Johnson, S. T. Baur, J. A. Roth, B. Nosh, T. J. De Lyon, J. E. Jensen, and R. E. Longshore, *J. Electron. Mater.* **33**, 509 (2004).
- <sup>149</sup>E. P. G. Smith, E. A. Patten, P. M. Goetz, G. M. Venzor, J. A. Roth, B. Z. Nosh, J. D. Benson, A. J. Stoltz, J. B. Varesi, J. E. Jensen, S. M. Johnson, and W. A. Radford, *J. Electron. Mater.* **35**, 1145 (2006).
- <sup>150</sup>M. B. Reine, A. Hairston, P. O'Dette, S. P. Tobin, F. T. J. Smith, B. L. Musicant, P. Mitra, and F. C. Case, *Proc. SPIE* **3379**, 200 (1998).
- <sup>151</sup>J. P. Zanatta, P. Ferret, R. Loyer, G. Petroz, S. Cremer, J. P. Chamonal, P. Bouchut, A. Million, and G. Destefanis, *Proc. SPIE* **4130**, 441 (2000).
- <sup>152</sup>P. Tribolet, *Proc. SPIE* **5964**, 49 (2005).
- <sup>153</sup>J. P. Zanatta, G. Badano, P. Ballet, C. Langeron, J. Baylet, O. Gravrand, J. Rothman, P. Castelein, J. P. Chamonal, A. Million, G. Destefanis, S. Mibord, E. Brochier, and P. Costa, *J. Electron. Mater.* **35**, 1231 (2006).
- <sup>154</sup>J. Giess, M. A. Glover, N. T. Gordon, A. Graham, M. K. Haigh, J. E. Hails, D. J. Hall, and D. J. Lees, *Proc. SPIE* **5783**, 316 (2005).
- <sup>155</sup>C. L. Jones, L. G. Hipwood, J. Price, C. J. Shaw, P. Abbott, C. D. Maxey, H. W. Lau, R. A. Catchpole, M. Ordish, P. Knowles, and N. T. Gordon, *Proc. SPIE* **6542**, 654210 (2007).
- <sup>156</sup>F. Aqariden, P. D. Dreiske, M. A. Kinch, P. K. Liao, T. Murphy, H. F. Schaake, T. A. Shafer, H. D. Shih, and T. H. Teherant, *J. Electron. Mater.* **36**, 900 (2007).
- <sup>157</sup>W. E. Tennant, M. Thomas, L. J. Kozlowski, W. V. McLevige, D. D. Edwall, M. Zandian, K. Spariosu, G. Hildebrandt, V. Gil, P. Ely, M. Muzilla, A. Stoltz, and J. H. Dinan, *J. Electron. Mater.* **30**, 590 (2001).
- <sup>158</sup>L. A. Almeida, M. Thomas, W. Larsen, K. Spariosu, D. D. Edwall, J. D. Benson, W. Mason, A. J. Stoltz, and J. H. Dinan, *J. Electron. Mater.* **31**, 669 (2002).
- <sup>159</sup>A. H. Lockwood, J. R. Balon, P. S. Chia, and F. J. Renda, *Infrared Phys.* **16**, 509 (1976).
- <sup>160</sup>J. Baylet, P. Ballet, P. Castelein, F. Rothan, O. Gravrand, M. Fendler, E. Laffosse, J. P. Zanatta, J. P. Chamonal, A. Million, and G. D. Destefanis, *J. Electron. Mater.* **35**, 1153 (2006).
- <sup>161</sup>E. P. G. Smith, E. A. Patten, P. M. Goetz, G. M. Venzor, J. A. Roth, B. Z. Nosh, J. D. Benson, A. J. Stoltz, J. B. Varesi, J. E. Jensen, S. M. Johnson, and W. A. Radford, *J. Electron. Mater.* **35**, 1145 (2006).
- <sup>162</sup>E. P. G. Smith, R. E. Bornfreund, I. Kasai, L. T. Pham, E. A. Patten, J. M. Peterson, J. A. Roth, B. Z. Nosh, T. J. Lyon, J. E. Jensen, J. W. Bangs, S. M. Johnson, and W. A. Radford, *Proc. SPIE* **6127**, 61271F (2006).
- <sup>163</sup>P. R. Norton, *Proc. SPIE* **3379**, 102 (1998).
- <sup>164</sup>K. Józwikowski and A. Rogalski, *J. Appl. Phys.* **90**, 1286 (2001).
- <sup>165</sup>A. K. Sood, J. E. Egerton, Y. R. Puri, E. Bellotti, D. D'Orsogna, L. Becker, R. Balcerak, K. Freyvogel, and R. Richwine, *J. Electron. Mater.* **34**, 909 (2005).
- <sup>166</sup>E. Bellotti and D. D'Orsogna, *IEEE J. Quantum Electron.* **42**, 418 (2006).
- <sup>167</sup>L. G. Hipwood, C. L. Jones, C. D. Maxey, H. W. Lau, J. Fitzmaurice, R. A. Catchpole, and M. Ordish, *Proc. SPIE* **6206**, 620612 (2006).
- <sup>168</sup>K. Józwikowski and A. Rogalski, *Opto-Electron. Rev.* **15**, 215 (2007).
- <sup>169</sup>W. A. Beck and T. S. Faska, *Proc. SPIE* **2744**, 193 (1996).
- <sup>170</sup>M. Sundaram and S. C. Wang, *Proc. SPIE* **4028**, 311 (2000).
- <sup>171</sup>S. D. Gunapala, S. V. Bandara, J. K. Liu, E. M. Luong, S. B. Rafol, J. M. Mumolo, D. Z. Ting, J. J. Bock, M. E. Ressler, M. W. Werner, P. D. LeVan, R. Chehayeb, C. A. Kukkonen, M. Ley, P. LeVan, and M. A. Fauci, *Opto-Electron. Rev.* **8**, 150 (2001).
- <sup>172</sup>S. D. Gunapala, S. V. Bandara, A. Singh, J. K. Liu, S. B. Rafol, E. M. Luong, J. M. Mumolo, N. Q. Tran, J. D. Vincent, C. A. Shott, J. Long, and P. D. LeVan, *Proc. SPIE* **3698**, 687 (1999).
- <sup>173</sup>S. D. Gunapala, S. V. Bandara, A. Singh, J. K. Liu, B. Rafol, E. M. Luong, J. M. Mumolo, N. Q. Tran, D. Z. Ting, J. D. Vincent, C. A. Shott, J. Long, and P. D. LeVan, *IEEE Trans. Electron Devices* **47**, 963 (2000).
- <sup>174</sup>S. D. Gunapala, S. V. Bandara, J. K. Liu, B. Rafol, J. M. Mumolo, C. A. Shott, R. Jones, J. Woolaway, J. M. Fastenau, A. K. Liu, M. Jhabvala, and K. K. Choi, *Infrared Phys. Technol.* **44**, 411 (2003).
- <sup>175</sup>A. Goldberg, T. Fischer, J. Kennerly, S. Wang, M. Sundaram, P. Uppal, M. Winn, G. Milne, and M. Stevens, *Proc. SPIE* **4028**, 276 (2000).
- <sup>176</sup>M. Jhabvala, *Infrared Phys. Technol.* **42**, 363 (2001).
- <sup>177</sup>E. Costard, Ph. Bois, X. Marcadet, and A. Nedelcu, *Proc. SPIE* **5783**, 728 (2005).
- <sup>178</sup>W. Cabanski, M. Münzberg, W. Rode, J. Wendler, J. Ziegler, J. Fleißner, F. Fuchs, P. Rehm, J. Schmitz, H. Schneider, and M. Walther, *Proc. SPIE* **5783**, 340 (2005).
- <sup>179</sup>H. Schneider, T. Maier, J. Fleissner, M. Walther, P. Koidl, G. Weimann, W. Cabanski, M. Finck, P. Menger, W. Rode, and J. Ziegler, *Infrared Phys. Technol.* **47**, 53 (2005).
- <sup>180</sup>S. Gunapala <http://compoundsemiconductor.net/cws/article/magazine/23363>.
- <sup>181</sup><http://www.qumagiq.com>.
- <sup>182</sup>S. D. Gunapala, S. V. Bandara, J. K. Liu, B. Rafol, and J. M. Mumolo, *IEEE Trans. Electron Devices* **50**, 2353 (2003).
- <sup>183</sup>E. H. Aifer, J. G. Tischler, J. H. Warner, I. Vurgaftman, and J. R. Meyer, *Proc. SPIE* **5783**, 112 (2005).
- <sup>184</sup>M. Münzberg, R. Breiter, W. Cabanski, K. Hofmann, H. Lutz, J. Wendler, J. Ziegler, P. Rehm, and M. Walther, *Proc. SPIE* **6542**, 654207 (2007).
- <sup>185</sup>X. Lu, J. Vaillancourt, and M. Meisner, *Proc. SPIE* **6542**, 65420Q (2007).
- <sup>186</sup>U. Sakoglu, J. S. Tyo, M. M. Hayat, S. Raghavan, and S. Krishna, *J. Opt. Soc. Am. B* **21**, 7 (2004).
- <sup>187</sup>A. G. U. Perera, *Opto-Electron. Rev.* **14**, 99 (2006).
- <sup>188</sup>W. I. Gunning, J. DeNatale, P. Stupar, R. Borwick, S. Lauxterman, P. Kobrin, and J. Auyeung, *Proc. SPIE* **6232**, 62320F (2006).
- <sup>189</sup>C. A. Musca, J. Antoszewski, K. J. Winchester, A. J. Keating, T. Nguyen, K. K. M. B. D. Silva, J. M. Dell, L. F. Faraone, P. Mitra, J. D. Beck, M. R. Skokan, and J. E. Robinson, *IEEE Electron Device Lett.* **26**, 888 (2005).
- <sup>190</sup>A. J. Keating, K. K. M. B. D. Silva, J. M. Dell, C. A. Musca, and L. Faraone, *IEEE Photonics Technol. Lett.* **18**, 1079 (2006).
- <sup>191</sup>J. Carrano, J. Brown, P. Perconti, and K. Barnard, SPIE's OEmagazine **20** (2004).